

AFWAL-TR-80-4045

Volume III

Pt I

ADA 120709

MECHANICAL PROPERTIES VS MORPHOLOGY OF ORDERED POLYMERS  
VOLUME III



E. L. Thomas, R. J. Farris and S. L. Hsu

Polymer Science & Engineering Department  
The University of Massachusetts  
Amherst, MA 01003

August 1982

INTERIM REPORT FOR PERIOD 1 SEPTEMBER 1980 THROUGH 30 AUGUST 1981

Approved for public release; distribution unlimited

MATERIALS LABORATORY  
AIR FORCE WRIGHT AERONAUTICAL LABORATORIES  
AIR FORCE SYSTEMS COMMAND  
WRIGHT-PATTERSON AIR FORCE BASE, OHIO 45433

20040223024

BEST AVAILABLE COPY

NOTICE

When Government drawings, specifications, or other data are used for any purpose other than in connection with a definitely related Government procurement operation, the United States Government thereby incurs no responsibility nor any obligation whatsoever; and the fact that the government may have formulated, furnished, or in any way supplied the said drawings, specifications, or other data, is not to be regarded by implication or otherwise as in any manner licensing the holder or any other person or corporation, or conveying any rights or permission to manufacture use, or sell any patented invention that may in any way be related thereto.

This report has been reviewed by the Office of Public Affairs (ASD/PA) and is releasable to the National Technical Information Service (NTIS). At NTIS, it will be available to the general public, including foreign nations.

This technical report has been reviewed and is approved for publication.



T. E. HELMINIAK  
Project Monitor



R. L. VAN DEUSEN, Chief  
Polymer Branch  
Nonmetallic Materials Division

FOR THE COMMANDER



FRANKLIN D. CHERRY, Chief  
Nonmetallic Materials Division

"If your address has changed, if you wish to be removed from our mailing list, or if the addressee is no longer employed by your organization please notify AFWAL/MLBP, W-PAFB, OH 45433 to help us maintain a current mailing list".

Copies of this report should not be returned unless return is required by security considerations, contractual obligations, or notice on a specific document.

## UNCLASSIFIED

SECURITY CLASSIFICATION OF THIS PAGE (When Data Entered)

REPORT DOCUMENTATION PAGE		READ INSTRUCTIONS BEFORE COMPLETING FORM	
1. REPORT NUMBER  AFWAL-TR-80-4045, Volume III Pt I	2. GOVT ACCESSION NO.	3. RECIPIENT'S CATALOG NUMBER	
4. TITLE (and Subtitle)  MECHANICAL PROPERTIES VS MORPHOLOGY OF ORDERED POLYMERS VOLUME III PART I	5. TYPE OF REPORT & PERIOD COVERED Interim, End of third year effort, 1 Sept 80 - 30 Aug 81		
7. AUTHOR(s)  E. L. Thomas, R. J. Farris, S. L. Hsu	6. PERFORMING ORG. REPORT NUMBER  F33615-78-C-5175		
9. PERFORMING ORGANIZATION NAME AND ADDRESS  Polymer Science and Engineering Department University of Massachusetts Amherst, MA 01003	10. PROGRAM ELEMENT, PROJECT, TASK AREA & WORK UNIT NUMBERS  24190407		
11. CONTROLLING OFFICE NAME AND ADDRESS  Materials Laboratory (AFWAL/MLBP) Air Force Wright Aeronautical Laboratories (AFSC) Wright-Patterson Air Force Base, OH 45433	12. REPORT DATE August 1982		
14. MONITORING AGENCY NAME & ADDRESS(if different from Controlling Office)	13. NUMBER OF PAGES 161		
	15. SECURITY CLASS. (of this report)  UNCLASSIFIED		
	15a. DECLASSIFICATION/DOWNGRADING SCHEDULE		
16. DISTRIBUTION STATEMENT (of this Report)  Approved for public release; distribution unlimited			
17. DISTRIBUTION STATEMENT (of the abstract entered in Block 20, if different from Report)			
18. SUPPLEMENTARY NOTES  AFWAL-TR-80-4045, Volume III, Part II contains computer software; therefore distribution is limited in accordance with AFR 300-6. Non-DOD requests must include the statement of terms and conditions contained in Atch 21 to AFR 300-6.			
19. KEY WORDS (Continue on reverse side if necessary and identify by block number)  Heterocyclic Polymers Rodlike Polymers High Modulus High Strength			
20. ABSTRACT (Continue on reverse side if necessary and identify by block number)  Morphological techniques in conjunction with mechanical testing have been used to elucidate the relationships between mechanical properties and sample microstructures and to use this knowledge to obtain the maximum in strength and modulus for rigid rod polymer fiber and film. The fibers and films of poly (p-phenylene benzobisthiazole) (PBT) which have been investigated were produced at Celanese Research Corporation from liquid crystalline solutions using a dry-jet wet spin process for fibers and either shear or extrusion for films.			

Microstructural studies involve predominantly scanning and transmission electron microscopy, small and wide angle x-ray scattering and electron diffraction. Mechanical behavior has been assessed in tensile, fatigue, bending and torsion tests. Tensile properties have been measured over the range -100°C to +200°C. Studies of low molecular weight model compounds and poly-p-phenylene benzo-bisoxazole (PBO) and PBT polymers in solution and solid states have also been done by laser Raman and Fourier transform infrared spectroscopy.

Heat treated fibers have been produced with a modulus of 2100 grams per denier (g/d) and a tenacity of 20 g/d. These properties place PBT in a prominent position with respect to other high performance materials. In addition to their high specific modulus and strength, the fibers' thermal and environmental stability is outstanding. Correlation of sample microstructure and resultant mechanical properties with processing conditions has been done to help optimize processing conditions.

## FOREWORD

This report covers the work performed by the University of Massachusetts, Amherst, Massachusetts 01003, on "Mechanical Properties versus Morphology of Ordered Polymers." The work was conducted under contract F33615-78-C-5175 for the Materials Laboratory. The performance period was from 1 September 1980 to 1 September 1981. This report was submitted in January 1982.

The work was performed in the Polymer Science and Engineering Department with Professor Edwin L. Thomas acting as principal investigator, and Professors R. J. Farris and S. L. Hsu as coprincipal investigators. The assistance of Messrs. S. Allen, A. Filippov and J. Minter and Drs. D. Shen, K. Shimamura, and G. Venkatesh is gratefully acknowledged. The project engineer was Dr. Thaddeus E. Helminiak, AFWAL/MLBP, Materials Laboratory, Wright-Patterson Air Force Base, Ohio.

## TABLE OF CONTENTS

	PAGE
SECTION I: OVERVIEW . . . . .	1
SECTION II: SPECTROSCOPY . . . . .	4
A. Introduction . . . . .	4
B. Microstructural Changes in Stressed PBT . . . . .	5
1. Experimental . . . . .	6
2. Stress Induced Structural Changes . . . . .	8
C. Protonation Effect . . . . .	13
1. Experimental . . . . .	14
2. Structural Analysis of Protonated Molecules. . .	15
3. Dilution Experiments: On the Reversibility of Protonation of PBT . . . . .	18
4. Determination of the Spectroscopic Features of Half Protonated and Fully Protonated Species . .	19
SECTION III: MORPHOLOGICAL INVESTIGATIONS . . . . .	39
A. High Resolution Dark Field of PBT Films . . . . .	39
B. Lattice Imaging from PBT Fibers . . . . .	41
C. Calculation of the Fourier Transform of a Single PBT Chain . . . . .	44
1. Cylindrically Averaged Fourier Transforms . . . . .	46

TABLE OF CONTENTS (cont'd.)

	PAGE
2. Chains with Preferential Orientation . . . . .	47
D. Packing Analysis in the PBT Unit Cell . . . . .	48
1. Packing Analysis of PBT Chains . . . . .	48
E. Light Microscopy of PBT Ribbons from PPA Dopes:	
Influence of Processing Conditions . . . . .	50
F. Small Angle Neutron Scattering . . . . .	51
1. SANS of Dilute Mixtures . . . . .	54
2. Preliminary Results . . . . .	58
G. Microvoid Analysis by Small Angle X-ray Scattering. .	59
1. The Intensity of Small Angle Scattering . . . . .	61
2. Isotropic Systems . . . . .	64
a. Guinier's Law . . . . .	64
b. Debye-Bueche Theory . . . . .	64
3. Extension to Anisotropic Systems. . . . .	66
a. The Projected Correlation Function. . . . .	66
b. Extension to Uniaxial Systems Using Spherical	
Coordinates . . . . .	68
c. Guinier Analysis of Anisotropic Systems . . .	69
d. Extension to Uniaxial Systems Using Cylindrical	
Coordinates. . . . .	71
e. Analysis of Diffuse SAXS from Selected Fibers	
and Films. . . . .	73

TABLE OF CONTENTS (concluded)

	PAGE
f. Comparison of the Models for Data Analysis . . . . .	76
g. Correlation of Void Size with Processing	
Conditions. . . . .	77
4. Suggestions for Future Experiments. . . . .	78
SECTION IV: MECHANICAL PROPERTIES . . . . .	114
A. Fiber heat treatment . . . . .	114
B. Temperature Dependence of Tensile Properties. . . . .	119
C. Fiber Torsional Modulus . . . . .	121
D. Large Torsional Deformation: Twisting . . . . .	123
E. Torsion-Tension Testing . . . . .	124
F. Mandrel Loop Tests. . . . .	126
G. Elastica Loop Tests . . . . .	127
H. Compressive Behavior. . . . .	133
REFERENCES . . . . .	155

## LIST OF ILLUSTRATIONS

FIGURE	PAGE
1      Schematic drawing of the coupling between mechanical deformation and FTIR . . . . .	29
2      Polarized infrared spectra obtained from highly oriented PBT film: A. Parallel polarization; B. Perpendicular polarization . . . . .	30
3      Infrared spectra obtained from highly oriented PBT films: A. Curve corresponds to spectrum taken with film plane perpendicular to the incident radiation; B. Curve corresponds to a 45° rotation . . . . .	31
4      Infrared spectra of PBT: A. Taken from an unoriented sample; B. Spectrum taken from a highly oriented film . . . . .	32
5      Stress induced relative intensity changes: A. No stress; B. 0.18 GPa stress applied . . . . .	33
6      Stress induced spectroscopic changes for the 1252 cm <sup>-1</sup> band in PBT: A. No stress; B. 0.18 GPa; C. Spectrum taken immediately after stress is released (< 70 sec); D. Spectrum taken from a relaxed sample . . . . .	34
7      Frequency shift of the 1252 cm <sup>-1</sup> band as a function of stress . . . . .	35

LIST OF ILLUSTRATIONS (Cont'd.)

FIGURE		PAGE
8	Spectra infrared spectra taken after the stress is applied: A. Immediately after the stress is applied (<0.35 sec, 0.18 GPa); B. Taken after 140 sec. when stress is relaxed to 0.11 GPa . . . . .	36
9	Raman Spectrum of PBT in MSA. Laser Power: 15 nm at 5145 Å; Bandpass: 2 cm <sup>-1</sup> at 5100 Å . . . . .	37
10	Raman Spectrum of PBT solid. Laser Power: 15 mw at 5145 Å; Bandpass: 2 cm <sup>-1</sup> at 5100 Å . . . . .	38
11	Decay of e <sub>2</sub> -e <sub>4</sub> for PBT at a dose rate, j <sub>0</sub> = 2.8 x 10 <sup>-3</sup> coul/cm <sup>-2</sup> sec <sup>-1</sup> . Inset: schematic of electron diffraction pattern showing approximate radius of objective aperture . . . . .	81
12	DF micrograph of PBT fragment suspended over a gold decorated, perforated support film (S). "K" denotes kinked area. Extrusion direction is vertical. Instrumental Magnification = 33,000X. Top: Enlargement of boxed area at bottom. "B"s denote probable buckled regions . . . . .	82
13	DF micrographs (10,000 instrumental magnification) of the same area of a PBT film using e <sub>2</sub> -e <sub>4</sub> and e <sub>1</sub> reflections, respectively . . . . .	83
14	(a) Electron diffraction pattern of a typical 'as-spun' PBT fiber . . . . .	84

LIST OF ILLUSTRATIONS (cont'd.)

FIGURE		PAGE
	(b) Electron diffraction pattern of typical 'heat treated' PBT fiber. Arrows indicate splitting of sixth layer line . . . . .	84
15	Two regions of an axial bright field lattice image (100,000X instrumental magnification) of a tension heat treated fiber . . . . .	85
16	(a) Optical transform of micrograph used to obtain Figure 3.5 . . . . .	86
	(b) Schematic of Figure 3.6a. Sharp spots are due to .59 nm E fringes and diffuse streaks to 1.24 nm M fringes . . . . .	87
17	Definition of the scattering vectors used . . . . .	
18	Cylindrically averaged molecular transform for a single PBT chain of 8 units using coordinates of Odell <u>et. al</u> [7]. Temperature factor (.025 nm <sup>2</sup> perpendicular to chain and is .005 nm <sup>2</sup> parallel to chain axis) . . . . .	88
19	Matrix printer output of cylindrical averaged molecular transform for a single PBT chain of 8 units by Odell <u>et. al</u> [7] . . . . .	89

LIST OF ILLUSTRATIONS (cont'd.)

FIGURE		PAGE
20	Cylindrical averaged molecular transform for a single PBT chain of 8 units using coordinates of Wellman <u>et al.</u> [44]. Temperature factor .025 nm <sup>2</sup> perpendicular to chain axis, .005 nm <sup>2</sup> parallel to chain axis . . . . .	90
21	Cylindrical averaged molecular transform for a single PBT chain of 8 units using coordinates of Wellman <u>et al.</u> [7]. Temperature factor .06 nm <sup>2</sup> parallel to chain axis and .06 nm <sup>2</sup> perpendicular to chain axis . . . . .	91
22	Distribution of intensity about $\lambda = 6$ for case in Figure 20 in steps of $S_1 = \pm 0.02 \text{ nm}^{-1}$ . . . . .	92
23	Molecular transform for a single PBT molecule of 8 units. Conformational angle between phenyl and bisthiazole moieties ( $\phi$ ) = 35° as a function of angle of incidence of beam ( $\alpha$ ). (a) $\alpha = 0$ . . . . .	93
	(b) $\alpha = 35$ . . . . .	94
	(c) $\alpha = 45$ . . . . .	95
	(d) $\alpha = 60$ . . . . .	96
	(e) $\alpha = 90$ . . . . .	97
24	Molecular transform for a single PBT molecule of 8 units. Conformational angle between phenyl and bisthiazole moieties ( $\phi$ ), angle of incidence of beam ( $\alpha$ ). (a) $\phi = 0$ , $\alpha = 0$ . . . . .	98

LIST OF ILLUSTRATIONS (cont'd.)

FIGURE		PAGE
	(b) $\phi = 25^\circ$ , $\alpha = 0$ . . . . .	99
	(c) $\phi = 45^\circ$ , $\alpha = 0$ . . . . .	100
25	Comparison of cylindrically averaged molecular transforms of PBT chains to measured electron diffraction profile for the sixth layer line.	
	Calc 1 - using coordinates of Odell <u>et al.</u> [41] . . . . .	101
	Calc 2 - using coordinates of Wellmann <u>et al.</u> [44] . . . . .	101
	Exptl - microdensitometer profile . . . . .	101
26	Definition of parameters for conformational calculations.	102
27	Proposed structure of PBT. Top: monoclinic net. Bottom: chains in net (with translational freedom) . . . . .	103
28	Conformational energy for PBT cell as a function of chain rotational angle . . . . .	104
29	Polarized light micrograph of PBT-29022-7-8. (a) Film oriented at $45^\circ$ to polarizer . . . . .	105
	(b) Film oriented at $5^\circ$ to polarizer . . . . .	105
30	Polarized light micrograph of PBT-29022-5a. (a) Film oriented at $45^\circ$ to polarizer . . . . .	106
	(b) Film oriented at $0^\circ$ to polarizer . . . . .	106
31	Scattering functions for a rod and a sphere. . . . .	107
32	SAXS from annealed PBT fibers . . . . .	108
33	Model for interpreting SAXS from PBT . . . . .	109

LIST OF ILLUSTRATIONS (cont'd.)

FIGURE		PAGE
34	Guinier plot of PBT equatorial small angle x-ray scattering . . . . .	110
35	Debye plot of PBT equatorial small angle x-ray scattering . . . . .	111
36	Cylindrical correlation function for PBT SAXS . . . . .	112
37	Projected correlation function along R <sub>2</sub> . . . . .	113
38	Schematic of fiber heat treatment apparatus . . . . .	136
39	Typical temperature profile in the heat treatment chamber. . . . .	137
40	Summary of heat treated fiber modulus dependence on heat treatment temperature and tension. Residence time 77 seconds, no aftercooler. . . . .	138
41	Summary of heat treated fiber strength dependence on heat treatment temperature and tension. Residence time 77 seconds, no aftercooler. . . . .	139
42	Modulus, of 595°C heat treated fiber, dependence on residence time and tension. Nitrogen aftercooler used. . . .	140
43	Strength, of 595°C heat treated fiber, dependence on residence time and tension. Nitrogen aftercooler used. . . .	141
44	Temperature dependence of Kevlar (K-49,K-29), as spun PBT (9-10,33-5) and heat treated PBT (42-2) fiber modulus. . .	142
45	Temperature dependence of Kevlar (K-49,K-29), as spun PBT (9-10,33-5) and heat treated PBT (42-2) fiber strength . .	143

#### LIST OF ILLUSTRATIONS (concluded)

FIGURE		PAGE
46	Fiber modulus dependence on temperature for Kevlar 49 and heat treated PBT fibers. . . . .	144
47	Fiber strength dependence on temperature for Keval 49 and heat treated PBT fibers. . . . .	145
48	PBT fiber strength dependence on temperature . . . . .	146
49	Schematic of torsion pendulum apparatus employed for the determination of fiber torsional moduli. . . . .	147
50	Torsional behavior of PBT fibers . . . . .	148
51	Surface appearance of twisted PBT fibers (strains refer to the fiber surface) . . . . .	149
52	Variation of PBT fiber strength with initial pretwisting .	150
53	a) Geometry of mandrel loop test. b) Loop efficiency of PBT fiber. . . . .	151
54	Geometry of elastica loop test . . . . .	152
55	Elastica loop behavior of PBT fibers . . . . .	153
56	Kinks produced in bending of PBT fibers. . . . .	154

LIST OF TABLES

TABLE		PAGE
1	Infrared Bands Observed for Highly Oriented PBT Film . . . . .	25
2	The Frequency Shift of PBT Infrared Bands Under Mechanical Load (0.18 GPa) . . . . .	26
3	Intensity Variations of Some Raman Bands with Acid Concentration . . . . .	27
4	Relative Intensities of Raman Bands . . . . .	28
5	Scattering Parameters of Atoms Useful for PBT SANS. . . . .	52
6	Parameters for Contrast Factor and Signal to Noise Calculations for SANS . . . . .	53
7	Optimum Matrix Thickness for SANS of PBT . . . . .	55
8	Contrast Factor and Signal to Noise Ratio for Selected Pairs of Species 1 (LABEL) in Species 2 (MATRIX) for Small Angle Neutron Scattering Assuming $W_1 = 0.01$ and $DP_1 = 50$ . . . . .	58
9	Comparison of Tensile and Torsional Moduli . . . . .	135

## SECTION I: OVERVIEW

The goal of this project is to determine for rigid rod polymer fibers and films, the relationships between mechanical properties and sample microstructures and to use this knowledge to obtain the maximum in strength and modulus for these materials. The fibers and films of poly(p-phenylene benzobisthiazole) (PBT) which have been investigated were produced at Celanese Research Corporation (Dr. E.C. Chenevey) from liquid crystalline solutions using a dry-jet-wet spin process for fibers and either shear or extrusion for films.

Microstructural studies involve predominantly scanning and transmission electron microscopy, small and wide angle x-ray scattering and electron diffraction. Mechanical behavior has been assessed in tensile, fatigue, bending and torsion tests. Tensile properties have been measured over the range -100°C to +200°C. Studies of low molecular weight model compounds and poly-p-phenylene benzo-bisoxazole (PBO) and PBT polymers in solution and solid states have also been done by laser Raman and Fourier transform infrared spectroscopy.

Heat treated fibers have been produced with a modulus of 2100 grams per denier (g/d) and a tenacity of 20 g/d. These properties place PBT in a prominent position with respect to other high performance materials. In addition to their high specific modulus and strength, the fibers' thermal and environmental stability is outstanding. Correlation of sample microstructure and resultant mechanical properties with processing conditions has been done to help optimize processing conditions.

During the past year the following publications have appeared:

1. S.R. Allen, A.G. Filippov, R.J. Farris and E.L. Thomas, C.P. Wong, G.C. Berry and E.C. Chenevey, *Macromolecules*, 14, 1135-1138 (1981), "Mechanical Studies of High-Strength, High-Modulus Poly(p-phenylene-benzobisthiazole) Fibers".
2. J.R. Minter, *Proceedings of the Electron Microscopical Society of America*, 37, 342-343 (1981), "High Resolution Dark Field of Poly (p-phenylene Benzobisthiazole)".
3. J.R. Minter, K. Shimamura, and E.L. Thomas, *J. Material Science* (1981), "Microstructural Study of As-Extruded and Heat Treated Ribbons of Poly(p-phenylene Benzobisthiazole)".
4. G.M. Venkatesh, D.Y. Shen and S.L. Hsu, *Journal of Polymer Science: Polymer Physics Edition*, Vol. 19, 1475 (1981), "Spectroscopic Study of Rigid-Rod Polymers: I. Structures of Model Compounds".

and the following papers have been submitted for publication:

1. S.R. Allen, A.G. Filippov, R.J. Farris and E.L. Thomas, The Strength and Stiffness of Polymers, edited by A.E. Zachariades and R.S. Porter, Marcel Dekker, Inc., New York (1982), "Structure-Property Relations in Poly(p-Phenylene Benzobisthiazole) Fibers".
2. D.Y. Shen, G.M. Venkatesh, D.J. Burchell and S.L. Hsu, *Journal of Polymer Science (Physics)*, to be published (1982), "Spectroscopic Study of Rigid Rod Polymers: II. Protonation Effect".
3. D.Y. Shen and S.L. Hsu, *Polymer*, in press., "Vibrational Spectroscopic Characterization of Rigid Rod Polymers: III. Microstructural Changes in Stressed Polymers".

The general approach of the University of Massachusetts contract for microstructure-mechanical property relations continues along three lines. The following three areas summarize the three main sections of this report:

1. Spectroscopic Studies (see Section II: Dr. S.L. Hsu)
2. Morphological Studies (see Section III: Dr. E.L. Thomas)
3. Mechanical Studies (see Section IV: Dr. R.J. Farris)

## SECTION II: SPECTROSCOPY

### A. Introduction

In the last year, we gave particular attention to the characterization of structure-property relationships for PBT fibers and films by using a combination of mechanical and vibrational spectroscopic techniques. These types of experiments provide more than just numerical values of physical properties. They can potentially yield insight on microstructural parameters affecting the mechanical response such as orientational order, molecular slippage and mobility, and stress or strain activated microstructural damage. In these experiments, highly oriented PBT fibers were stressed in a small hydraulic tester interfaced to a fast scanning Fourier transform infrared spectrometer.

The infrared spectra obtained for stressed PBT exhibit a number of changes in band polarization, frequency and shape. The stress induced polarization changes have been explained in terms of the coplanarity between the phenyl ring and the heterocyclic ring. In most cases frequency changes can be explained by a reduction of the force constant for polymers in the stressed state. However, the frequency shift of perpendicularly polarized bands have been interpreted to result from a disruption of intermolecular interaction in stressed polymers. This interpretation is supported by the changing frequency of similar magnitude also observed in samples containing much lower degrees of orientational order. Lastly, by using a rapid scanning Fourier transform technique, we observed that frequency and bandshape change at very different time scale. The eventual goal is to correlate these changes to the molecular dynamics when a macroscopic

stress is applied to the polymers.

In the past year, we also analyzed the structural aspects of PBT in methane sulfonic acid solution. The protonation processes of PBT and model compounds have been studied by UV-visible and Raman spectroscopy. The protonated structure in strong acid has been determined to be a more conjugated form than the unprotonated structure. This interpretation is supported by the increase in  $\lambda_{\text{max}}$  in the UV-visible absorption spectra. Based on previous studies, the intensity increase associated with the  $1608 \text{ cm}^{-1}$  terminal ring stretching and the increase in C-C stretching frequency can also be associated with such a change in structure. One category of Raman bands can only be seen for solutions containing 0.1 to 5% acid. These bands can be associated with the half protonated structure. The pK values of the two nitrogen atoms measured in our experiments are consistent with other studies. The relative concentrations of each of these three structures: unprotonated, half protonated and fully protonated forms, are very sensitive to the temperature of measurement.

#### B. Microstructural Changes in Stressed PBT

Mechanical behavior of these rigid rod polymers has been studied extensively by Professor Farris' group. Several recent studies have shown the utility of vibrational spectroscopy in order to gain greater insight into the microstructural response when an external stress is applied. Spectroscopic features such as band polarization, frequency, intensity and shape can all be sensitive to an external stress [1-7]. Their changes have been associated with changes in chain conformation, orientation and packing. This type of

information supplements the macroscopic performance data, leading ultimately to a more accurate description of the structure-property relationships.

However, because of stress relaxation this type of time dependent spectroscopic analysis is difficult. The multiplex characteristic (the ability to measure all spectral elements) of a Fourier transform infrared spectrometer (FTIR) together with the high energy throughput provide FTIR with a substantial gain in signal to noise ratio for a given measurement time when compared to a dispersive instrument. Therefore, it is feasible to use FTIR to follow time dependent phenomena. Unlike a dispersive instrument, simultaneous measurements of band position, shape and relative intensity over a wide frequency region are retained in FTIR studies. We have followed the stress induced structural changes of PBT with our rapid scanning FTIR.

### 1. Experimental

PBT and its model compounds were furnished by the Materials Laboratory, Wright-Patterson Air Force Base, Ohio. Highly oriented fibers or films processed at Celanese Corporation have been characterized and used for these spectroscopic studies [8]. We have also prepared highly oriented films ( $\sim 10 \mu\text{m}$  thick) in our laboratory from a 6% solution of PBT (intrinsic viscosity  $\sim 17$ ) in MSA. The solution was sheared between glass plates, and then coagulated in deionized distilled water. In order to prevent dimensional changes, the films on the glass slide are attached to a frame during the subsequent washing. After continuous washing for two days, the films were dried in air and then in a vacuum oven at room temperature. In all samples, the characteristic band of acid (located at  $1190 \text{ cm}^{-1}$ ) was absent, indicating a complete elimination of

residual acid.

A miniature tensile tester is interfaced to our Nicolet Fourier transform infrared spectrometer. Both the load and displacement values applied to the sample are available in digitized form and accessible by our FTIR minicomputer. Macroscopic mechanical information in the form of stress-strain data is collected along with microscopic information in the form of infrared data.

In previous deformation experiments, the stretching apparatus which generally employed a combination of gear-spindle drives [7-12]. In general, however, this type of device cannot be operated at high deformation frequency or amplitude with sufficient reproducible accuracy necessary in cyclic experiments. Therefore, we have developed a hydraulic stretching device which can be used for stress relaxation, creep, or harmonic deformation experiments in conjunction with a rapid scanning FTIR.

This hydraulic system is schematically outlined in Figure 1. This tester incorporates a closed-loop servo-controller, which drives a hydraulic servo-valve attached to a hydraulic piston. Input to the controller is driven by a function generator, enabling a predefined strain function to be applied to a sample (0.5 cm x 3.0 cm) film in the infrared beam. For accurate control, actual instantaneous sample displacement and applied load are available from a solid state displacement transducer and a load cell. Through this feedback loop to the controller, both the stroke and load are programmable. In addition, both the load and displacement values applied to the sample are available in digitized form and accessible by a minicomputer associated with the FTIR. Thus

accurate macroscopic mechanical information in the form of stress-strain data is collected along with microscopic information in the form of infrared spectra. These highly oriented films were drawn slowly (0.6 mm/min) until nearly broken. The maximum stress and strain obtainable are approximately 0.22 GPa and 3%, respectively. In some cases, the permanent plastic strain reaches 0.8%.

Polarized radiation was obtained with a quad-diamond cell [9]. The infrared spectra were collected using a modified rapid scanning Nicolet 7199 FTIR. Infrared spectra with time resolution in the order of 700 msec can be stored on a magnetic disk for further analysis.

## 2. Stress Induced Structural Changes

The polarization spectra of PBT films as previously described exhibit high orientation (see Figure 2). Several recent studies have shown that three dimensional orientation of polymers can be measured by infrared spectorscopy [10,11]. These measurements generally involve changing the angle of the film plane relative to the polarized incident radiation in order to determine the relative absorptions of transition moments along x and y perpendicular to the chain or Z direction. A series of infrared spectra were measured at angles between 0 to 60°. Representative spectra are shown in Figure 3. Prominent infrared bands and their polarization are listed in Table 1. Since these molecules are complex, accurate vibrational assignments have generally been difficult to achieve [12,13]. Tentative assignments based on model compounds and the measured transition moments are listed in Table 1 [12,13,14-18].

From these band assignments and the orientation measurements, one sees

assignable to phenyl ring exhibit considerable variation. We observed the 1113, 1410 (Figure 2.5) and 3075  $\text{cm}^{-1}$  bands decreased in intensity while the 837  $\text{cm}^{-1}$  band increased in intensity. In contrast, the intensities of the bands assignable to the heterocyclic ring remained unchanged. These results suggest that the dihedral angle of the phenyl ring with respect to the heterocyclic group can also be influenced by the external stress. In our previous Raman studies, dramatic intensity changes associated with backbone vibrations observed in various PBT and PBO model compounds have been interpreted by variations in this dihedral angle, thus affecting the resonance conformation between the two rings. X-ray results for the t-PBT model compound have shown the rings are at an angle of 23°, owing to the steric hinderance between the S and H of the heterocyclic and phenyl ring, respectively [19]. The angle predicted from conformational energy calculations is 60° [20], larger than actually measured. It appears that intermolecular interactions tend to keep the angle low in the solid state [28,29]. When the material is stressed, or in material lacking orientational order, it is reasonable to assign the changing polarization to a disruption of the intermolecular forces or to a direct weakening of the bond connecting two rings, thus affecting the coplanarity of the two rings.

Table 2 lists the frequency shifts caused by an external stress. Nearly all the skeletal vibrations exhibit changes of 1  $\text{cm}^{-1}$  or more at a 0.18 GPa load. However, most of the ring deformation and C-H vibrations remained essentially constant as expected. These frequency shifts are reversible and proportional to the stress applied. It is interesting that the macroscopic modulus

measured for these films is generally in the 15-22 GPa range, much lower than measured for the corresponding PBT fibers [21]. By using the force constant generally associated with the single bond ( $\sim 5$  mdyne/ $\text{\AA}$ ) connecting the phenyl ring to the heterocyclic ring and the cross sectional area ( $\sim 10 \text{ \AA}^2$ ) measured for a PBT chain [31], the theoretical modulus is estimated to be roughly 500 GPa, a value much higher than measured. These comparisons are important and demonstrate the usual difficulty in relating the macroscopic stress to the changes at the molecular level, even for these highly ordered films processed from anisotropic liquid crystalline state.

The most interesting band is the perpendicular polarized  $1252 \text{ cm}^{-1}$  band of medium intensity. The frequency of this band is lowered to  $1249 \text{ cm}^{-1}$  for a 0.18 GPa stress. Representative spectra are shown in Figure 6. The frequency variation as a function of applied stress is shown on Figure 7. It is generally accepted that in stressed polymers, bonds weaken, causing a decrease in the force constants, therefore, a frequency shift is observed. Therefore, the sensitivity of this perpendicular band is perhaps surprising since skeletal modes with transition moments parallel to the drawing direction are generally more sensitive to the applied stress [4-6].

Furthermore, although the frequency of this perpendicular band is sensitive to the stress applied, it can also be affected by sample preparation. For highly oriented PBT films (sheared UMass films and extruded ribbons from Celanese), it is located at  $1251.8 \text{ cm}^{-1}$ , but for the as-polymerized resin (in KBr), it is located at  $1249.2 \text{ cm}^{-1}$ . In certain experimental polymers, "swivel" segments are added forming copolymers of PBT. The composition of the copolymer

measured for these films is generally in the 15-22 GPa range, much lower than measured for the corresponding PBT fibers [21]. By using the force constant generally associated with the single bond ( $\sim 5$  mdyne/ $\text{\AA}$ ) connecting the phenyl ring to the heterocyclic ring and the cross sectional area ( $\sim 10 \text{ \AA}^2$ ) measured for a PBT chain [31], the theoretical modulus is estimated to be roughly 500 GPa, a value much higher than measured. These comparisons are important and demonstrate the usual difficulty in relating the macroscopic stress to the changes at the molecular level, even for these highly ordered films processed from anisotropic liquid crystalline state.

The most interesting band is the perpendicular polarized  $1252 \text{ cm}^{-1}$  band of medium intensity. The frequency of this band is lowered to  $1249 \text{ cm}^{-1}$  for a 0.18 GPa stress. Representative spectra are shown in Figure 6. The frequency variation as a function of applied stress is shown on Figure 7. It is generally accepted that in stressed polymers, bonds weaken, causing a decrease in the force constants, therefore, a frequency shift is observed. Therefore, the sensitivity of this perpendicular band is perhaps surprising since skeletal modes with transition moments parallel to the drawing direction are generally more sensitive to the applied stress [4-6].

Furthermore, although the frequency of this perpendicular band is sensitive to the stress applied, it can also be affected by sample preparation. For highly oriented PBT films (sheared UMass films and extruded ribbons from Celanese), it is located at  $1251.8 \text{ cm}^{-1}$ , but for the as-polymerized resin (in KBr), it is located at  $1249.2 \text{ cm}^{-1}$ . In certain experimental polymers, "swivel" segments are added forming copolymers of PBT. The composition of the copolymer

is 90 molar percent PBT and 10% swivel. As a result, this band in this copolymer is shifted to  $1247.6\text{ cm}^{-1}$ . This kind of copolymer does not exhibit an isotropic to anisotropic transition in solution. The film formed is of much lower orientational order when compared to PBT. Therefore, our observations suggest a correlation between the frequency of this band and the uniformity and magnitude of intermolecular interaction providing an alternative explanation for the frequency shift in stressed PBT.

Although the frequency shifts are the most noticeable change, it should be mentioned that the band shapes are perturbed as well. For example, the  $1249\text{ cm}^{-1}$  band in the stressed polymer exhibits a definite increase in the intensity at the low frequency side of the central peak. This is similar to the behavior observed for typical stress-sensitive infrared bands in semicrystalline polymers [5,6]. As discussed earlier, the frequency shift is proportional to the applied stress. The "tail" of a vibrational band developed in stressed polymer is usually interpreted as being caused by the non-uniform stress distribution at the microstructural or molecular level. Although the macroscopic stress applied is uniform, the actual stress at the microstructural level may be heterogeneous due to conformational or packing defects. For similar strain, some of the bonds or regions may be loaded much more than the sample taken as a whole forming the so-called "overstressed bonds" vibrating at lower frequencies [5,6]. In flexible chain, semicrystalline polymers, amorphous regions usually consist of random coils, chain folds, tie chains and cilia. The disordered structures (macro or micro) in these PBT films have not been characterized sufficiently to provide a phenomenological mechanism relating macroscopic load to the molecular

level in order to explain the frequency change.

Although a definitive explanation for the changes of band shape is still lacking, we have given particular attention to the time dependence of the spectroscopic changes observed. It is interesting to note although the frequency recovers to the original position almost instantaneously, the band shape does not. In Figure 6, curve C was measured immediately after the load was released. In this case, the frequency of the central peak is  $1251.6\text{ cm}^{-1}$  as compared to the  $1251.8\text{ cm}^{-1}$  in the original sample. However, the shape does not fully recover until 18 hours after the load was released. Similar observations can be seen in the stress-relaxation experiments as shown in Figure 8. Curve A was taken immediately after a load (0.18 GPa) was applied. In this case, the frequency of the central peak shifts to  $1249.7\text{ cm}^{-1}$  from the original  $1252\text{ cm}^{-1}$ . After 140 sec, the central peak shifts slightly to  $1249.9\text{ cm}^{-1}$  (curve B). However, the intensity on the low frequency side decreased substantially as a function of time.

### C. Protonation Effect

Since the only known solvents for these polymers are the powerful acids sulfuric acid ( $\text{H}_2\text{SO}_4$ , 100%), methane sulfonic acid (MSA), chlorosulfonic acid (CSA) and polyphosphoric acid (PPA), it has been postulated that these polymers exist in protonated forms in strong acids and with the addition of water form aggregates [22]. Even though cryoscopic studies have determined that at least three protons are associated with polymers in the solution state [23], the location of these charges and the changes in the structures are largely unknown.

In our previous study [12], the analysis of the electronic and vibrational spectra of the model compounds, in conjunction with X-ray and conformational energy calculations have clarified one aspect of these heterocyclic molecules, i.e. the electronic delocalization between the phenyl and the heterocyclic rings. We have extended our Raman spectroscopic study to the analysis of protonated structure.

### 1. Experimental

PBT and t-PBT model compounds were furnished by Dr. A. Fratini of the University of Dayton and Captain Wellman of the Materials Laboratory, Wright-Patterson Air Force Base, Ohio. Unlike the polymer, the model compounds can be dissolved in nonprototic solvents such as CHCl<sub>3</sub>. The concentration used was 1 mg/1 ml of CHCl<sub>3</sub>. Trifluoro acetic acid was gradually added to this solution until the desired acid concentration was obtained.

Since the acid used was corrosive, we did not attempt to obtain infrared data for polymers or model compound in strong acid solutions. For the samples we did try, the strong infrared bands associated with solvents generally masked the bands from the polymer or model compounds. In contrast, even for such dilute solutions, Raman data obtained was of exceptional high signal to noise ratio. Data acquisition was with a computer-controlled Jobin-Yvon HG.2S Raman spectrometer. For quantitative relative intensity measurements, the 760 cm<sup>-1</sup> CHCl<sub>3</sub> band served as an internal standard. The Raman spectrum of PBT polymers in methane sulfonic acid is shown in Figure 9. The solid state spectrum is shown in Figure 10. In this case, the Raman spectra were obtained using less

than 15 mw of laser power and a rotating cell (front surface reflection method) in order to minimize the possibility of thermal degradation. The Raman data obtained for the model compound are shown in Figure 11.

Solution ultraviolet and visible absorption spectra were obtained with a Beckman Acta VI spectrometer. Representative spectra of the polymer and of the model compound are shown in Figures 12 and 13 respectively.

## 2. Structural Analysis of Protonated Molecules

Although all the model compounds contain a number of lattice vibrations below  $100\text{ cm}^{-1}$ , no Raman bands of significant intensity were observed below  $900\text{ cm}^{-1}$  for the polymers. The Raman spectrum of PBT polymer in the solid state exhibits only a few modes with intense bands at  $1481\text{ cm}^{-1}$  and  $1605\text{ cm}^{-1}$ . The spectrum is far simpler than the corresponding infrared spectrum. This is because of the high selectivity of the Raman scattering process. In Raman spectroscopy, when the frequency of the incident laser excitation radiation is close to or coincident with the frequency of an electronic absorption band of the molecule, enhancement of the scattered Raman intensity is expected [24]. In addition, only the Raman bands coupled to the electronic transitions at or near the frequency of the laser excitation are resonance enhanced. Not surprisingly, as can be seen on Figures 12 and 13, the electronic absorption obtained for these conjugated heterocyclic polymers and its model compounds all exhibit strong absorptions in the  $300 - 450\text{ nm}$  region presenting the possibility that the scattered Raman intensities may be resonance enhanced. Because of the fluorescent background, we could not quantitatively measure the dependence of Raman intensity as a function of the excitation wavelength. However

as reported earlier [12] for t-PBT the normalized Raman intensity (using excitation wavelength varying from 4579 - 5145 Å) was found to vary significantly with excitation wavelength.

Identical Raman spectra were obtained for the pressed pellet or films of PBT polymer. The dissolution of PBT in acid is essentially a result of protonation of the heteroatoms on the polymer backbone. This causes changes which affect the interchain interaction (van der Waals) sufficiently to facilitate the dispersion of molecules. In solution, the Raman spectrum of PBT shows intense bands at 1610, 1515, 1295 and 1218 cm<sup>-1</sup>. These spectral features are independent of PBT polymer concentration from 0.01% to 14% (mg/ml) in acid (MSA). Since the isotropic to nematic phase transformation occurs near 5% concentration, the spectral changes cannot be associated with the change in the intermolecular interaction, but rather with the structure of the polymer. On the basis of the vibrational spectra obtained for biphenyl and heterocyclic model compounds [26-30], the Raman bands observed were assignable to the stretching vibrations of the heterocyclic group, the phenyl ring and the C-C bond linking them [12]. The changes observed for these backbone motions are interesting and need to be analyzed in order to interpret the structural aspects in both the solid and the solution states. However, because of the extreme simplicity of the Raman spectrum, a proper interpretation of the changing spectral features is difficult. Hence, we intend to examine the electronic absorption and vibrational spectra of the four model compounds (t-PBT, c-PBT, t-PBO, c-PBO), as a basis for understanding spectra of the polymers.

Since all the model compound can be dissolved in nonprotonic solvent such as

$\text{CHCl}_3$ , the spectroscopic changes as a function of relative acid concentration is of high interest. For the t-PBT model compound in  $\text{CHCl}_3$ , two strong electronic absorptions were found at 246 nm and 346 nm close to the visible region. The peak around 246 nm can be assigned to the phenyl end groups. This assignment is consistent with the observations for biphenyl [31]. In that case the absorption maxima were found at 238, 246 and 251 nm for biphenyl in the vapor, solution and crystalline forms respectively. The 346 nm maxima can be associated with the absorption of the heterocyclic group. Its position can shift to as high as 440 nm in PBT polymer dissolved in MSA. For the t-PBT model compound in acid, this absorption maximum shifted upward by 19 nm to 365 nm when compared to  $\text{CHCl}_3$  solution; the second component for t-PBT model compound can be found at 266 nm in acid. No further spectroscopic changes were found for solutions containing acid concentrations greater than 5%. This progressive upward shift of this absorption band from the model compound to the polymer is consistent with the known fact that the absorption maximum,  $\lambda_{\max}$ , increases with increasing chain length, that is, a greater degree of delocalization. Therefore, the upward shift of absorption maximum as a function of acid concentration may be associated with an increase in the electron delocalization between the main heterocyclic ring and the phenyl ring in the protonated structure.

This interpretation can be supported by the analysis of biphenyl. In that case the absorption maximum has been related to the degree of the coplanarity of the two benzene rings or the degree of electron delocalization [31]. The absorption maximum for the phenyl ring is observed at 238 nm and 251 nm for the least conjugated (vapor phase) and the most conjugated structures (solid phase)

respectively.

### 3. Dilution Experiments: On the Reversibility of Protonation of PBT

Two types of dilution experiments were carried out in order to examine the reversibility of the protonation. In the first set of experiments the donor ( $\text{F}_3\text{COOH}$ ) - acceptor (t-PBT model compound) molar ratio was kept constant, and the starting solution was diluted with chloroform. In the second set of experiments the solute concentration in  $\text{CHCl}_3$  solution was kept constant, and the acid concentration was increased by adding  $\text{CF}_3\text{CO}_2\text{H}$ . The UV-visible absorption and the Raman spectra obtained show that the process of protonation is completely reversible.

To complement the UV-visible spectroscopic studies, vibrational spectra of the model compounds were also obtained to analyze the protonation process. As expected, the intense low frequency lattice modes ( $10 - 100 \text{ cm}^{-1}$ ) were unobservable for the model compounds in solution. There are also substantial spectral changes as a function of acid concentration. The observed Raman bands can be divided into three categories. These are: (1) the bands that are clearly observable for acid concentration below 0.1%; (2) the bands that are observed for solutions containing acid concentration 5% or higher; (3) the bands that are only clearly observable for solutions containing acid concentrations between approximately 0.1% and 5%. The normalized intensities and their changes (relative to the  $760 \text{ cm}^{-1}$   $\text{CHCl}_3$  band) of the Raman bands are tabulated in Tables 3 and 4. A transition seems to occur for acid concentration between 0.1% and 5%. It is probable that the first and second sets of Raman bands can be assigned to the unprotonated and fully protonated structures, respectively. The

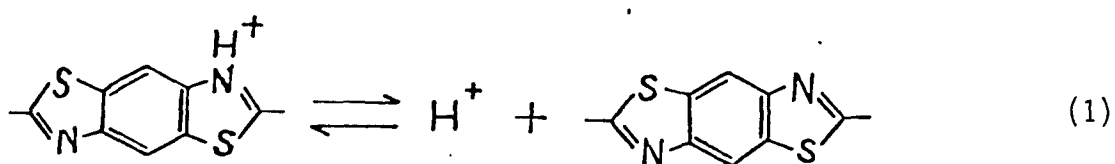
appearance and disappearance of some of the bands with change in the acid concentration is intriguing. One possible explanation is the different pK value associated with the two nitrogen atoms on the heterocyclic ring. The nitrogen atom of one side should be protonated and then followed by the protonation of the other side at a considerably higher acid concentration.

#### 4. Determination of the Spectroscopic Features of Half Protonated and Fully Protonated Species

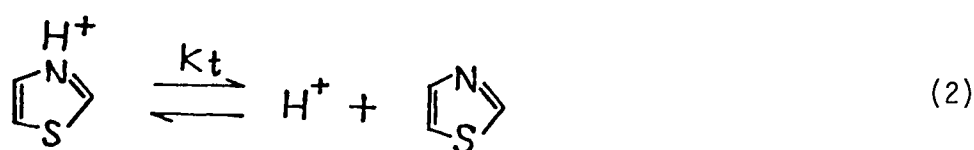
For the twelve Raman spectra varying only in acid concentration, we have used factor analysis [32] to establish that there indeed are three linearly independent components giving rise to all the spectra obtained. Four methods of factor analysis have been evaluated, as mentioned in a previous work [32]. Although each method is satisfactory for model systems, in some cases, the results derived from one method may not be conclusive in assigning the number of components in polymer spectroscopy. Our mathematical methods explicitly incorporate measurement errors in the algorithm. This type of analysis has proved to be quite useful in detecting and deconvoluting the characteristics of conformational and packing defects in semicrystalline polymers [32]. In our analysis, we have incorporated the average random noise above the baseline as our measurement error. The result of our analysis clearly shows the existence of three linearly additive components for the twelve spectra containing different acid concentrations.

It seems reasonable, then, to assume these three linearly additive components are associated with three structures (unprotonated, half-protonated and

fully protonated). Their relative abundance depends on the acid concentration. The acid concentration needed to protonate one of the two t-PBT nitrogen atoms can be approximated as follows: The equilibrium state to be considered is:



which can be approximated by the thiazole protonation equilibrium:



for which the pK value is 2.4. Considering the t-PBT model compound to be 2 thiazoles and from the definition of pK and the equilibrium constant we find

$$k_t = 10^{-pK} = 0.004 = \frac{[\text{H}^+] \left[ \text{---S---} \text{C}_3\text{H}_3\text{N---S---} \right]}{\left[ \text{H}^+ \text{---} \text{S---} \text{C}_3\text{H}_3\text{NH---S---} \right]} \quad (3)$$

The situation we are considering corresponds to an equal concentration of unprotonated and half-protonated structures. This leads to the acid concentration needed as 0.004 (g/ml). For  $\text{CF}_3\text{CO}_2\text{H}$ , the density is  $1.535 \text{ g/cm}^3$ ,

and molecular weight 114.03 g/mole. The concentration of acid needed to protonate half of the t-PBT molecules is calculated to be 0.03%. This estimated value is lower than the observed value of 0.1%. This may be due to the insensitivity of the spectroscopic methods to quantitatively distinguish the two structures until the bands associated with each is of sufficient intensity. Because of insufficient sample we could not carry out a titration experiment to measure the pK value associated with the second nitrogen atom. However, the addition of a second nitrogen to the same molecule usually results in the basicity of the second nitrogen being several orders of magnitude less than the first nitrogen. Taking the pK value of the second nitrogen  $pK_2$  to be  $pK_1 - 2$ , leads to an acid concentration needed for full protonation to be about 3%. We observed the disappearance of some Raman bands for an acid concentration of about 5%. The 1410 and the  $1334\text{ cm}^{-1}$  bands can be associated with the half protonated molecule. They are clearly observable for acid concentrations between 0.1% to 5%. Their intensities are at maximum for the 3% acid concentration solution. For the fully protonated molecule these bands are no longer present.

To complement the UV and visible spectroscopic studies, the Raman spectra were analyzed in order to elucidate the structural changes due to protonation. From group frequency analysis, the bands of significant intensity in the  $1100\text{ cm}^{-1}$  to  $1600\text{ cm}^{-1}$  region are likely assignable to the stretching vibrations of the central heterocyclic group, the outer phenyl ring and the C-C bond linking them.

A band at  $1608\text{ cm}^{-1}$  exists in the spectrum of solid t-PBT model compound. This band has been previously assigned to the ring stretching vibration of the

terminal phenyl ring. The dramatic intensity changes in the Raman spectra obtained for various model compounds have been interpreted by variations in the dihedral angle between the plane of the phenyl group and the plane of the central heterocyclic ring, thus affecting the resonance configuration between the two rings [12].

The investigations on sterically hindered biphenyls by Schmid and Brosa [26] show that there exists a quantitative relationship ( $\cos^2 \theta$  law) between the Raman intensity of the ring stretching vibration at  $1600\text{ cm}^{-1}$  and the angle of twist. When the rings are coplanar as in fluorene, the Raman intensity has its largest value. When the rings are at large angles the resonance stabilization does not take place and the Raman lines will be weak [26]. In our previous study [12], the structure for a number of model compounds deduced from our Raman spectroscopic analysis are consistent with their x-ray diffraction structures and theoretical conformation analysis. It has been shown in the usual vibrational analysis [33,34] the frequency of this phenyl ring stretching vibration is also sensitive to the degree of interaction between the phenyl ring and the heterocyclic group. For our t-PBT model compound in  $\text{CHCl}_3$ , this  $1608\text{ cm}^{-1}$  band is present as a weak band. Its intensity increased significantly as a function of acid concentration. In addition a frequency shift is observed to  $1622\text{ cm}^{-1}$ . Therefore, the Raman spectroscopic changes suggest an increase in conjugation between the phenyl ring and the heterocyclic ring. This interpretation is consistent with the UV-visible absorption analysis.

The  $1277\text{ cm}^{-1}$  band of medium intensity is observed in the Raman spectrum of t-PBT model compound. This band can be assigned to the C-C stretching vibration

associated with the bond connecting the phenyl ring to the main heterocyclic ring [12]. As the acid concentration increases, a second component at  $1294\text{ cm}^{-1}$  can be observed in this region. Finally, for samples containing more than 10% acid, the  $1277\text{ cm}^{-1}$  band disappeared completely. From x-ray studies the length of this bond in the solid state is  $1.49\text{ \AA}$  [35], intermediate between the values usually associated with the double bond ( $1.34\text{ \AA}$ ) or single bond ( $1.54\text{ \AA}$ ). The increase in the frequency of this stretching mode may be associated with the increase in conjugation between the groups as a result of protonation. For other model compounds of these heterocyclic polymers the frequency of this C-C stretching has been directly related to the degree of conjugation [12].

The  $1313$ ,  $1479$ , and  $1507\text{ cm}^{-1}$  bands exhibit similar variations with respect to the increase in protonation. The  $1507\text{ cm}^{-1}$  band is the most intense band observed for the t-PBT model compound. These bands shift to  $1322$ ,  $1487$  and  $1524\text{ cm}^{-1}$  respectively for solutions containing high acid concentration. For solutions containing acid concentration between  $0.1\%$  to  $5\%$ , these bands broadened before narrowing for solution containing acid concentrations greater than  $5\%$ . The precise origins of these three bands are unclear. We have assigned these three bands to contain a significant amount of C ... N stretching vibrations [12,27-30]. The isolated C=N stretching mode usually absorbs at approximately  $1650\text{ cm}^{-1}$ . In conjugated molecules such as oxazole, thiazole, imidazole, benzoxazole, benzimidazole, pyridine, etc., there is such a strong interaction between the C=N and C=C stretching vibrations that they completely lose their individual identity. As a result, a complex series of bands usually appears in the aromatic stretching region between  $1600 - 1300\text{ cm}^{-1}$  [12,27-30].

When the nitrogen atom is protonated, there is an increase in the electron density of a carbon atom adjacent to the nitrogen [36]. Intuitively, by protonation, the electronic charge is withdrawn toward the nitrogen from all positions of the ring. This structural change may cause the frequency increase associated with these three bands.

The 1446 and 1597  $\text{cm}^{-1}$  bands are assignable to the  $\nu_{1g}$  and  $\nu_g$  vibrations of the central phenyl ring [37]. This assignment is consistent with the observations in substituted benzene. From our experiments, these intensity variations are quite sensitive to the degree of protonation. As can be seen in Figure 11, the intensity of the 1597  $\text{cm}^{-1}$  band continues to increase with increasing acid concentration. In contrast, the intensity of the 1446  $\text{cm}^{-1}$  band is at maximum for solution containing 3% acid before diminishing. It is known that the optical activities of these two bands are very sensitive to the symmetry group present [37]. The vibration at 1446  $\text{cm}^{-1}$  is only present in Raman spectra for molecules of lower symmetry than the one for benzene ( $D_{6h}$ ). It is possible therefore, that the intensity variations observed are indicative of the structural changes due to protonation. In the unprotonated or half-protonated molecule, this band is of medium intensity. When the molecule is fully protonated, the phenyl ring and the main ring may reach a coplanar state of higher symmetry group ( $C_{2h}$ ). For this structure this band should be optically inactive.

TABLE 1  
Infrared Bands Observed for Highly Oriented PBT Film

Frequency (cm <sup>-1</sup> )	Intensity	Polarization Directions	Tentative Assignment
3076	w	y	20b 1,4-C <sub>6</sub> H <sub>4</sub>
3050	sh		20a 1,2,4,5-C <sub>6</sub> H <sub>2</sub>
3027	w	z	20a 1,4-C <sub>6</sub> H <sub>4</sub>
1605	w	z	8a 1,4-C <sub>6</sub> H <sub>4</sub> , 1,2,4-5C <sub>6</sub> H <sub>2</sub>
1532	m	z	19a 1,4-C <sub>6</sub> H <sub>4</sub>
1500	sh		19a 1,2,4,5-C <sub>6</sub> H <sub>2</sub>
1485	vs	z	Hetero ring stretch
1428	m	z	19b 1,2,4,5-C <sub>6</sub> H <sub>2</sub>
1410	s	y	19b 1,4-C <sub>6</sub> H <sub>4</sub>
1401	s	z	Hetero ring stretch
1314	vs	z	Hetero ring stretch
1252	s	y	Crystalline band
1211	w	z	C-C stretch
1113	m	y	18b 1m4-C <sub>6</sub> H <sub>4</sub>
1056	m	z	18a 1,4-C <sub>6</sub> H <sub>4</sub>
1017	w	x	18a 1,2,4,5-C <sub>6</sub> H <sub>2</sub>
960	vs	z	Hetero ring "breathing"
860	s	y	11 1,2,4,5-C <sub>6</sub> H <sub>2</sub>
837	s	x	11 1,4-C <sub>6</sub> H <sub>4</sub>
732	w	z	Hetero in-plane ring deformation
705	m	z	12 1,4-C <sub>6</sub> H <sub>4</sub>
689	s	z	Hetero ring stretch
627	w	z	6b 1,4-C <sub>6</sub> H <sub>4</sub>
605	s	y	Hetero out-of-plane ring deformation
488	m	y	Hetero out-of-plane ring deformation

w = weak, m = medium, s = strong intensity, sh = shoulder

TABLE 2  
The frequency shift of PBT infrared bands under  
mechanical load (0.18 GPa)

Frequency (cm <sup>-1</sup> )	Shift (cm <sup>-1</sup> )
1532	+ 1.4 <u>±</u> 0.1
1485	1.0
1428	1.7
1410	0.9
1401	1.1
1314	0.9
1252	2.9
1113	0.6
1056	0.4
1017	0.2
960	1.3
860	0.0
837	0.2
732	0.3
705	0.6
689	1.4
627	0.0
605	0.0

Table 3  
 Intensity Variations of Some Raman Bands  
 with Acid Concentration

	% Acid ( $\text{F}_3\text{COO}_2\text{H}$ )		
Band	0%	3%	100%
1278 $\text{cm}^{-1}$	S		0
1294 $\text{cm}^{-1}$			0
			S
	W		
1507 $\text{cm}^{-1}$	VS		0
1524 $\text{cm}^{-1}$	W		VS
1479 $\text{cm}^{-1}$	S		0
1487 $\text{cm}^{-1}$			S
	0		
1622 $\text{cm}^{-1}$			M
1334 $\text{cm}^{-1}$		0	
		M	
1410 $\text{cm}^{-1}$	W	W	0
1597 $\text{cm}^{-1}$	φ		0
			VS
1446 $\text{cm}^{-1}$	VS	V	
	M		0

s = strong, m = medium, w = weak, vs = very strong intensity

Table 4  
 Relative Intensities of Raman Bands  
 $I_x/I_{760} (\text{CHCl}_3) \times 10^{-2}$

$F_3\text{CCO}_2\text{H}\%$

	1314	1322	1334	1347	1410	1462	1597	1622	1446 (area)
0	3.5		1.5				32		(130)
0.2	3.1		2.0				34		(137)
0.5	2.8		3.7				40		(163)
0.75	2.7		4.2		0.7		41		(169)
1	2.24		4.7	1.0	1.0		41		(170)
2	2.0		6.5	1.5	1.7	1.3	44		(174)
3		2.3	8.2	2.1	2.6	2.9	45		(177)
5		4.2	4.4	2.1	1.7	2.8	48		(110)
10		7.2	2.3	2.2	1.3	1.9	53	3.6	(38)
20		9.1	1.7	2.4	1.2	1.4	58	4.8	(30)
30		10					58	8.0	(20)

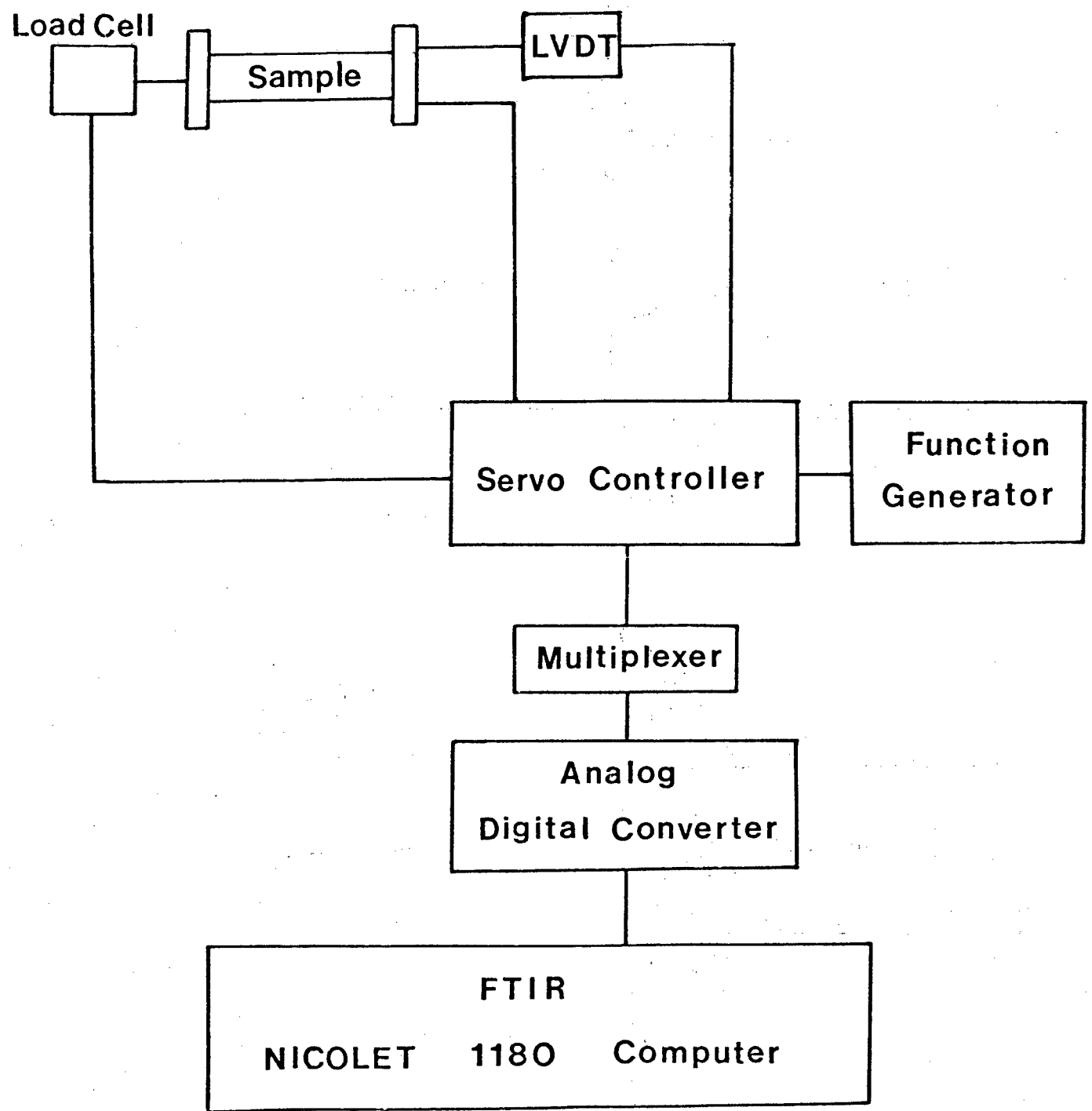


Figure 1. Schematic drawing of the coupling between mechanical deformation and FTIR.

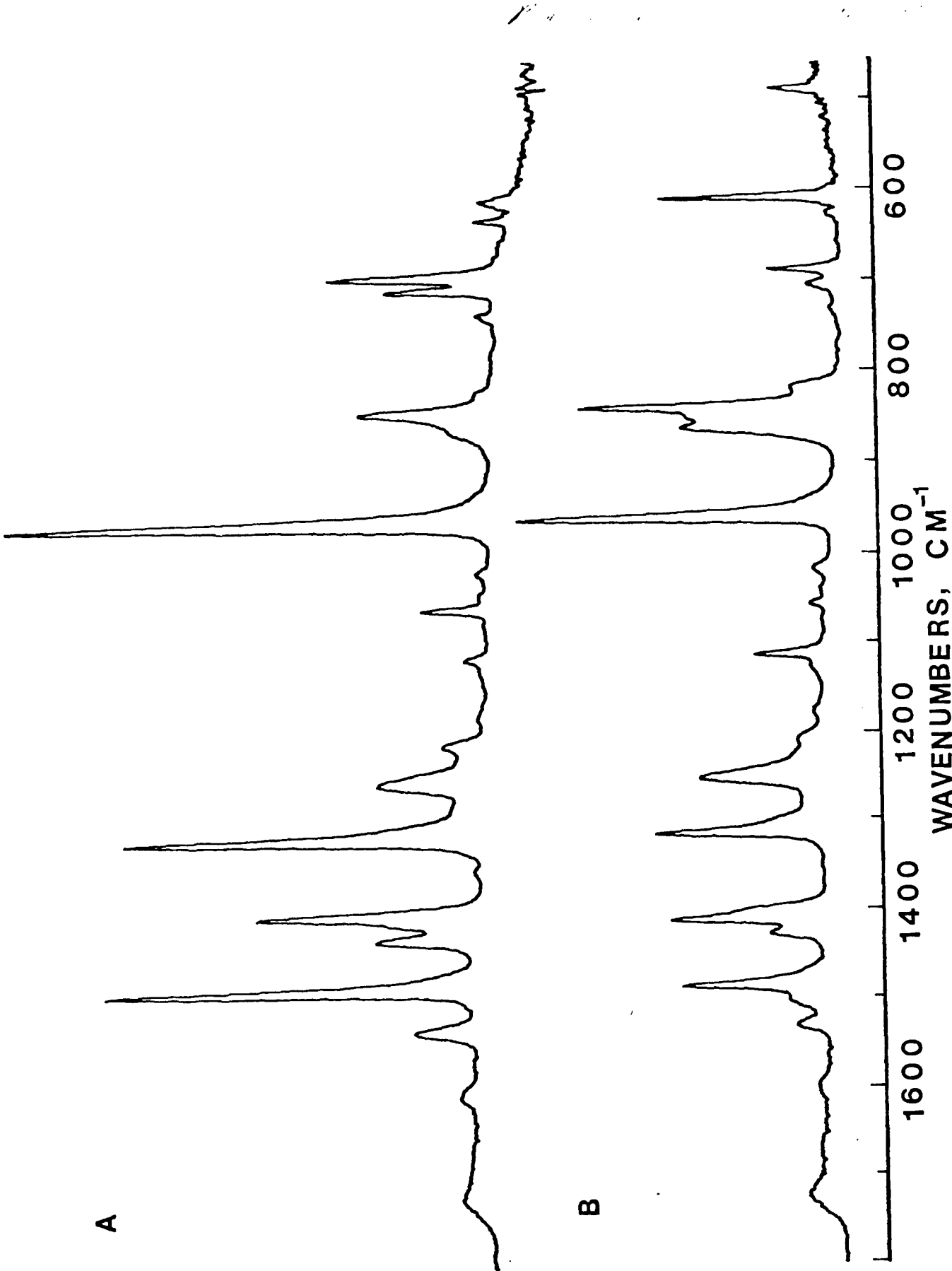


Figure 2. Polarized infrared spectra obtained from highly oriented PBT film:  
A. Parallel polarization; B. Perpendicular polarization.

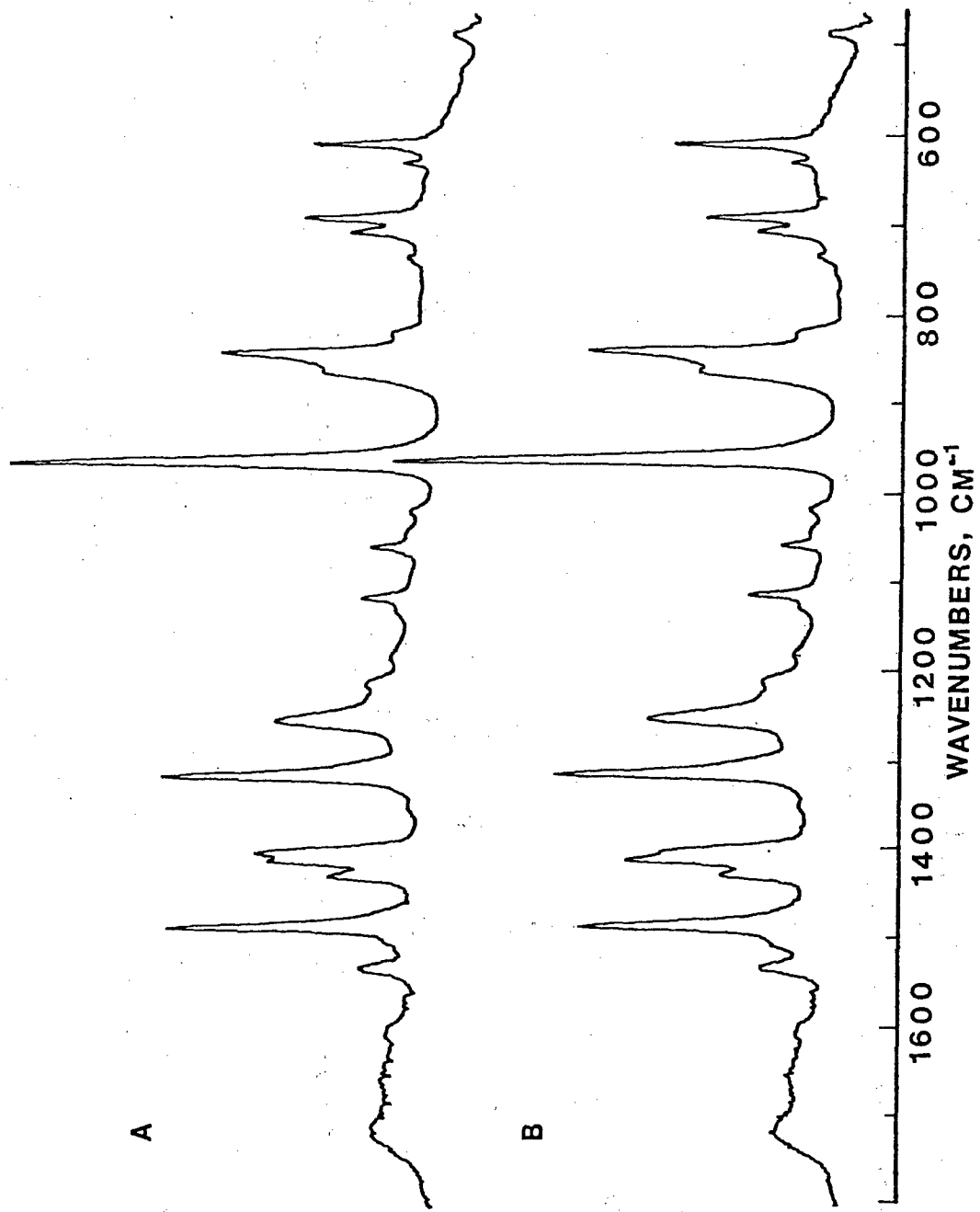


Figure 3. Infrared spectra obtained from highly oriented PBT films: A. Curve corresponds to spectrum taken with film plane perpendicular to the incident radiation; B. Curve corresponds to a 45° rotation.

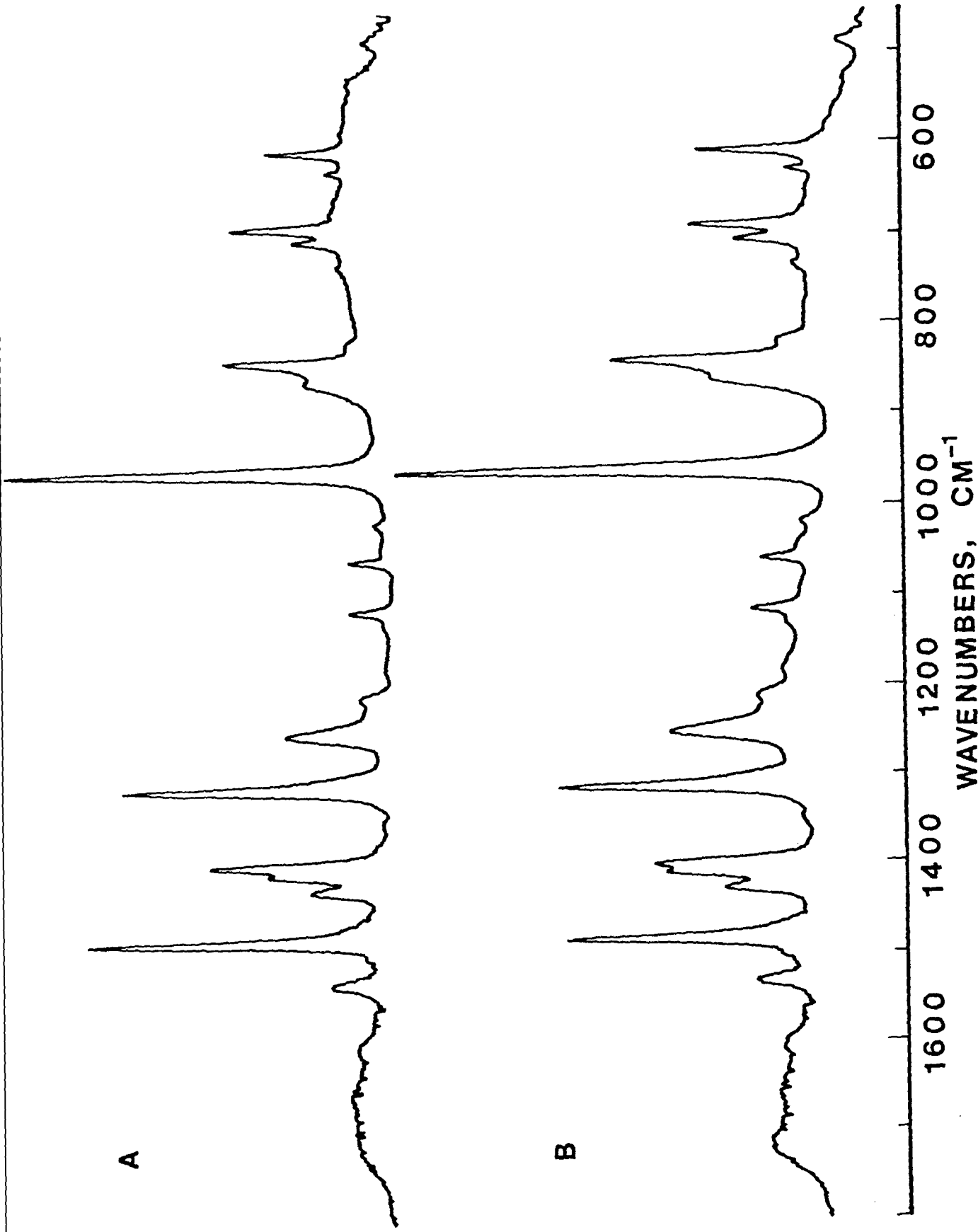


Figure 4. Infrared spectra of PBT:  
A. Taken from an unoriented sample;  
B. Spectrum taken from a highly oriented film.

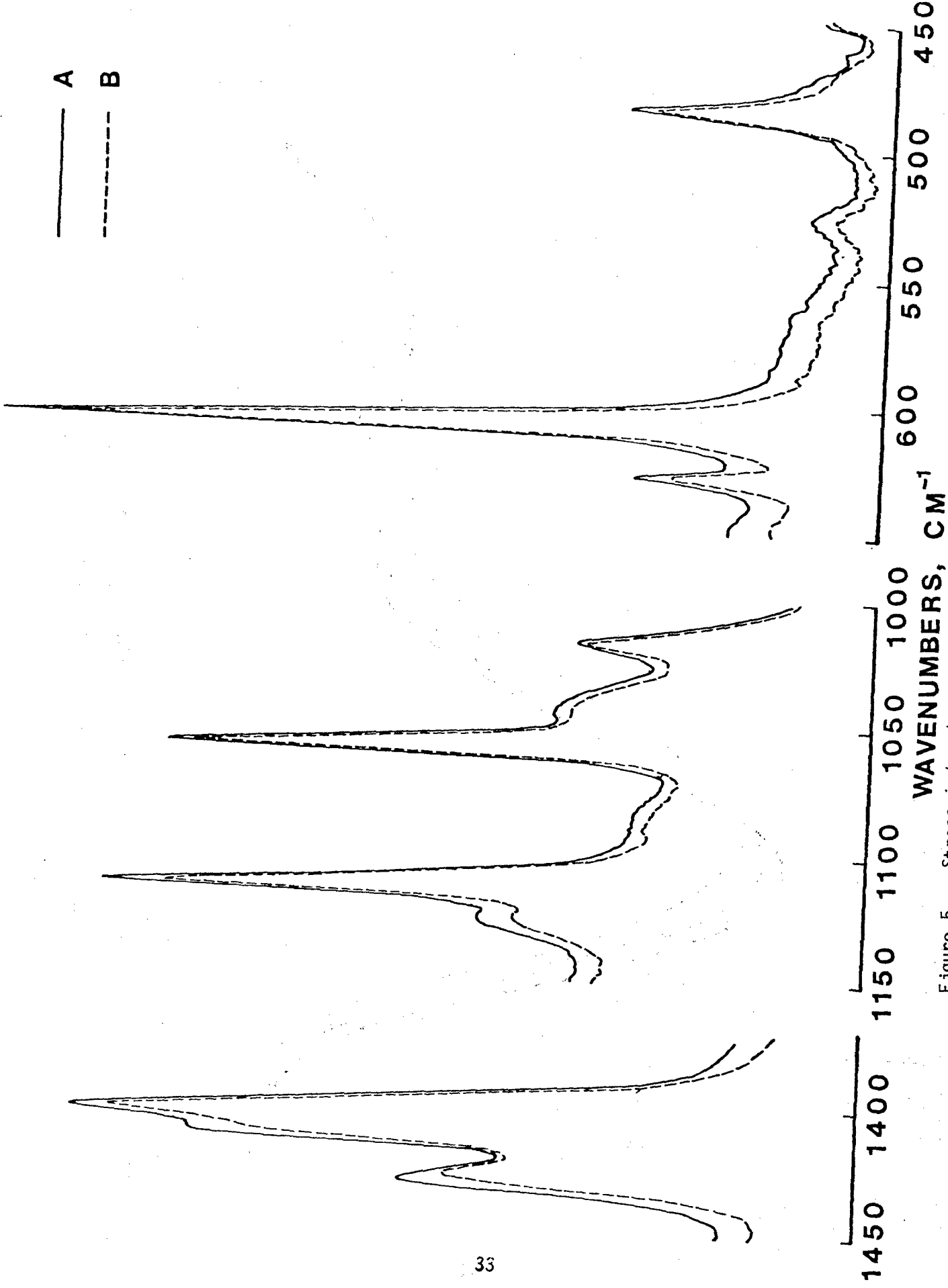


Figure 5. Stress induced relative intensity changes: A. No stress;  
B. 0.18 GPa stress applied.

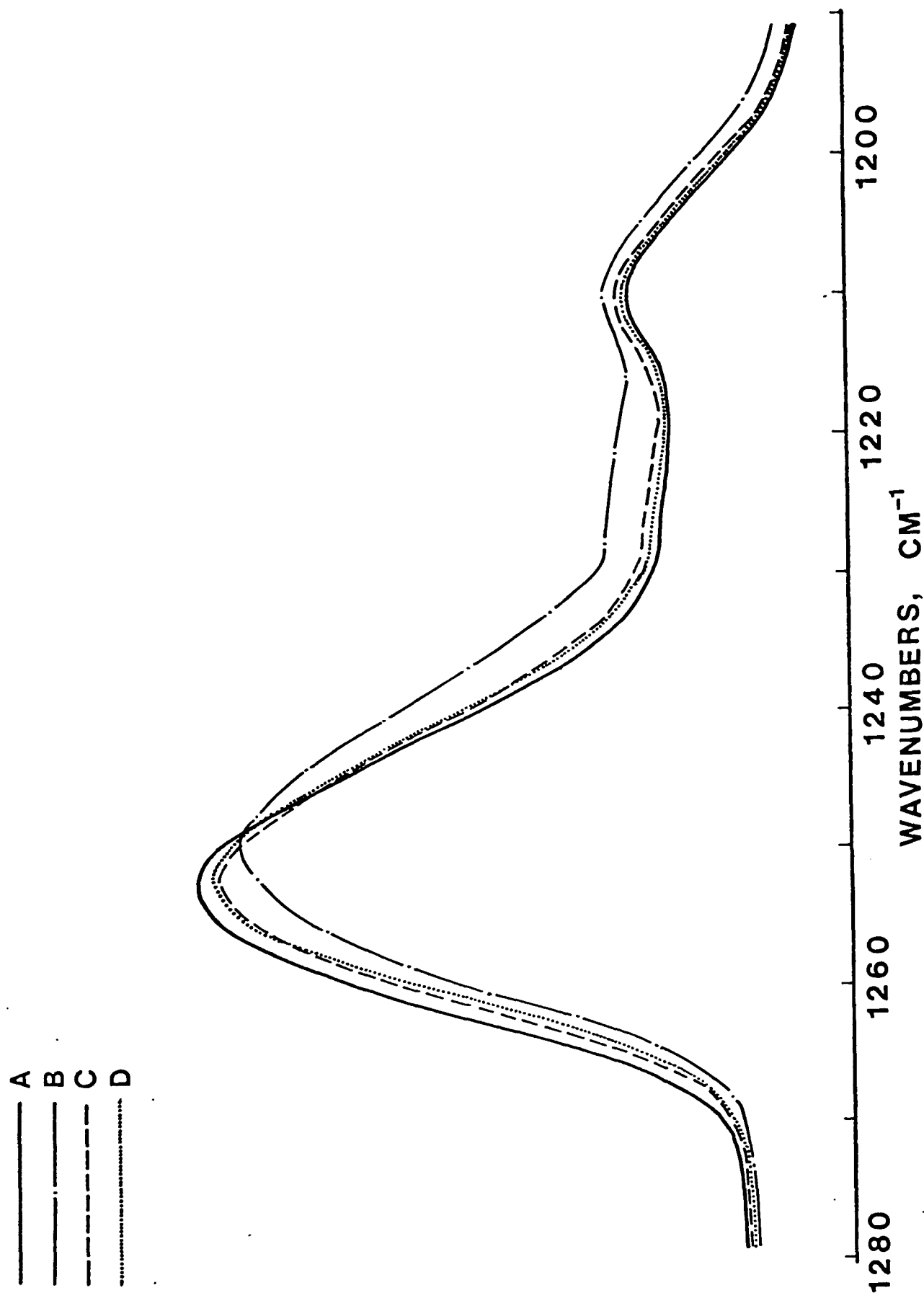


Figure 6. Stress induced spectroscopic changes for the  $1252 \text{ cm}^{-1}$  band in PBT:  
A. No stress; B. 0.18 GPa; C. Spectrum taken immediately after  
stress is released (< 70 sec); D. Spectrum taken from a relaxed  
sample.

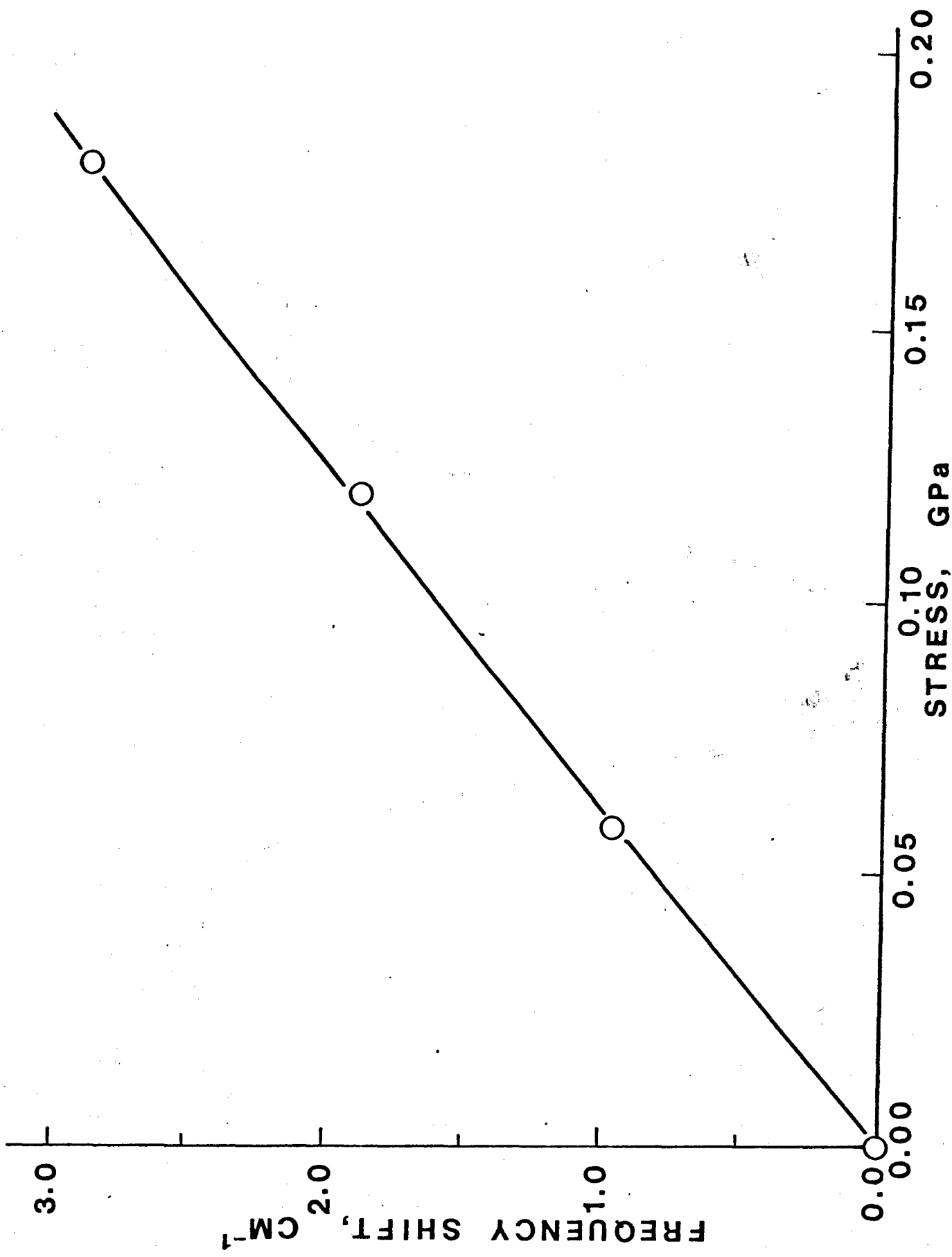


Figure 7. Frequency shift of the  $1252 \text{ cm}^{-1}$  band as a function of stress.

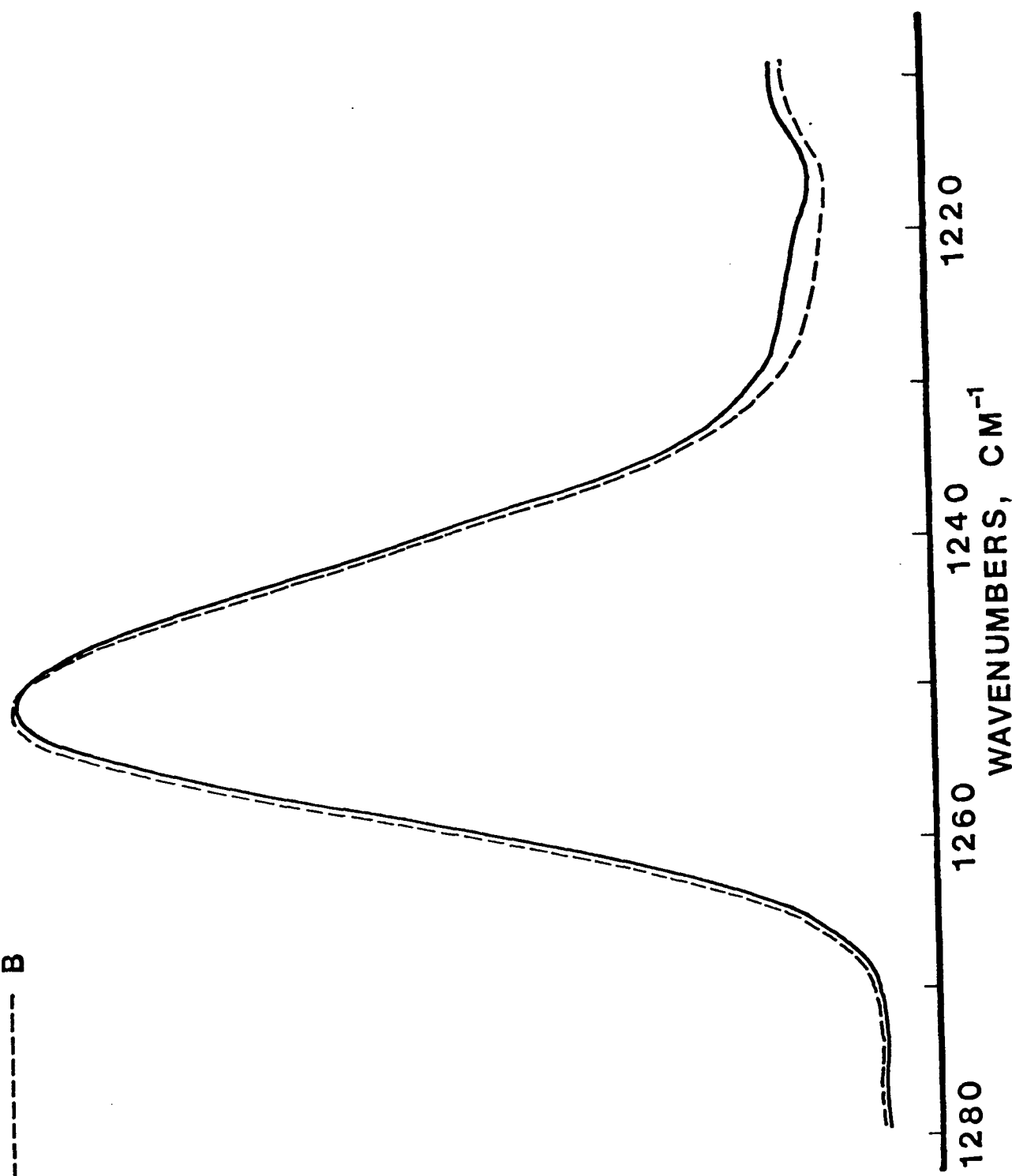


Figure 8. Spectra infrared spectra taken after the stress is applied:  
 A. Immediately after the stress is applied (<0.35 sec, 0.18 GPa);  
 B. Taken after 140 sec. when stress is relaxed to 0.11 GPa.

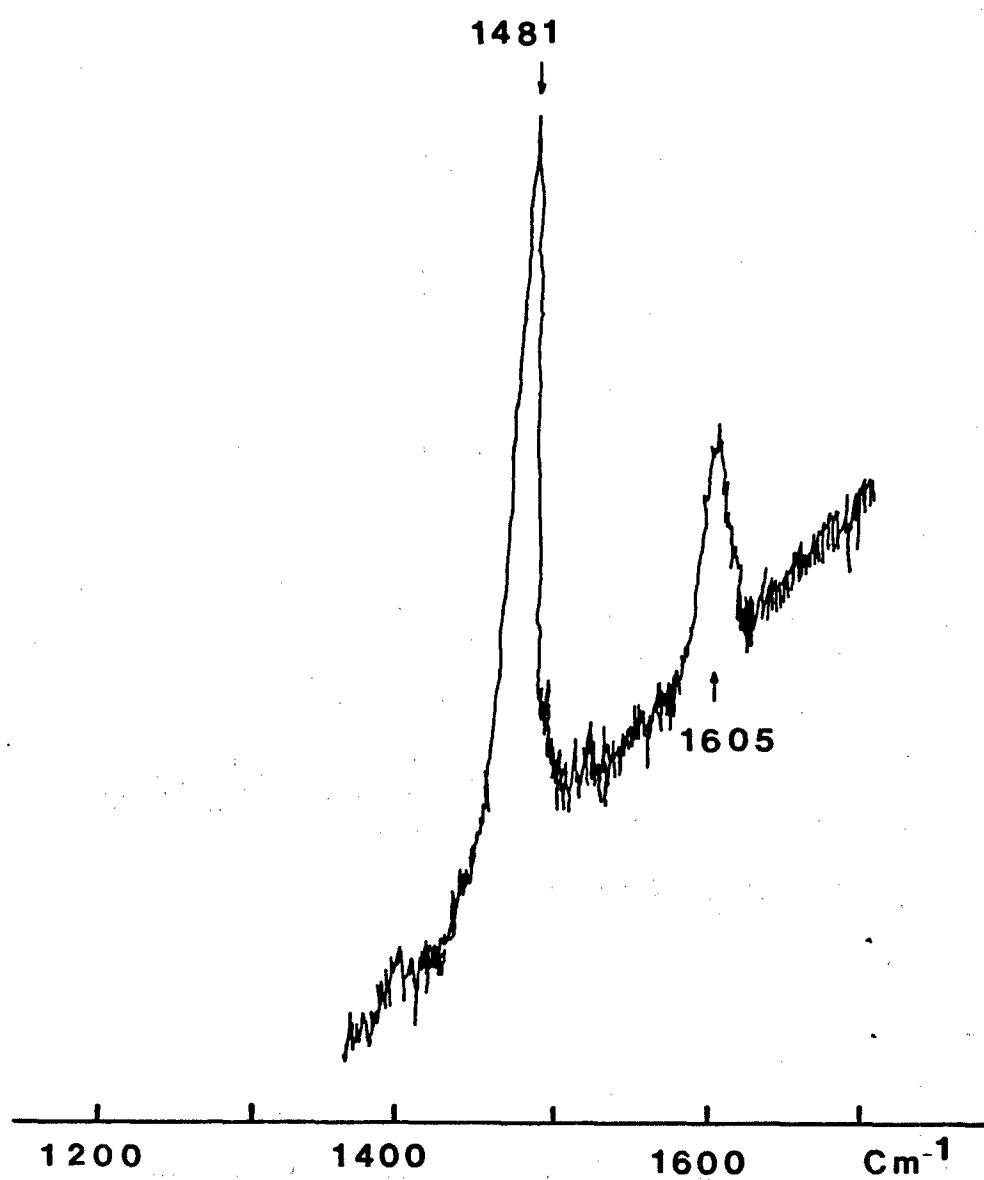


Figure 9. Raman Spectrum of PBT in MSA. Laser Power: 15 mW at 5145 Å;  
Bandpass:  $2 \text{ cm}^{-1}$  at 5100 Å.

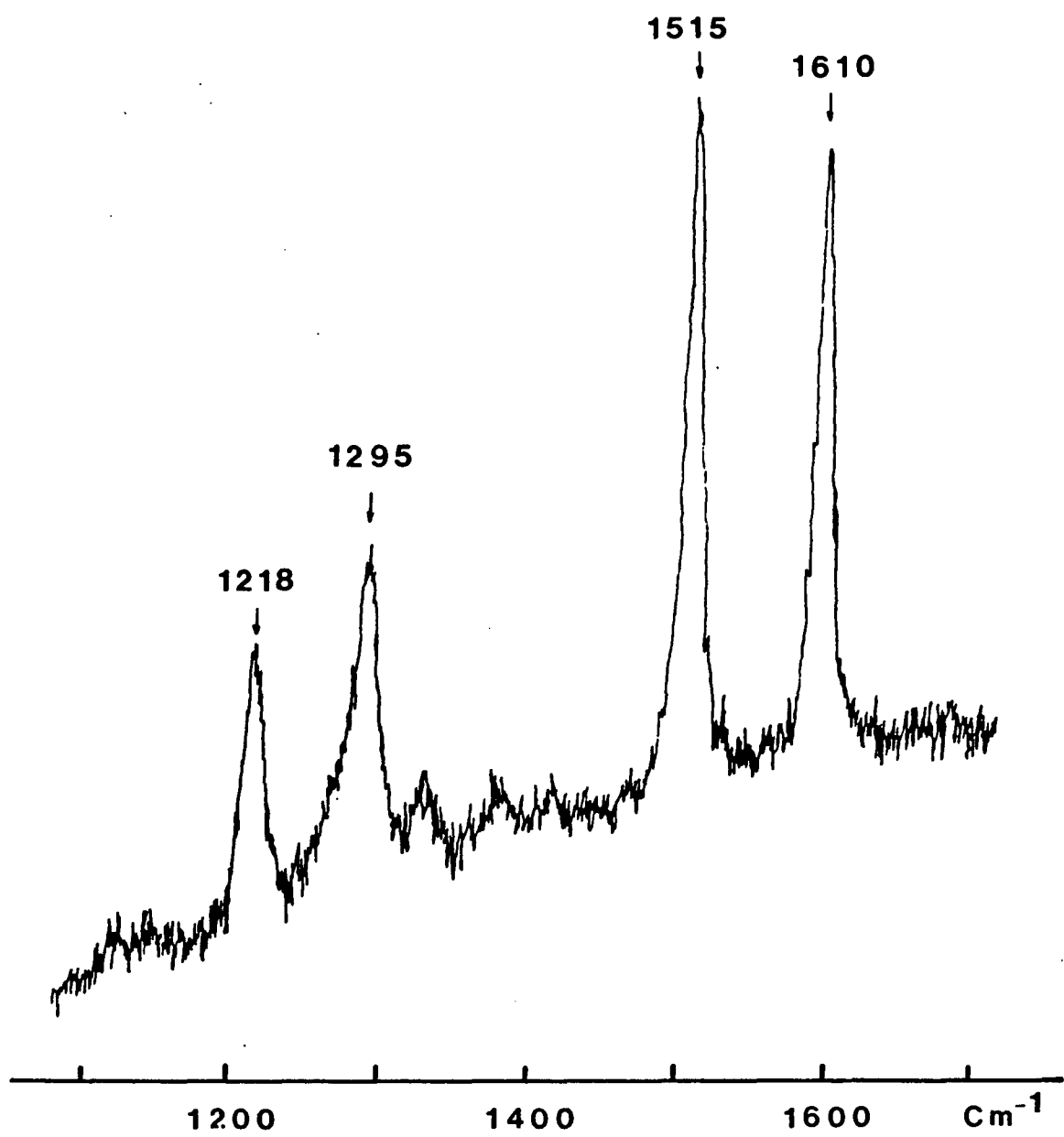


Figure 10. Raman Spectrum of PBT solid. Laser Power: 15 mw at 5145 Å;  
Bandpass:  $2 \text{ cm}^{-1}$  at 5100 Å.

### SECTION III: MORPHOLOGICAL INVESTIGATIONS

In this section we report results of microscopical and scattering investigations of the microstructure of solutions, fibers and ribbons of PBT. The following topics are treated: high resolution dark field imaging and lattice imaging of PBT fibers and tapes, light microscopy of PBT tapes, calculation of the wide angle scattering of a single chain, packing analysis in the PBT unit cell, and small angle x-ray and neutron scattering from PBT solutions, fibers, and tapes.

#### A. High Resolution Dark Field Imaging of PBT Films

The resolution attainable for polymer samples is limited by electron beam radiation damage due to crosslinking or chain scission with subsequent loss of mass. Molecules containing aromatic groups have been found to have improved resistance to beam damage (with respect to aliphatic compounds), presumably due to overall chain rigidity and resonance stabilization of radicals generated by the electron beam. PBT fibers and films have been studied by tilted beam dark field.

The films investigated were prepared by Celanese Research Co. by extrusion from a PPA dope (9.5% solids, Polymer 3895-32, I.V. = 32) through a rectangular die (12.7 mm wide x 0.093 mm thick x 1.7 mm long at 150 mm/min) through an air gap (1.5 mm) onto a casting roller, into a water coagulation bath (at 21°C) over a hot shoe (110°C, 91 sec) and taken up on a movie film reel. The spin draw ratio was 1.3 and the final film width was 5 mm. Typical film properties were: 820 g/den modulus, 7.7 g/den strength for a 750 denier film. Some samples were

continuously heat treated by Celanese (525°C, 0.6% stretch, 32 sec. residence; 475°C, 500 g tension, 32 sec. residence) and small samples were heat treated under load (50 g tension, 30 min. cycle time, 400°C maximum temperature, N<sub>2</sub> atmosphere). After continuous heat treatment typical properties were 870 g/den modulus, 8-11 g/den strength for a 630 den film.

Samples thin enough for TEM were prepared from bulk films by extraction replication with collodion and examined in a JEOL 100 CX operated at 100 KV using Kodak 4463 film. Figure 11 shows the decay of the 2nd, 3rd and 4th equatorial reflections (e<sub>2</sub>, e<sub>3</sub> and e<sub>4</sub>) as a function of electron dose. The intensity is proportional to the current collected from the isolated observation screen when the microscope was operated in the diffraction mode with the appropriate reflections selected with a 5.6 mrad diameter objective aperture. The electron dose was obtained by the method of Grubb [38]. The screen current decays to a plateau value arising from the damaged polymer and the carbon support film. A plot of  $\ln(i(D) - i(\infty))$  vs dose is linear, suggesting that the decay is exponential with a characteristic value,  $D^* = 1.6 \text{ coul/cm}^2$ , required for the diffracted intensity to decrease to 1/e of its original value. By examination of serial DF images, we have found useful images may be obtained up to a total dose of approximately  $D^*$ . Since  $I_{e_2-e_4}/I_{1000} \sim .02$ , and the electron speed for the film and developing conditions employed is approximately 0.8, the maximum dark field magnification is calculated to be 40,000X when focusing is done on an adjacent area [39]. This is an order of magnitude greater working DF magnification than reported for polyethylene.

Figure 12 is an e<sub>2</sub>-e<sub>4</sub> DF image at 33,000X original magnification from an

extracted fragment suspended over a gold decorated, perforated carbon support film. The coherently scattering regions average 10 nm in width and 15 nm in length and are highly aligned in the extrusion direction. The kinked area in the lower right region (marked 'K') shows the effect of tilt about an axis normal to the extrusion direction. The non-diffracting region of the kink also shows that the axial orientation is very high and the Bragg condition is only satisfied for normal incidence of the electron beam.

The top of Figure 12 shows an enlargement of the area within the white box. Several bright coherently scattering regions are separated by small, dark, non-coherently scattering regions (marked "B"). These dark regions may represent buckled regions or defects within the region.

The  $e_1$  dark field image when compared by a transparent sheet overlay technique with that from  $e_2-e_4$  of the same area (Figure 13, instrumental magnification reduced to 10,000X for two successive micrographs) shows a different array of coherently scattering regions of similar size and shape. The size of the coherently scattering regions agrees with the extent of the lattice fringe regions we have observed (section III.B). Dark field images from the meridional reflections exhibit no prominent diffraction contrast, indicating the presence of some paracrystalline axial shift in the extrusion direction.

#### B. Lattice Imaging from PBT Fibers

PBT of inherent viscosity 31 was supplied by J. Wolfe of Stanford Research Institute. The fibers investigated were spun by E. Chenevey of Celanese Research from a 5.6% solution in polyphosphoric acid using a 5 x 200  $\mu\text{m}$  diameter

spinneret maintained at 60°C. A spin draw ratio of 3.7X was obtained by use of a 7.5 cm air gap followed by coagulation in an aqueous bath containing 9% H<sub>3</sub>PO<sub>4</sub> and final washing in pure water. The as spun filament had a modulus of 480 gpd and a strength of 18 gpd. After drying, the filaments were tension heat treated by a continuous process through an oven maintained at 475°C with a nitrogen atmosphere. Residence time was 64 seconds with a 4% applied stretch. A final modulus of 1900 gpd and strength of 21 gpd was obtained.

Thin sections of fiber were prepared by extraction replication as in section III.A. Regions of fiber suspended across holes in a perforated carbon support film were examined in axial bright field at 100 KeV in a JEOL 100CX electron microscope with spherical aberration coefficient of 6.7 mm. The microscope was carefully adjusted at 100,000X for approximately Scherzer defocus ( $\Delta f$ ) conditions by minimizing granularity (phase contrast) in the carbon support film ( $\Delta f \approx -170$  nm for our microscope). This value of focus results in good transfer of diffracted beams over the spatial frequency range from about 0.7 to 2 nm<sup>-1</sup>. Once focus was obtained in a given area, an adjacent unirradiated area was quickly chosen and the photographic exposure made without further adjustment using Kodak 4489 electron microscope film. Optical transforms of electron micrograph negatives were obtained on a Polaron optical diffractometer using Polaroid 55 P/N film.

The electron beam radiation damage lifetime of PBT is approximately 1.6 coul/cm<sup>2</sup> for equatorial reflections at 100 KeV and room temperature (section III.A). Since lattice images have been reported for Poly(p-phenylene terephthalamide) (radiation damage lifetime of 0.2 coul/cm<sup>2</sup>) [40], the prospect

of obtaining lattice images for sufficiently ordered PBT is quite good.

Figure 14 shows an electron diffraction pattern typical of the as spun and heat treated PBT fiber. The axial molecular orientation is very high. The pattern is characterized by discrete equatorial reflections and diffuse, continuous layer lines (up to 20 orders being visible on the negative). This type of pattern can arise due to an axially disordered crystal structure [41-43]. There is good lateral packing of chains into a two dimensional net but along the fiber axis the chains are irregularly positioned. The unit cell based on the (ten) equatorial reflections is monoclinic with  $a = .597 \text{ nm}$ ,  $b = .362 \text{ nm}$ ,  $\gamma = 95.2^\circ$  with fiber repeat of  $c = 1.24 \text{ nm}$  [44]. The cylindrically averaged Fourier transform of a single (completely planar conformation) chain has been calculated [44 and also section III.C] and shows good agreement with the observed diffraction pattern confirming the basic two dimensional order with high axial orientation.

The tension heat treatment of PBT fibers has resulted in further significant improvements in axial tensile modulus over as-spun and annealed fibers (section III.F). Electron diffraction patterns still show no distinct  $hkl$  reflections but modifications occur in the continuous distribution of intensity along the layer lines. This likely arises from a slight improvement in axial orientation and hence decreased azimuthal smearing of the layer line intensities.

In partially ordered systems high resolution electron microscopy has proved particularly valuable since while the electron diffraction pattern is a composite average from a region of the fiber, imaging details the structure locally and can reveal minority regions of different degree of order than the bulk

average [45].

An axial bright field image obtained using an  $8 \text{ nm}^{-1}$  cutoff objective aperture is shown in Figure 15. Distinct fringes (labelled E) are observed parallel to the fiber axis over regions 20 nm wide by 40 nm long with spacing of 0.59 nm corresponding to the first equatorial reflection ( $e_1$ ). Less distinct, somewhat meandering fringes are also observed approximately normal to the fiber axis (labelled M). These fringes have a spacing of 1.24 nm corresponding to the first layer line ( $m_1$ ). They occur in groups of 3-10 fringes with their lateral extent limited to about 5 nm. An optical transform of the bright field micrograph used to print Figure 15 is shown in Figure 16a (schematic Figure 16b). A pair of faint spots is seen normal to the fiber axis with a pair of streaks at  $90^\circ$ . The ratio of their reciprocal spacings is 2.13, corresponding well with the ratio  $m_1/e_1$  (i.e.  $1.24/.59 = 2.10$ ). The intensity distributions in the optical transform also correspond well with the expected shape transforms of the large (E) and small, elongated (M) fringe regions. The 1.24 nm lattice fringes are unequivocal evidence for the occurrence of true three dimensional crystalline order in local regions of the fiber. At present however, these type of regions are a very minor component of the fibers examined. The fringe regions thus far observed while limited in extent, show no evidence of structural defects. This is similar to the perfection of order in lattice images of PPTA fibers [40]. Ongoing work is concerned with detailed correlation of the extent and orientation of the lattice image regions with fiber mechanical properties.

#### C. Calculation of the Fourier Transform of a Single PBT Chain

In order to better understand the selected area electron diffraction (SAED)

and wide angle x-ray diffraction (WAXD) of PBT, we have decided to further consider the Fourier transform of a single PBT chain. In this case we use the method of Tadokoro [41,42]. We have specifically considered two sets of atomic coordinates, a set supplied by Odell et al. [46] and another set generated by summing bond vectors obtained from bond angles, bond distances, and internal rotation angles obtained from the Wellman et al. [47] model compound studies. The program BOND SUM, which was based on a procedure reported by Yokouchi et al. [48], and data are included in Appendix I.

First, we consider the case of cylindrical symmetry where the Fourier transform is rotationally averaged using a program CYLTRAN (Appendix II) and second, the case of preferred orientation (that is, without the cylindrical average) using a program POTRAN (Appendix III). The input files for CYLTRAN or POTRAN are generated using a program DATAGN (Appendix IV), thereby minimizing the risk of introducing erroneous coordinates by retyping data.

Specifically, calculations have been performed for the 1st - 8th layer lines using a c axis repeat of 12.45 Å. The scattered intensity along a particular layer line [i.e. at increments of  $\ell/c$  along the  $c^*$  axis (fiber axis)] was calculated at  $0.4 \text{ nm}^{-1}$  increments along an axis, labeled  $S_2$ , which is normal to  $c^*$ . Thus the magnitude of the scattering vector  $\xi$  in reciprocal space is defined by

$$|\xi|^2 = (\ell/c)^2 + n^2 |\xi_2|^2 \quad (4)$$

or, in the notation used later for small angle scattering (section III.G)

$$|\tilde{S}|^2 = \ell^2 |\tilde{S}_1|^2 + n^2 |\tilde{S}_2|^2 \quad (5)$$

This is shown in Figure 17.

Following Tadokoro [42] an orthotropic temperature factor has been used. Two cases have been considered, specifically 6.0 and 2.5 Å<sup>2</sup> normal to the chain direction and 6.0 and 0.5 Å<sup>2</sup> parallel to the chain direction. These values were suggested by E. Roche [49]. In the future these may be experimentally determined from intensity measurements as described by Buerger [50].

### 1. Cylindrically Averaged Fourier Transforms

Figure 18 shows the square of the cylindrically averaged Fourier transform for the first through eighth layer lines calculated assuming the coordinates of Odell *et al.* [46] where the molecular axis has been rotated to coincide with the fiber axis. A temperature factor of (0.5, 2.5 Å<sup>2</sup>) (parallel, normal) was used. The variations of intensity along the layer lines are in qualitative agreement with the matrix printer plots shown by Odell (see Figure 19).

When coordinates generated by BOND SUM were used with a temperature factor of (0.5, 2.5 Å<sup>2</sup>) (see Figure 20) a splitting of the sixth layer line is observed. Apparently the slight differences (typically  $\pm 0.02$  nm) in the atomic coordinates are sufficient to cause differences, particularly in the higher order layer lines which are more sensitive to the local atomic structure. When the temperature factor is increased to (6.0, 6.0 Å<sup>2</sup>) (see Figure 21) the intensity falls faster with increasing  $S_2$  on the higher layer lines, but the shapes of the curves are similar. The program was then used to calculate the distribution of intensity

about a given layer line in specified increments of  $S_1$ . Figure 22 shows the distribution in intensity about  $\ell = 6$  in increments of  $2 \times 10^{-2} \text{ nm}^{-1}$  along the meridian. The calculated maximum remains at constant  $S_2$  as one moves slightly off the layer line. Therefore splitting will not disappear simply by moving off of an integral layer line. It is also important to note that the cylindrical average is insensitive to rotation of the phenyl ring and so cannot be used as evidence to support a model with a particular conformational angle. The cylindrical average was also found insensitive with respect to including the weak scattering from the H atoms.

## 2. Chains with Preferred Orientation

In order to investigate the effect of preferential orientation we considered two angles:  $\phi$  - the angle of the phenyl ring with respect to the bisthiazole moiety and  $\alpha$ , the angle of the bisthiazole moiety with respect to the reciprocal space vector normal to the incident beam direction (taken to be normal to  $\zeta$ , see Figures 29 and 30).

Figure 23 shows the intensity for a single chain with  $\phi = 35^\circ$  of 8 repeat units as the setting angle,  $\alpha$ , is increased from  $0^\circ$  to  $90^\circ$ . Splittings of especially the 5th and 6th layer lines are observed which move to higher  $S_2$  values and decrease in intensity as  $\alpha$  increases. Figure 24 shows similar data for  $\phi = 0, 25, 35$  and  $45^\circ$  for  $\alpha = 0^\circ$ .

The calculated layer line intensity distributions are currently being compared to microdensitometer traces from electron diffraction patterns and x-ray precession photographs. Figure 25 shows preliminary results for the comparison

precession photographs. Figure 29 shows preliminary results for the comparison of the calculated intensity distribution for the sixth layer line to the distribution obtained by microdensitometry. Calc-1 is the cylindrically averaged calculation with the coordinates from Odell *et al.* [46], Calc-2 is the cylindrically averaged calculation using the coordinates from the Wellman *et al.* [47] model compound study. Notice the remarkable agreement including the secondary maximum near  $S_2 = 4 \text{ nm}^{-1}$  in the latter case. For correct comparison to the molecular transform, the diffracting material must have very high axial orientation to prevent smearing out of the intensity due to fibril misorientation.

#### D. Packing Analysis in the PBT Unit Cell

##### 1. Packing Analysis of PBT Chains

In order to augment our electron diffraction studies we have considered the potential energy of PBT chains packed in a monoclinic net. The potential energy of such an array can be modeled as the sum of the pairwise interactions of a PBT unit with three neighboring chains, each consisting of three units, plus the intrachain potential energy.

The interchain potential energy was calculated from the sum of the pairwise Van der Waals interactions using a Buckingham potential function with parameters supplied by Welsh, Bhaumik and Mark [51]. Following their suggestion "aromatic" Buckingham potential function parameters were used only for 1,3 pairs - that is for interactions roughly perpendicular to the benzene rings. This assumption is only valid for small conformational and setting angles (see below). The parameters used are given in Table . Thus, the potential energy of the PBT unit

with the  $i^{\text{th}}$  chain is given by:

$$V_{1-i} = \sum_{j=1}^N \sum_{k=1}^{3N} [A_{jk} \exp \{-b_{jk} d_{jk}\} - C_{jk} d_{jk}^{-6}] \quad (6)$$

and

$$E_{\text{TOT}} = \sum_{i=2}^4 V_{1-i} + E_{\text{INTRA}} \quad (7)$$

where  $E_{\text{TOT}}$  = total potential energy

$V_{1-i}$  = potential energy between the PBT segment and the  $i^{\text{th}}$  chain

$N$  = number of atoms in the segment (24)

$d_{jk}$  = distance between the  $j^{\text{th}}$  and  $k^{\text{th}}$  atom

$E_{\text{INTRA}}$  = intrachain potential energy

The basic configuration for the calculation is shown in Figure 26 which corresponds to the proposed PBT unit cell (Figure 27). The setting (or chain rotation) angle,  $\alpha$ , is defined as the angle between the projection of the benzobisthiazole moiety down the  $\zeta$  (chain) axis and the  $\alpha$  axis. The conformational angle,  $\phi$ , is defined as the angle between the phenyl ring and the benzobisthiazole moiety when both are projected down the  $\zeta$  axis. Thus, "aromatic" Buckingham parameters were only used for the 1,3 pair.

Intrachain energies in Equation 7 were obtained by interpolating values obtained by Welsh et al., [51] which were obtained by summing Van der Waals, torsional, and coulombic terms.

The chain at (0, A) was translated along the  $\zeta$  axis from -4.0 Å to 3.0 Å

The chain at (0, A) was translated along the  $\zeta$  axis from -0.4 nm to 0.3 nm in increments of 0.1 nm, with all other chains fixed with their origin at C=0. The setting angle  $\alpha$  was varied from  $-40^\circ$  to  $+50^\circ$  and chain conformational angle  $\phi$  was varied from  $-90^\circ$  to  $+90^\circ$ . Results revealed two broad minima in  $(\alpha, \phi)$  space. The first occurs at (-15, +40) and is the "global minimum" at T = 0.0 nm. The second occurs at (20, -5) and is a local minimum at T = 0.0 nm. To pass from one to another would require crossing about a 15 Kcal/mol barrier (see Figure 28). However, calculation of the structure factors for equatorial reflections for these conformations showed poor agreement with the experimental observed values, which suggests that our violation of the assumption of small  $\alpha$ ,  $\phi$  is significant. Thus the minima lie outside the range of validity of our assumption. However, the slow change of potential energy within the range of validity of our assumption supports the case for axial translational freedom of the molecule.

E. Light Microscopy of PBT Ribbons from PPA Dopes: Influence of Processing Conditions

Samples of PBT ribbons produced by Dr. E. Chenevey of Celanese Research Company have been examined by transmitted polarized light microscopy. See Section III.A for ribbon processing history. All ribbons in the series were observed to contain voids, the size and number of which increased with increasing extrusion temperature. Figure 29 shows a sample of film 29022-7-8 at two different orientations with respect to the polarizer. In Figure 29a, where the ribbon is oriented at  $45^\circ$  to the polarizer, the dark areas are voids

and are aligned in the extrusion direction. In Figure 29b, the ribbon is oriented at about 5° to the polarizer revealing that the voids are surrounded by misoriented regions. Complete extinction when the ribbon is oriented along the polarizer suggests that the average molecular orientation is high. Figure 30a shows ribbon 29022-7-5a oriented at 45° to the polarizer. Notice the increased size of the voids in this ribbon extruded at 90°C. In Figure 30b the same area is oriented at 0° to the polarizer, showing the increased misorientation around the voids.

Based on the limited number of samples we have received, the size and number of voids increases with increasing extrusion temperature. We hypothesize that their formation may be attributed either to water evolved from the PPA at higher temperatures or to coagulation inhomogeneities.

#### F. Small Angle Neutron Scattering

The objective of this work is to study the configuration of PBT molecules in dilute isotropic solution, concentrated nematic solutions and in the bulk, i.e. oriented and unoriented PBT films. The difference in neutron scattering cross section of hydrogen and deuterium provides scattering contrast when a mixture of deuterium labeled PBT in a solvent or in a hydrogenated PBT matrix is used.

In small angle scattering, the problem may be formulated as scattering from monomer units. Following the development of Cotton *et al.* [52], the total coherent, elastic scattering length,  $B$ , for a monomer containing  $n$  atoms may be written as:

$$B = \sum_{i=1}^n b_i \quad (8)$$

where  $b_i$  is the coherent, elastic scattering length for the  $i^{\text{th}}$  atom. The coherent, elastic scattering cross-section is  $4\pi B^2$ . The incoherent, elastic scattering cross-section for the monomer is obtained by summing the incoherent scattering cross-sections for the individual atoms:

$$\sigma_{\text{inc}}^{\text{TOT}} = \sum_{i=1}^n \sigma_i^{\text{EL}} - 4\pi b_i^2 \quad (9)$$

where  $\sigma_i^{\text{EL}}$  is the total elastic scattering cross-section for the  $i^{\text{th}}$  atom. Values of  $\sigma_i^{\text{EL}}$  and  $b_i$  have been tabulated by Bacon [53] and Cotton et al. [52]. These are summarized for atoms of interest in Table 5.

TABLE 5  
Scattering Parameters of Atoms Useful for PBT SANS

Atom	$b_i$ ( $10^{-12}\text{cm}$ )	$\sigma_i^{\text{el,coh}}$ ( $10^{-24}\text{cm}^2$ )	$\sigma_i^{\text{EL}}$ ( $10^{-24}\text{cm}^2$ )	$\sigma_i^{\text{el,inc}}$ ( $10^{-24}\text{cm}^2$ )
C	0.661	5.49	5.51	0.02
N	0.949	11.10	11.4	0.3
S	0.31	1.2	1.2	0.0
D <sup>+</sup>	0.65	5.4	7.6	2.2
D <sup>++</sup>	0.667	5.59	(12.8)	7.2
H	-0.378	1.8	81.5	79.7
O	0.577	4.2	4.24	0.04
P	0.53	3.53	3.6	0.07

<sup>†</sup>Bacon [53]      <sup>‡</sup>Cotton et al. [52]

Bacon's [53] value for the incoherent scattering cross-section for deuterium differs substantially from that used by Cotton et al. [52]. Other

literature surveyed revealed that about half of the authors used each value.

The original sources appear to be about the same age (1962-1965) and it is not clear which value is correct. For this reason, calculations were done using each value. More recently (1972, 1977), Bacon [54,55] confirmed the coherent scattering length of deuterium of  $0.667 \times 10^{-12} \text{ cm}$ , but still reports the incoherent cross-section as  $2.0 \times 10^{-24} \text{ cm}^2$ .

The appropriate scattering parameters were calculated for selected molecules of interest and are displayed in Table 6. Molar volumes were calculated for PBT chains based on the structural model of Roche *et al.* [56] using a density of 1.69. Polyphosphoric acid (PPA) was assumed to be  $(\text{PO}_3)_n$  with n sufficiently large to make end group contributions negligible. PPA was also assumed to have a density equal to that of  $\text{H}_3\text{PO}_4$ .

TABLE 6  
Parameters for Contrast Factor and Signal to Noise  
Calculations for SANS

Species	B ( $10^{-12} \text{ cm}$ )	Source	$\sigma_{\text{inc}}^{\text{TOT}}$ ( $10^{-24} \text{ cm}^2$ )	Molar Volume ( $\text{cm}^3/\text{mole}$ )	Density ( $\text{g}/\text{cm}^3$ )	Monomer M. Wt. (gmole)
$\text{D}_4\text{H}_2\text{PBT}$	13.60	Bacon	169.0	152.68	1.69	270.3
$\text{D}_4\text{H}_2\text{PBT}$	13.67	Cotton	188.0	152.68	1.69	270.3
$\text{D}_6\text{PBT}$	15.65	Bacon	13.0	152.68	1.69	272.3
$\text{D}_6\text{PBT}$	15.76	Cotton	44.0	152.68	1.69	272.3
$\text{H}_6\text{PBT}$	9.49	Bacon	478.0	152.68	1.69	266.3
MSA	4.21	Bacon	319.0	64.89	1.481	96.1
PPA	1.88	Bacon	79.7	43.6	1.834	80.0
$\text{D}_4\text{MSA}$	5.30	Bacon	8.0	67.56	1.481	100.1
$\text{D}_4\text{MSA}$	5.37	Cotton	32.0	67.56	1.481	100.1
$\text{D}_1\text{PPA}$	2.91	Bacon	5.2	44.15	1.834	81.0
$\text{D}_1\text{PPA}$	2.93	Cotton	7.4	44.15	1.834	81.0

### 1. SANS of Dilute Mixtures

The scattered intensity was calculated for a dilute mixture of a polymer of molecular weight  $M$  (monomer molecular weight  $m_1$ ) in a matrix of species 2 of molecular weight  $m_2$ . If species 2 is a polymer, we assume that the polymer molecular weight is the same as species 1, and  $m_2$  is the monomer molecular weight. For a dilute mixture, the intensity of elastically-scattered neutrons,  $I$ , as a function of the scattering vector  $q = \frac{4\pi}{\lambda} \sin \frac{\theta}{2}$  is given by equation (10):

$$I(q) = N_A V \Phi_0 t T [K^2 \frac{c_1}{m_1} \frac{M}{m_1} S_0(q) + \frac{c_1}{m_1} B_{I_1}^2 + \frac{c_2}{m_2} B_{I_1}^2] + \int_0^t N(q,t) dt \quad (10)$$

$N_A$  = Avagadro's Number

$V$  = scattering volume ( $\text{cm}^3$ )

$\Phi_0$  = incident neutron flux ( $\text{cm}^{-2}\text{sec}^{-1}$ )

$t$  = counting time (sec)

$c_1$  and  $c_2$  = concentration ( $\text{g}/\text{cm}^3$ ) of species 1 and 2

$K^2$  = square of the contrast factor (given by equation (11))

$S_0(q)$  = scattering function

$T$  = specimen transmittance (given by equation (12))

$N(q,t)$  = electronic noise from the detector - e.g. the dark current

The first term of equation (10) is the coherent scattering, the second and third terms are due to incoherent scattering of the polymer and solvent and the fourth term is due to system noise.

The square of the contrast factor is defined as

$$K^2 = [B_1 - \left(\frac{V_1}{V_2}\right) B_2]^2 \quad (11)$$

where  $V_1$  and  $V_2$  are the molar volumes of species 1 and 2. The transmittance,  $T$ , is given by

$$T \equiv \frac{I}{I_0} = \exp \{-n\sigma_{EL}x\} \quad (12)$$

where  $n$  is the number of scatterers per unit volume,  $\sigma_{EL}$  is the total elastic scattering cross-section for neutrons, and  $x$  is the sample thickness. The optimum sample thickness occurs for a value of the transmittance of  $\frac{1}{e}$ , i.e.  $x = \frac{1}{n\sigma_{EL}}$  (see Table 7).

TABLE 7  
Optimum Matrix Thickness for SANS of PBT

Species	X <sub>optimum</sub> (cm)
D <sub>4</sub> H <sub>2</sub> PBT	.10
D <sub>6</sub> PBT	.08
H <sub>6</sub> PBT	.16
MSA	.20
PPA	.58
D <sub>1</sub> PPA	.66
D <sub>4</sub> MSA	.31
<hr/>	
H <sub>8</sub> Polystyrene <sup>+</sup>	.27
D <sub>8</sub> Polystyrene <sup>+</sup>	.14

<sup>+</sup>Values of Polystyrene are given for comparison

SANS samples much larger than the thickness of normal PBT ribbons are therefore necessary. Processing single films 1 mm thick is impractical, so one must stack multiple films and optimize signal/noise by the proper choice of label species and matrix.

The scattering function  $S_0(q)$  is given by

$$S_0(q) = \frac{1}{n_1^2} \sum_i^{n_1} \sum_j^{n_1} e^{iq \cdot r_{ij}} \quad (13)$$

where the double sum is over all monomer units in a single polymer molecule.  $S_0(q)$  as defined is normalized to unity for  $q = 0$  and falls off with scattering angle depending on the molecular configuration. For randomly oriented rods of length  $2L$  [36]:

$$S_0(q) = \frac{Si(qL)}{qL} + \frac{\sin^2(qL)}{(qL)^2}$$

$$\text{where } Si(qL) = \int_0^{qL} \frac{\sin u}{u} du$$

A plot of  $S_0(q)$  for an anisotropic solution of rods is shown in Figure 31. The larger the rod length the faster the decrease of  $S_0(q)$  with scattering angle. Guinier [36] has shown that for  $R_g q \ll 1$

$$S_0(q) \approx 1 - \frac{R_g^2 q^2}{3} \quad (14)$$

where  $R_g$  is the radius of gyration and is for a rod of length  $2L$ :

$$R^2 = \frac{4L^2}{12} \quad (15)$$

Using the approximation  $e^{-x} \approx 1-x$ , equation (7) becomes

$$S_0(q) = e^{-Rg^2q^2/3} \quad (16)$$

and thus a plot of  $\log S_0(q)$  versus  $q^2$  yields the radius of gyration and hence the rod length.

If one neglects the dark current of the detector, the signal/noise ratio may be calculated as the ratio of coherent to incoherent scattering. This is given by equation (17) below:

$$\frac{S}{N} = \frac{k^2 DP}{B_{I1}^2 + \frac{c_2 m_1}{c_1 m_2} B_{I2}^2} S_0(q) \quad (17)$$

where DP is the degree of polymerization and the  $B_{Ii}$  are the incoherent scattering cross-sections. Calculated values of  $K^2$  and  $S/N$  for various polymers and matrixes are given in Table 6. Representative combinations are given in Table 8.

For a mixture of species 1 (weight fraction,  $w_1$ ) in a matrix of species 2 (weight fraction,  $w_2$ ), the concentration in g/cm<sup>3</sup> of solution is given by:

$$c_1 = w_1^2 (\rho_1 - \rho_2) + w_1 \rho_2 \quad (18)$$

analogously for  $c_2$

$$c_2 = w_2^2 (\rho_2 - \rho_1) + w_2 \rho_1 \quad (19)$$

where  $\rho_1$  and  $\rho_2$  are the densities of the pure components 1 and 2. The degree of polymerization of species 1 (typically for PBT: 20, 50 and 100) and weight fractions (typically 0.01 and .05) were used to calculate the signal to noise ratio.

TABLE 8

Contrast Factor and Signal to Noise Ratio for Selected Pairs of Species 1 (LABEL) in Species 2 (MATRIX) for Small Angle Neutron Scattering Assuming  $W_1 = 0.01$  and  $DP_1 = 50$

Species 1	D <sub>4</sub> H <sub>2</sub> PBT			H <sub>6</sub> PBT			D <sub>6</sub> PBT		
	K <sup>2</sup>	S/N <sup>+</sup>	S/N <sup>++</sup>	K <sup>2</sup>	S/N <sup>+</sup>	S/N <sup>++</sup>	K <sup>2</sup>	S/N <sup>+</sup>	S/N <sup>++</sup>
Species 2									
D <sub>4</sub> H <sub>2</sub> PBT				17.47	0.65	0.58	4.37	0.16	0.15
H <sub>6</sub> PBT	17.47	0.23	0.23				39.31	0.51	0.51
D <sub>6</sub> PBT	4.37	1.90	0.61	39.31	14.22	5.21			
MSA	14.17	0.10	0.10	0.17	0.00	0.00	34.27	0.24	0.24
PPA	50.22	1.18	1.18	8.45	0.20	0.20	84.21	1.97	1.97
D <sub>4</sub> MSA	2.35	0.64	0.17	7.00	1.70	0.49	13.14	3.81	0.95
D <sub>1</sub> PPA	12.51	4.17	2.99	0.41	0.12	0.09	31.67	11.41	7.94

<sup>+</sup> S/N times  $S_0(q)$ , data from Bacon [42]

<sup>++</sup>S/N times  $S_0(q)$ , data from Cotton [38]

Since  $0.1 \leq 1$ , a S/N<sup>+</sup> ratio of at least 10 is desired. The best candidates are thus seen to be D<sub>6</sub>PBT and H<sub>6</sub>PBT (bulk), D<sub>6</sub>PBT and D<sub>1</sub>PPA, and D<sub>4</sub>H<sub>2</sub>PBT and D<sub>1</sub>PPA (solution).

Equation (17) shows the signal to noise ratio is directly proportional to the degree of polymerization. Therefore DP should be as high as possible, e.g. a DP of 500 would increase all S/N ratios in Table 7 by a factor of 10.

## 2. Preliminary Results

SANS experiments have been performed at Oak Ridge National Laboratory on isotropic solutions of 1 wt% D<sub>4</sub>H<sub>2</sub> PBT in MSA, nematic 10% polymer (10% D<sub>4</sub>H<sub>2</sub>PBT + 90% H<sub>6</sub>PBT) in MSA, and bulk 50% D<sub>4</sub>H<sub>2</sub>PBT/50% H<sub>6</sub>PBT extruded ribbons and relaxed, precipitated films. The experimental signal to noise ratio for the isotropic and nematic colutions was too low for meaningful analysis and in addition

problems were encountered with the beam monochromator.

The bulk precipitated films showed an unexpectedly strong scattered intensity. This scattering is likely due to voids caused by the coagulation (precipitation) process.

Future SANS experiments on PBT must be carefully designed. If synthetically feasible, a substantial increase in S/N would be obtained using D<sub>6</sub>PBT and higher molecular weight PBT. However, because PBT is a rod-like molecule, Rg increases linearly with MW, so that a degree of polymerization of 120 (corresponding to a Rg of 1500 Å) is about the largest size rod-like molecule which the present 30-m SANS apparatus can measure. For bulk studies, void content must be minimal, indicating the need for slower coagulation of the polymer from the solvent. Finally, instead of using a dilute label, recent work [50,60] has shown that the single chain form factor of the polymer in bulk can be obtained from a single concentration measurement for any concentration of labelled molecules, providing the molecular weights of the matrix and labelled molecules are the same and the molecular weight distributions are narrow. Thus 50/50 blends could be used to improve S/N.

#### G. Microvoid Analysis by Small Angle X-ray Scattering

Wet spun fibers have long been known to exhibit a diffuse, continuous distribution of intensity of x-rays scattered at small angles [61]. This diffuse scattering has been attributed to the presence of microvoids which are small regions, generally 10 nm or less in size, that have lower electron density than the surroundings. Statton [62] envisioned microvoids as "the unfilled spaces around polymer segments, around segment bundles (fibrils), and between

lamellae, if such exist." The degree of crystallinity, when measured by wide angle x-ray scattering and differential scanning calorimetry, is unrelated to the diffuse scattered intensity [62]. Cellulose acetate which is known to be noncrystalline exhibits a high intensity of diffuse scatter [61]. The scattering from rayon was also found to decrease in intensity when the fibers were swollen with water, thereby decreasing the difference in electron density between the void and the polymer matrix [61]. Thus, this diffuse SAXS intensity is not caused by crystalline regions of high electron density embedded in a noncrystalline polymer matrix as many early investigators postulated [61]. Heikens, Hermans and Weidinger [63] found the diffuse scattered intensity increased with decreasing density and therefore, increasing void fraction, in air swollen cellulose. Comparison of the volume fraction of voids calculated from the SAXS integrated intensity with that calculated from density measurements indicated that only 20% of the total void volume consisted of sufficiently small voids to affect their accessible small angle scattering region.

Dobb et al. [64] have studied microvoids in Kevlar 29® and Kevlar 49® fibers by SAXS and electron microscopy. To visualize the microvoids by TEM and to increase the SAXS intensity, these authors stained the polymer with silver sulfide. The apparent microvoid size measured by SAXS in stained fibers was always smaller than the size measured in unstained fibers. They postulated that this occurred either by structural changes upon staining or a proportion of the voids were inaccessible to the stain. The former case is plausible since the staining procedure involved impregnation of the fibers with H<sub>2</sub>S at a pressure of 2 MPa followed by impregnation with aqueous AgNO<sub>3</sub>. The high pressure of

impregnation could cause a collapse of some void space. The latter case implies that the surface of the fiber which solidified first during coagulation contained voids smaller than the voids in the center of the fiber which solidified later and tended to cavitate. Thus, diffusion controlled staining would selectively stain the smaller voids. One may distinguish between these two cases by varying the time of staining.

In the following sections we will examine how to measure microvoid size and the assumptions inherent in the measurement. The results of SAXS experiments on selected PBT and Kevlar® samples will then be presented. The data will be analyzed by several models to determine which model(s) best represent this scattering system. We will then discuss how changes in processing history affect the average microvoid size.

### 1. The Intensity of Small Angle Scattering

The objective of this section is to relate the intensity of diffuse small angle x-ray scattering (SAXS) to the size and number of the fluctuations in electron density (voids in this case) which produce the scattering. One may approach this problem by two basic routes. The first option is to assume particulate scattering and, following Guinier and Fournet [57], to derive an equation for the scattered intensity in terms of the average squared radius of gyration of the particle,  $\langle R_g^2 \rangle$ . The second option uses a statistical approach patterned after Debye and Bueche [65]. We will consider each option and seek to determine which is most useful for analysis of the SAXS from PBT.

Let us consider an x-ray beam  $\xi_0$  incident upon a sample which generates a

scattered x-ray beam  $\tilde{s}'$  that subtends an angle  $2\theta$  with  $\tilde{s}_0$ . The scattered intensity is expressed in terms of the difference between  $\tilde{s}'$  and  $\tilde{s}_0$  (see Figure 33).

$$\tilde{s} = \tilde{s}_0 - \tilde{s}' \quad (20)$$

$$|\tilde{s}| = \frac{2 \sin \theta}{\lambda} . \quad (21)$$

Here  $\lambda$  is the wavelength of x-rays (0.154 nm for CuK $\alpha$ ). If one assumes that the specimen consists of a dilute system of  $N$  particulate scatterers each of which may be subdivided into  $M$  scattering elements which have scattering amplitudes  $f(\tilde{s})$ , the scattered intensity,  $I(\tilde{s})$ , is given by [66]

$$I(\tilde{s}) = N I_e \sum_{i=1}^M \sum_{j=1}^M f_i(\tilde{s}) f_j(\tilde{s}) \cos(2\pi \tilde{s} \cdot \tilde{r}_{ij}) \quad (22)$$

where  $I_e$  is the scattered intensity from a single electron

$$I_e = P_0 \left( \frac{e^2}{mc^2} \right) \frac{1}{a^2} = 7.96 \times 10^{-26} \text{ cm}^2 P_0/a^2 \quad (23)$$

and

$P_0 \equiv$  primary beam intensity (counts/sec $^{-1}$ )

$a \equiv$  sample to detector distance (cm)

$\tilde{r}_{ij} \equiv$  vector between scattering elements  $i$  and  $j$  (nm)

when  $\tilde{s}$  has units nm $^{-1}$ .

Alternately, one may assume that for SAXS the system may be considered as

continuous distribution of electron density,  $\rho(\underline{r})$ , which may be expressed in terms of fluctuations,  $n(\underline{r})$ , from an average value,  $\bar{\rho}$

$$\rho(\underline{r}) = \bar{\rho} + n(\underline{r}). \quad (24)$$

(see the insert in Figure 33). These fluctuations in electron density are described by the correlation function,  $\gamma(\underline{r})$  which is defined as

$$\gamma(\underline{r}) \equiv \frac{\int n(\underline{r}') n(\underline{r}' + \underline{r}) dV_{\underline{r}'}}{\int n(\underline{r}') n(\underline{r}') dV_{\underline{r}'}} \quad (25)$$

or

$$\gamma(\underline{r}) = \frac{\int n(\underline{r}') n(\underline{r}' + \underline{r}) dV_{\underline{r}'}}{\langle n^2 \rangle V_X} \quad (26)$$

where  $\langle n^2 \rangle$  is the mean squared electron density fluctuation ((moles electrons)<sup>2</sup> cm<sup>-3</sup>) and  $V_X$  is the volume of the sample irradiated by the x-ray beam [66]. By definition  $\gamma(\underline{r})$  (equation 25) is normalized to unity at  $\underline{r} = 0$ . For a two phase system such as that depicted in the inset in Figure 33,  $\gamma(\underline{r})$  represents the probability that a small volume element probe separated by the vector  $\underline{r}$  from a reference volume element in phase 1, is also in phase 1. In such a two phase system with randomly positioned voids,  $\gamma(\underline{r})$  reaches an asymptotic value of zero as  $|\underline{r}|$  reaches infinity.

For this model,  $I(\underline{s})$  is given by the three-dimensional Fourier transform of  $\gamma(\underline{r})$  [66]

$$I(\tilde{s}) = I_e v_x \langle n^2 \rangle \int \int \int \gamma(r) \exp \{ -2\pi i \frac{\tilde{s} \cdot r}{\tilde{s}} \} dv_r. \quad (27)$$

## 2. Isotropic Systems

### a. Guinier's Law

After averaging over all orientations of the particle, equation 22 becomes

$$I(|\tilde{s}|) = \sum_{i=1}^M \sum_{j=1}^N f_i(|\tilde{s}|) \frac{\sin 2\pi |\tilde{s}| |\tilde{r}_{ij}|}{2\pi |\tilde{s}| |\tilde{r}_{ij}|} \quad (28)$$

Guinier [58] expanded the sine in equation 28 as a power series and found  $I(\tilde{s})$  for a monodisperse system of spheres to be given by

$$I(|\tilde{s}|) = (\sum f_i(|\tilde{s}|))^2 \left\{ 1 - \frac{4\pi^2 |\tilde{s}|^2}{3} R_g^2 + \dots \right\} \quad (29)$$

which, for  $2\pi |\tilde{s}| R_g < 1$ , may be written as

$$I(|\tilde{s}|) = I(0) \exp \{ -4\pi^2 |\tilde{s}|^2 R_g^2 / s \} \quad (30)$$

when this model is valid, a plot of  $\ln I(|\tilde{s}|)$  versus  $4\pi^2 |\tilde{s}|^2$  yields a straight line with a slope equal to  $-R_g^2/3$ .

### b. Debye-Bueche Theory

For an isotropic system  $\gamma(r)$  is only a function of the magnitude of  $r$  so that equation 27 becomes:

$$I(s) = I_e V_x \langle n^2 \rangle \int_{\phi_2=0}^{\pi} \int_{\psi_2=0}^{2\pi} \int_{r=0}^{\infty} r^2 \gamma(r) dr \exp \{-2\pi i s r \cos \psi_2\} \times \sin \psi_2 d\psi_2 d\phi_2 \quad (31)$$

where  $\psi_2$  and  $\phi_2$  are the two angles in spherical coordinates (see Figure 33). We have assumed the isotropic sample to be positioned in the x-ray beam such that  $s \cdot r = sr \cos \psi_2$ . Performing the integration over  $\phi_2$  and  $\psi_2$  yields

$$I(s) = 4\pi I_e V_x \langle n^2 \rangle \int_{r=0}^{\infty} \gamma(r) r^2 \frac{\sin(2\pi s r)}{2\pi s r} dr \quad (32)$$

Debye and Bueche [65] have shown that for many systems  $\gamma(r)$  may be approximated as  $\exp \{-r/\lambda_a\}$  where  $\lambda_a$  is termed the correlation length and is a measure of the size of voids. For a random 2 phase system of voids in a continuum, the exponential correlation function is rigorous. Physically, this indicates that the probability that two volume elements separated by a distance  $r$  are both in the same phase decreases exponentially with increasing values of  $r$ . Substituting this exponential correlation function into equation 26 and integrating leads to

$$I(s) = \frac{8\pi I_e V_x \lambda_a^3}{(1 + 4\pi^2 s^2 \lambda_a^2)^2} \quad (33)$$

Equation 28 may be rearranged to yield

$$I(s) = \frac{1 + 4\pi^2 s^2 \lambda_a^2}{[8\pi I_e V_x \lambda_a^3]^{1/2}} \quad (34)$$

Thus, for an exponential correlation function, a plot of  $[I(s)]^{-1/2}$  vs  $4\pi^2 s^2$  is linear and  $\lambda_a^2$  is given by the ratio of the slope to y-intercept of the plot.

### 3. Extension to Anisotropic Systems

Four approaches to apply equation 22 to a system with uniaxial symmetry symmetry will be discussed in detail below. We will postulate that the microvoids in PBT fibers and films are axially symmetric with respect to rotation about the extrusion direction. A schematic of the model is shown in Figure 33. Thus, following Crist [74],  $s$  may be decomposed into components such that  $s_1$  is the component along the extrusion direction and  $s_2$  is the component normal to the extrusion direction lying in the detector plane. This is shown schematically in Figure 33. The vector  $s$  may also be described in terms of its magnitude and the angle  $\mu$  with respect to the  $s_1$  axis in Figure 33.

In the following treatment we postulate that the microvoids are all perfectly oriented along the extrusion direction and that the scattered intensity is only determined by the shape, size and spatial arrangement of microvoids and not variation of their orientation. We also assume that, in addition to each microvoid being perfectly oriented along the extrusion direction, the microvoids are randomly positioned in a continuum of PBT.

#### a. The Projected Correlation Function

Considering equation 22 one finds that for any principal direction,  $s_i$

$$I(s_i, 0, 0) = I_e V_x \langle n^2 \rangle \iiint \gamma(r) \exp \{ -2\pi i (s_i, 0, 0) \cdot r \} dv_r \quad (35)$$

For example, the intensity along  $s_1$  may then be written as

$$I(s_1, 0, 0) = I_{eV_X} \langle n^2 \rangle \int [\int \int \gamma(r_1, r_2, r_3) dr_2 dr_3] e^{-2\pi i s_1 r_1} dr_1 \quad (36)$$

which may be written more compactly as

$$I(s_1, 0, 0) = I_{eV_X} \langle n^2 \rangle \int \gamma_{pp}(r_1) e^{-2\pi i s_1 r_1} dr_1 \quad (37)$$

where  $\gamma_{pp}(r_1)$  is the projection of the correlation function onto the  $r_1$  axis.

By Fourier inversion one finds

$$\gamma_{pp}(r_1) = \frac{1}{I_{eV_X} \langle n^2 \rangle} \int_{-\infty}^{\infty} I(s_1, 0, 0) e^{2\pi i s_1 r_1} ds_1 \quad (38)$$

or

$$\gamma_{pp}(r_1) = \frac{1}{I_{eV_X} \langle n^2 \rangle} \mathcal{F}^{-1}[I(s_1, 0, 0)] \quad (39)$$

where  $\mathcal{F}^{-1}$  denotes the inverse Fourier transformation. Thus, by using the Fast Fourier Transform algorithm [69] to perform a discrete inverse Fourier transformation on the measured  $I(s)$ , one directly obtains the projection of the correlation function onto a given axis. This technique is the most general since it requires no assumptions about the form of the correlation function. However, because of the nature of the discrete transform algorithm, the data is forced to be periodic by flipping it about the last point [69]. One also must be careful to sample data over the correct interval [69]. Still, truncation of intensity data at high and low values of  $s$  causes error in the corelation function low and high values of  $r$ .

b. Extension to Uniaxial Systems Using Spherical Coordinates

Summerfield and Mildner [68] have modeled scattering from systems with scattering patterns that possess centrosymmetric azimuthal symmetry. These authors have chosen to approach the problem using spherical coordinates and find that the scattered intensity at the limit of small angles is given by [68]:

$$I(\|\tilde{s}\|) = K [1 + 4\pi^2 \|\tilde{s}\|^2 (\ell_a^2 \cos^2 \mu + \ell_c^2 \sin^2 \mu)]^{-2} \quad (40)$$

where  $\mu$  is the polar angle with respect to the axis of azimuthal symmetry of the pattern (see Figure 33). They have defined  $\ell_a^2$  and  $\ell_c^2$  as

$$\ell_a^2 = \pi N \int_0^\infty r^4 dr \int_{-1}^1 d(\cos\phi_1) g(r, \phi_1) \cos^2 \phi_1 \quad (41)$$

$$\ell_c^2 = \frac{\pi N}{2} \int_0^\infty r^4 dr \int_{-1}^1 d(\cos\phi_1) g(r, \phi_1) \sin^2 \phi_1 \quad (42)$$

where  $r$  and  $\phi_1$  are the polar coordinates of the scattering center and  $N$  is the number of scatterers (see Figure 33). The static pair correlation function,  $g(\tilde{r})$ , is defined by [68]

$$g(\tilde{r}) = \left\langle \sum_i \sum_{j \neq i} \delta(\tilde{r} - \tilde{r}_i + \tilde{r}_j) \right\rangle \cdot \frac{1}{N} \quad (43)$$

where  $\tilde{r}_i$  and  $\tilde{r}_j$  are the radius vectors to the  $i^{th}$  and  $j^{th}$  scattering elements and  $N$  is the number of scatterers. For a two phase system of microvoids in a continuum of PBT,  $\gamma(\tilde{r})$  is related to  $g(\tilde{r})$  by equation 44 [76]

$$\langle n^2 \rangle \gamma(r) = \langle \rho \rangle \{ \delta(r) + \langle \rho \rangle [g(r) - 1] \} . \quad (44)$$

Thus  $\ell_a^2$  and  $\ell_c^2$  are projected correlation lengths and are a measure of the size of the inhomogeneities.

Summerfield and Mildner [68] have also related these parameters to the generalized Guinier approximation and therefore the radius of gyration of the inhomogeneities in the plane of the scattering vector. When the scattering plane includes the axis of symmetry, ( $s \parallel z$ ) then

$$\langle R_g^2 \rangle_{\parallel} = 2 (\ell_a^2 \cos^2 \mu + \ell_c^2 \sin^2 \mu) . \quad (45)$$

### c. Guinier Analysis of Anisotropic Systems

The third approach to this problem is due to Stein [70] and requires only the assumption that the correlation function is separable into components along the x, y and z direction (see Figure 33). Thus

$$\gamma(r) = \gamma(x) \gamma(y) \gamma(z) . \quad (46)$$

Assuming  $s_0$  is along the x direction of the sample and  $s'$  is at an angle  $2\theta$  to  $s_0$  and makes an angle  $\mu$  with the z axis (see Figure 33) one can calculate  $I(|s|)$ . The result was that at small angles

$$I(|s|) \approx K \exp \{ -4\pi^2 |s|^2 (R_y^2 \sin^2 \mu + R_z^2 \cos^2 \mu) \} \quad (47)$$

and so a Guinier plot of  $\ln I$  vs  $4\pi^2 |s|^2$  at  $\mu = 0^\circ$  will have a limiting slope

equal to  $\langle R_z^2 \rangle$  and at  $\mu = 90^\circ$  will have a limiting slope equal to  $\langle R_g^2 \rangle$ . Equation 47 reduces to the proper limit for isotropic samples since  $R_x^2 = R_y^2 = R_z^2 = \langle R_g^2 \rangle / 3$

$$I_{iso}(\left| \frac{s}{\lambda} \right|) = K \exp \{ - 4\pi^2 \left| \frac{s}{\lambda} \right|^2 \langle R_g^2 \rangle / 3 \}. \quad (48)$$

Thus, when analyzing Guinier plots on anisotropic data it is important not to divide the slope by 3 as one would do for an isotropic sample. It is important to note that, as for all Guinier plots, we are interested in the limiting slope at zero angle. This can be contrasted with the analysis of Jellinek et al. [71] who have attempted to resolve curved Guinier plots into components. This is equivalent to fitting the scattering curve with a number of Gaussians and often violates the small angle assumption ( $2\pi s R_g < 1$ ) used in deriving Guinier's Law. The results of such analysis are not unique and moreover, without further information about the nature of the system one cannot differentiate between polydispersity of size or nonspherical shape of the scattering particles.

The treatment due to Stein [70] may be compared to the results for a single ellipsoid of rotation with axes  $a, a, v$  oriented along  $s_1$  reported by Hosemann and Bagchi [72]

$$I_{el}(\frac{s}{\lambda}) \sim \exp \{ - \frac{4}{5} \pi^2 a^2 (v^2 s_1^2 + s_2^2 + s_3^2) \}. \quad (49)$$

This suggests that the projected  $\langle R_g^2 \rangle$  measured from a Guinier plot on anisotropic data is  $1/5$  of the average square of the radius of such an ellipsoid along the axis of projection. This is the model used by Dobb et al. [64] to interpret data from Kevlar 29 $^\circ$  and Kevlar 49 $^\circ$ . They reported an average ellipse diameter

perpendicular to the extrusion direction of 10 nm in an unstained sample of Kevlar 49®.

d. Extension to Uniaxial Systems Using Cylindrical Coordinates

The treatment described below was developed during the analysis of SAXS data for this dissertation. To follow Debye and Bueche [65], one must assume a form of correlation function to describe a uniaxial system. Two are considered here. First, one may follow the treatment of Stein and Hotta [67] for light scattering from oriented films and assume a uniaxial Gaussian correlation function

$$\gamma_1(\tilde{r}) = \exp \left\{ - \left( \frac{x^2}{\lambda_a^2} + \frac{y^2}{\lambda_a^2} + \frac{z^2}{\lambda_c^2} \right) \right\} = \exp \left\{ - \left( \frac{r_1^2}{\lambda_a^2} + \frac{z^2}{\lambda_c^2} \right) \right\} \quad (50)$$

where the z axis has been chosen to be unique (see Figure 33). This is equivalent to saying that the probability that two volume elements are both in a void decreases exponentially with the square of the distance between them, and that this rate of decrease is different along z and perpendicular to z.

Alternately, one may generalize the Debye exponential correlation function to cylindrical coordinates

$$\gamma_2(\tilde{r}) = \exp \left\{ - \left( \frac{|r|}{\lambda_a} + \frac{|z|}{\lambda_c} \right) \right\}. \quad (51)$$

This is equivalent to postulating that the probability that two volume elements are both in a void decreases exponentially with the distance.

If one assumes a uniaxial Gaussian correlation function equation 27 reduces to

$$I(s_1, s_2) = 2\pi V_X I_e \langle \eta^2 \rangle \int_{r=0}^{\infty} \int_{z=\infty}^{\infty} \exp \left\{ - \left( \frac{r^2}{\lambda_a^2} + \frac{z^2}{\lambda_b^2} \right) \right\} J_0(2\pi s_2 r) \\ \times \exp \left\{ - 2\pi i z s_1 \right\} r dr dz . \quad (52)$$

For the intensity along  $s_1$  this becomes

$$I(s_1, 0) = 2\pi I_e V_X \langle \eta^2 \rangle \int_{r=0}^{\infty} \exp \left( - \frac{r^2}{\lambda_a^2} \right) r dr \int_{z=-\infty}^{\infty} \exp \left( - \frac{z^2}{\lambda_c^2} \right) \\ \times \exp \left\{ - 2\pi i z s_1 \right\} dz . \quad (53)$$

After integration one obtains

$$I(s_1, 0) = \pi^{3/2} I_e V_X \langle \eta^2 \rangle \lambda_c \exp \left\{ - \pi^2 \lambda_c^2 s_1^2 \right\} \quad (54)$$

If a uniaxial Gaussian correlation function adequately describes the system, a Guinier type plot of  $\ln I(s_1, 0)$  vs  $s_1^2$  will be linear with a slope equal to  $-\pi^2 \lambda_c^2$ . Similarly for the intensity along  $s_2$  one obtains by Hankel Transformation

$$I(0, s_2) = 2\pi^{3/2} I_e \langle \eta^2 \rangle V_X \lambda_a^2 \exp \left\{ - \lambda_a^2 s_2^2 \right\} \quad (55)$$

Thus, a plot of  $\ln I(0, s_2)$  vs  $s_2^2$  will be linear with a slope equal to  $-\lambda_a^2$ .

For the case of the cylindrical exponential function, equation 27 becomes

$$I(s_1, s_2) = 2\pi I_e V_X \langle \eta^2 \rangle \int_{r=0}^{\infty} \exp \left\{ - \left| \frac{r}{\lambda_a} \right| \right\} J_0(2\pi s_2 r) r dr \\ \times \int_{-\infty}^{\infty} \exp \left\{ - |z| / \lambda_c \right\} \exp \left\{ - 2\pi i z s_1 \right\} dz . \quad (56)$$

For the intensity along  $s_2$  one obtains by Hankel Transformation

$$I(0, s_2) = \frac{8\pi^2 I_e V_x \langle n^2 \rangle \lambda_a^2 \lambda_c}{(4\pi^2 \lambda^2 s_2^2 + 1)^{3/2}} . \quad (57)$$

A plot of  $[I(s_2)]^{-2/3}$  vs  $4\pi^2 s_2^2$  will be linear with a ratio of slope to intercept equal to  $\lambda_a^2$ . For the case of a slice along  $s_2$ , one obtains

$$I(s_1, 0) = \frac{4\pi I_e V_x \langle n^2 \rangle \lambda_a P_c}{1 + 4\pi^2 \lambda_c^2 s_1^2} . \quad (58)$$

A plot of  $[I(s)]^{-1}$  vs  $4\pi^2 s_1^2$  will be linear with a ratio of slope to intercept equal to  $\lambda_c^2$ .

#### e. Analysis of Diffuse SAXS from Selected Fibers and Films

SAXS patterns were recorded from PBT fiber bundles and stacked films using the 10 m ORNL SAXS Camera with a 64 x 64 element position sensitive detector. The data were corrected point-by-point for dark current, parasitic scatter, and detector sensitivity. Typical isointensity contour plots for as-spun and heat-treated fibers are shown in Figure 32. Intensity profiles two channels wide were then extracted along the equator ( $s_2$ ) and the meridian ( $s_1$ ). These intensity profiles were then analyzed for agreement with the models outlined in sections 3a - 3d and the numerical results are given in Table 6. For comparison purposes, the processing histories are given in Table 7. These will be discussed in detail below.

A typical Guinier type plot along  $s_2$  for PBT is shown in Figure 34.

Such plots are always highly curved which implies that a cylindrical Gaussian correlation function is not a good model for this system. Nevertheless, the anisotropic Guinier analysis is still valid so the limiting slope at small angles ( $2\pi s R_g < 1.5$ ) has been measured and the projected radii of gyration are given in Table 6. All the films examined were processed from PPA solutions and possess voids which have a radius of gyration of 10 - 12 nm perpendicular to the extrusion direction. With the exception of heat treatment, changes in processing variables appear to have no effect upon the average radius of gyration of the microvoids within experimental error. For example films extruded from PPA dopes with substantially different SDRs have essentially the same projected radius of gyration perpendicular to the extrusion direction. Although the extrapolation to zero angle for radius of gyration was difficult for PBT-28413-39-7, this sample appeared to have voids three times as long as wide, in agreement with the results from the Kevlar sample measured.

The void radius in the Kevlar 49® sample calculated assuming ellipsoidal voids was about 3 times larger than reported by Dobb *et al.* [64]. This must be due to difference in commercial samples or angular ranges used. Dobb's minimum value of  $|s|$  was  $2.9 \times 10^{-2} \text{ nm}^{-1}$  compared to  $2.0 \times 10^{-3} \text{ nm}^{-1}$  in this work. Thus, larger voids could be measured on the ORNL apparatus, and this is reflected in the average value.

Guinier and Fournet [57] have shown that the average radius of gyration is given by

$$\langle R_g^2 \rangle = \frac{\sum_k p_k n_k^2 R_k^2 g_k}{\sum_k p_k n_k^2} \quad (59)$$

where  $P_k$  are the number of particles of type  $k$  and  $n_k$  are the number of electrons in the particles of type  $k$ . Assuming that all particles are geometrically similar and that  $n_k$  is proportional to the volume of the particles, then  $n_k$  is proportional to  $R^3$ . Substituting for  $n_k$  in equation 54,

$$\langle R_g^2 \rangle = \frac{\sum_k P_k R_{gk}^8}{\sum_k P_k R_{gk}^6} \quad . \quad (60)$$

Thus the average radius of gyration is strongly influenced by the larger voids. Since the largest voids scatter at the smallest angles, the average radius of gyration will be sensitive to the small angle limit.

A typical Debye type plot is shown in Figure 35. These curves tend to have linear asymptotes at low and high  $s$ . If one refers to the assumptions in the development of Summerfield and Mildner [68], one finds the low angle limit to be desired value. This low angle limit should be  $1/2$  of  $\langle R_g^2 \rangle$  suggesting that  $\langle R_g^2 \rangle^{1/2}$  should equal  $1.41 \langle \ell^2 \rangle^{1/2}$ .

Scrutiny of Table 6 suggests that the low angle limit of  $\langle \ell^2 \rangle^{1/2}$  is generally equal to  $\langle R_g^2 \rangle^{1/2}$  which implies the approximation does not hold. The development of Guinier's law assumes a dilute suspension of particles. Guinier and Fournet [57] have shown that as the concentration of a suspension increases, the smallest angle scattering is decreased. This type of behavior would lead to a lower value of  $\langle R_g^2 \rangle$  than predicted. Perhaps this type of behavior accounts for the discrepancy in the measured value of  $\langle R_g^2 \rangle$  and that predicted from  $\langle \ell_a^2 \rangle$ .

A plot of the same data for a cylindrical exponential correlation function is shown in Figure 36. These plots generally exhibit positive deviation from

linearity. Frequently the intercepts are so small that they are negative when a linear least squares regression analysis is performed. Even when the intercepts are positive, the error is sufficiently large to result in large errors in the cylindrical correlation length  $\langle \xi_{\text{cy}}^2 \rangle^{1/2}$ . Therefore this model is not particularly useful for analysis of microvoids in PBT.

A plot of the projected correlation function obtained by Fast Fourier Transformation [69] of the data is given in Figure 37. The data up to  $|s| \approx 2 \times 10^{-2} \text{ nm}^{-1}$  were used and were flipped about the last point to make a periodic function for discrete transformation. If one tries to graphically estimate the first zero of the projected  $\gamma(r_2)$  one obtains about 100 nm. For an isolated sphere of radius  $R$ ,  $\gamma(r)$  reaches zero for  $r = 2R$  [72]. If we assume this to be true for the general case of non-spherical particles, this would imply a projected diameter of about 100 nm for this sample. This is roughly twice the size predicted if one assumes that the voids are ellipsoidal and derives the radius using the formula from Hosemann and Bagchi [72] and 10 times the size of the projected radius of gyration.

f. Comparison of the Models for Data Analysis

For comparison purposes, the best method is to directly examine the correlation function. Although it is difficult to relate the correlation function to physical dimensions in the sample, one can make relative statements. Examination of correlation lengths obtained from the Summerfield-Mildner [68] analysis and the projected radii of gyration from Summerfield et al. [68] and Stein [70] have thus far proved to be most useful. As long as one is careful to make comparisons on data from instruments with the same angular range and is

careful to take the limiting slope at small angles, useful comparison of data may be made with these models.

g. Correlation of Void Size with Processing Conditions

Before proceeding further, it is worthwhile to discuss the results of an experiment in which 28413-24-10 was swollen with water and examined by SAXS while still wet. The total scattered intensity from the wet sample after correction for background was significantly smaller than the dry sample. However, the projected correlation length perpendicular to the fiber axis in the wet sample was identical, within experimental error, to that from the dry sample. This confirms our model of voids within a matrix of PBT.

From Tables 6 and 7 we see that the average microvoid size determined from the projected radius of gyration and projected correlation length in fibers from MSA solution decreases upon heat treatment. A similar trend is seen in fibers from PPA solution. Since the scattered intensity of heat treated fiber bundles is greater than that of as-spun fiber bundles with similar thickness, this indicates that fibrillation increases the number of voids, but the lateral packing in the fiber is improved, resulting in fewer large voids and a smaller total fiber cross sectional area. That is, the fibrils fill in some of the larger voids. Films extruded from PPA with significantly different SDR contain large microvoids which appear to be unaffected by SDR. Heat treatment results in microvoids slightly smaller than those in the as-spun ribbons with a slight increase in the scattered intensity. This implies that there is less fibrillation during heat treatment in films from PPA solution.

#### 4. Suggestions for Future Experiments

Comparison of the projected void sizes perpendicular to the extrusion direction in PBT films extruded from PPA solutions at similar SDRs but different extrusion temperatures indicates that extrusion temperature does not affect the void size in the small angle region. This implies that the large voids reported in Chapter IV which increased with extrusion temperature must arise by a different mechanism than the voids observed by SAXS.

In the future, it would be interesting to have a quantitative measure of the volume fraction of microvoids accessable to small angle x-ray scattering. This may be achieved through the SAXS integrated intensity termed the invariant, Q [73]

$$Q \equiv \iiint I_n(s) dv_s \quad (61)$$

where  $I_n$  is the intensity normalized to that of the incident beam. For uniaxial symmetry,  $I$  is only a function of  $s_{r_2}$  and  $\phi_2$  and not a function of  $s_{\psi_2}$  (see Figure 34).

$$Q = \int_{s_{\phi_2}=0}^{\pi} \int_{s_{\psi_2}=0}^{2\pi} \int_{s_{r_2}=0}^{\infty} I_n(s_{r_2}, s_{\phi_2}) s^2 \sin\phi_2 ds_r ds_{\phi_2} ds_{\psi_2} \quad (62)$$

$$Q = 2\pi \int_{s_{\phi_2}=0}^{\pi} \int_{s_{r_2}=0}^{\infty} I(s_r, s_{\theta}) s_r^2 \sin\phi_2 dr d\phi_2 . \quad (63)$$

Following the geometry of Crist [43] we make a change of variable:

$$s_1 = s_{r_2} \cos\psi \quad s_2 = s_{r_2} \sin\psi \quad \text{and} \quad dA = ds_1 ds_2 = s_{r_2} dr_2 dr_{\psi}$$

Substituting these values into equation 63, one obtains

$$Q_{2-D} = 2\pi \int_{s_1=-\infty}^{\infty} \int_{s_2=-\infty}^{\infty} I_n(s_1, s_2) s_2 ds_1 ds_2 \quad (64)$$

or, only using one quadrant of  $s_1-s_2$  space

$$Q_{2-D} = 4\pi \int_{s_1=0}^{\infty} \int_{s_2=0}^{\infty} I_n(s_1, s_2) s_2 ds_1 ds_2 \quad (65)$$

$Q$  may be related to the mean squared electron density fluctuation,  $\langle \eta^2 \rangle$  [73]

$$Q = \frac{\langle \eta^2 \rangle i_e N_A d}{4\pi a^2} \quad (66)$$

where  $\langle \eta^2 \rangle$  is the mean squared electron density fluctuation (moles<sup>2</sup> electrons cm<sup>-6</sup>)

$i_e \equiv$  Thompson's factor  $7.94 \times 10^{-26}$  cm<sup>2</sup>

$N_A \equiv$  Avagadro's Number

$d \equiv$  the sample thickness (cm)

$a \equiv$  the sample-to-detector distance (cm) .

For a two phase system with sharp boundaries, the mean squared electron density fluctuation is given by [73]

$$\langle \eta^2 \rangle = \phi_1 \phi_2 \Delta \rho^2 \quad (67)$$

where  $\phi_1$  and  $\phi_2$  are the volume fractions of the respective phase and  $\Delta \rho^2$  is the

square of the difference of the electron density of the two phases.

For a system of voids in PBT, then  $\Delta\rho^2$  becomes  $\rho_{PBT}^2$  and we obtain an equation for the volume fraction of voids,  $\phi_i$

$$\phi_i (1-\phi_i) = \frac{4\pi a^2 Q}{\rho_{PBT}^2 I e^{N^2 d}} . \quad (68)$$

The  $\rho_{PBT}^2$  equals 0.71 moles<sup>2</sup> electrons cm<sup>-6</sup> so equation (68) reduces to

$$\phi_i (1-\phi_i) = 6.14 \times 10^{-22} a^2 Q/d . \quad (69)$$

This would be an excellent area for future work but would require careful determination of sample thickness, necessitating flat fiber bundles such as those used by Heikens et al. [63]. One would also have to subtract the intensity for electron density fluctuations within the PBT phase which occur at high angle. This is termed the liquid-like scatter, and may be obtained from the slope of a Porod plot [75], a plot of  $16\pi^4 I s^4$  and  $16\pi^4 s^4$ .

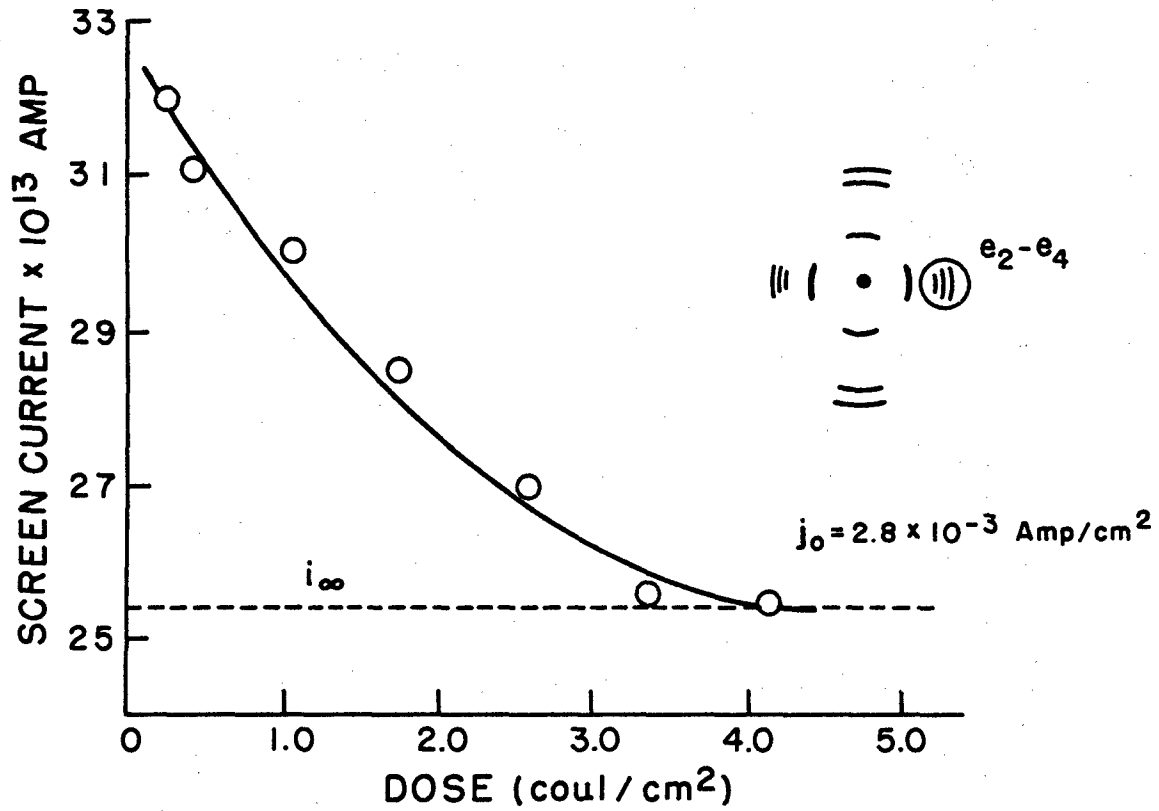


Figure 11. Decay of  $e_2 - e_4$  for PBT at a dose rate,  $j_0 = 2.8 \times 10^{-3}$  coul/cm $^2$  sec $^{-1}$ . Inset: schematic of electron diffraction pattern showing approximate radius of objective aperture.

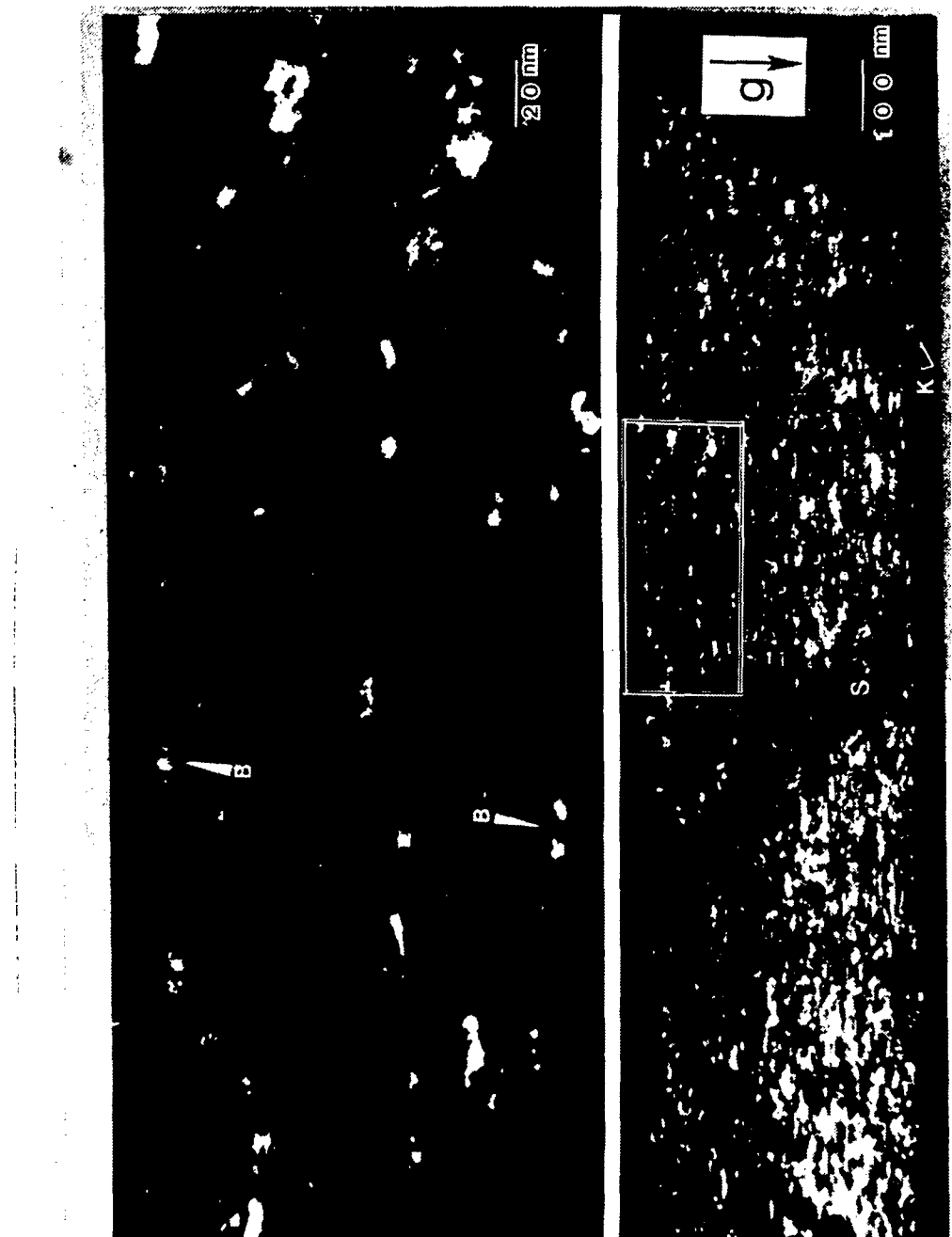


Figure 12. DF micrograph of PBT fragment suspended over a gold decorated, perforated support film (S). "K" denotes kinked area. Extrusion direction is vertical. Instrumental Magnification = 33,000X. Top: Enlargement of boxed area at bottom. "B"s denote probable buckled regions.

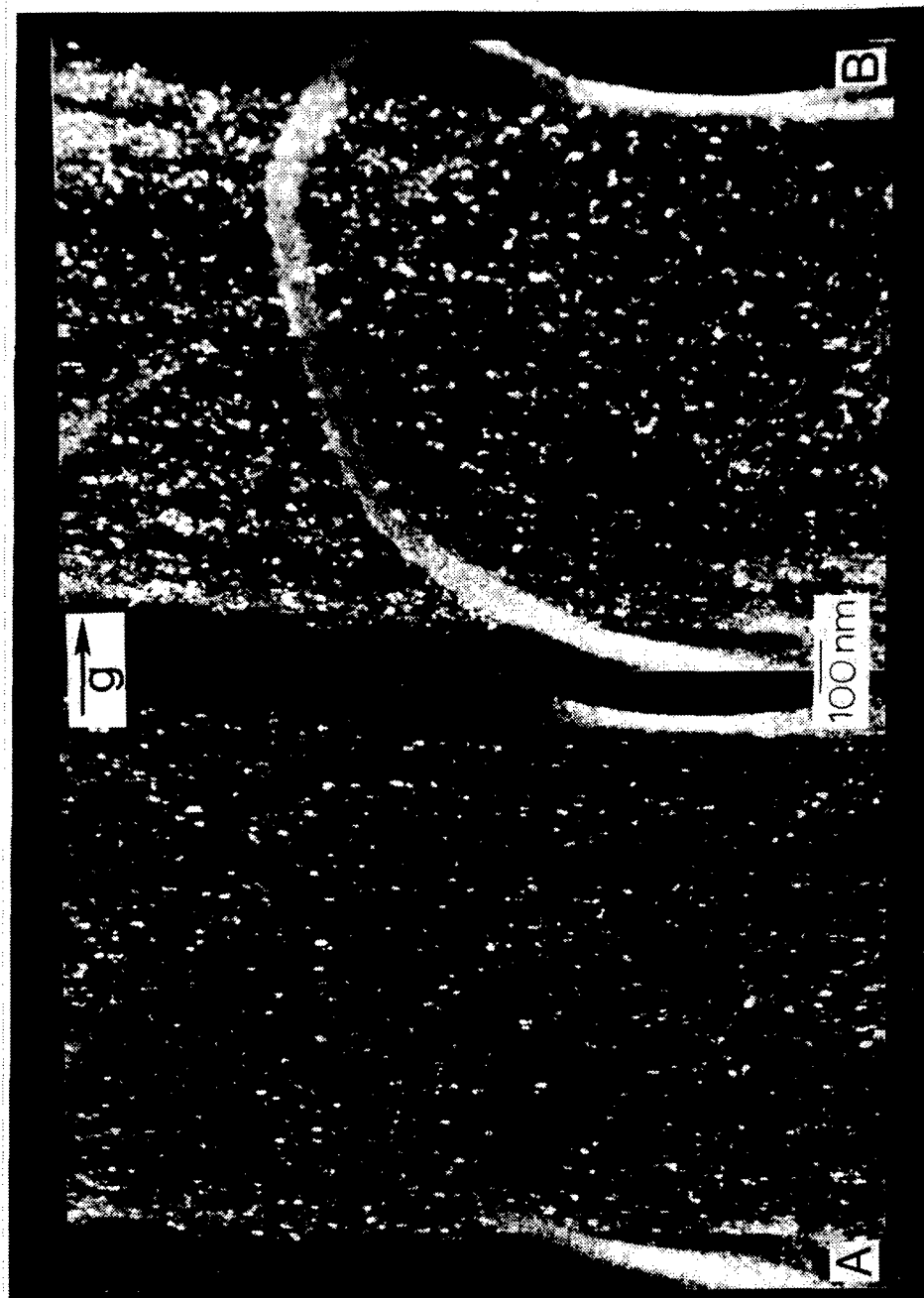
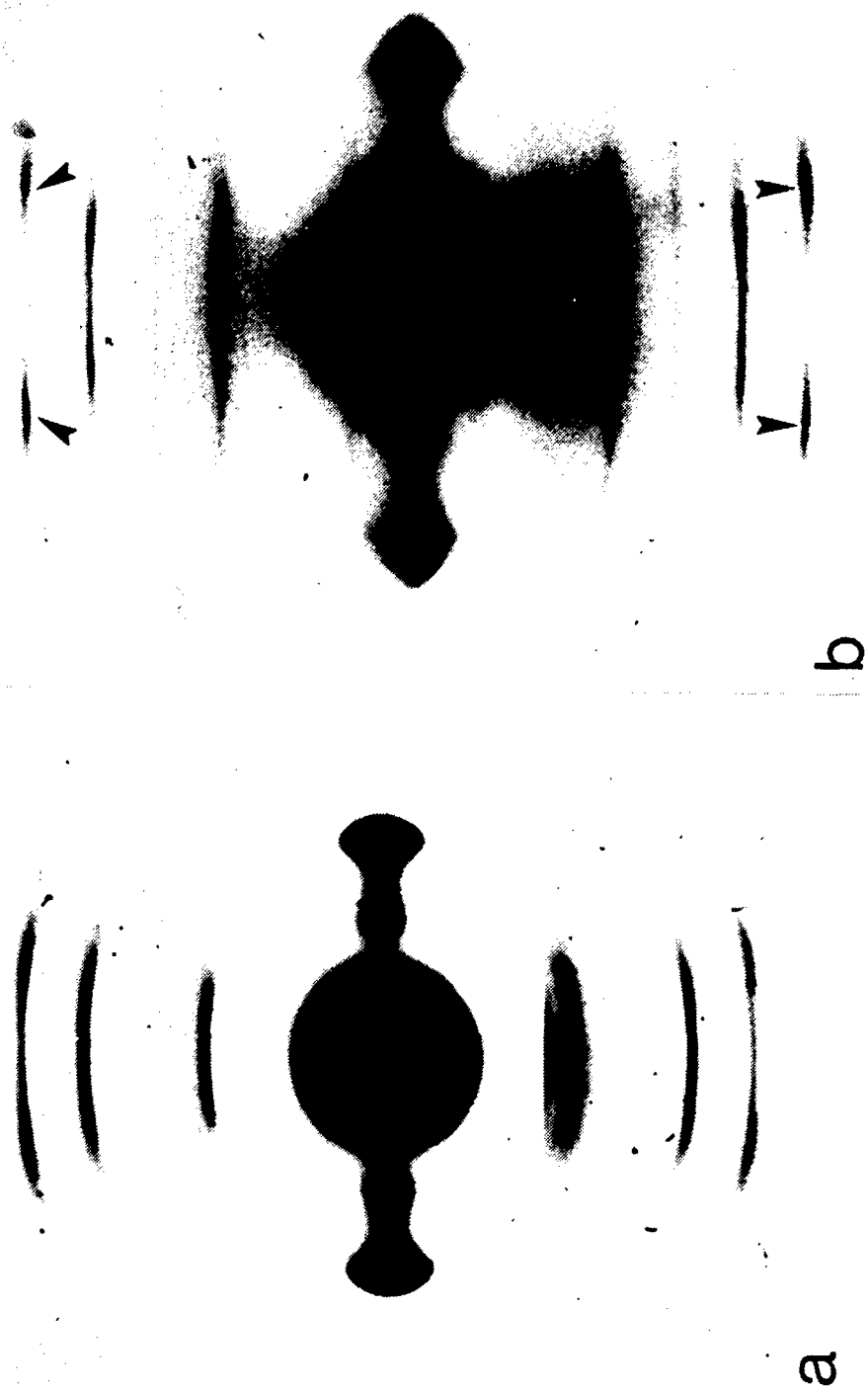


Figure 13. DF micrographs (10,000 instrumental magnification) of the same area of a PBT film using  $e_2-e_4$  and  $e_1$  reflections, respectively.

Figure 14. (a) Electron diffraction pattern of a typical 'as-spun' PBT fiber;  
(b) Electron diffraction pattern of typical 'heat treated' PBT fiber. Arrows indicate splitting of sixth layer line.



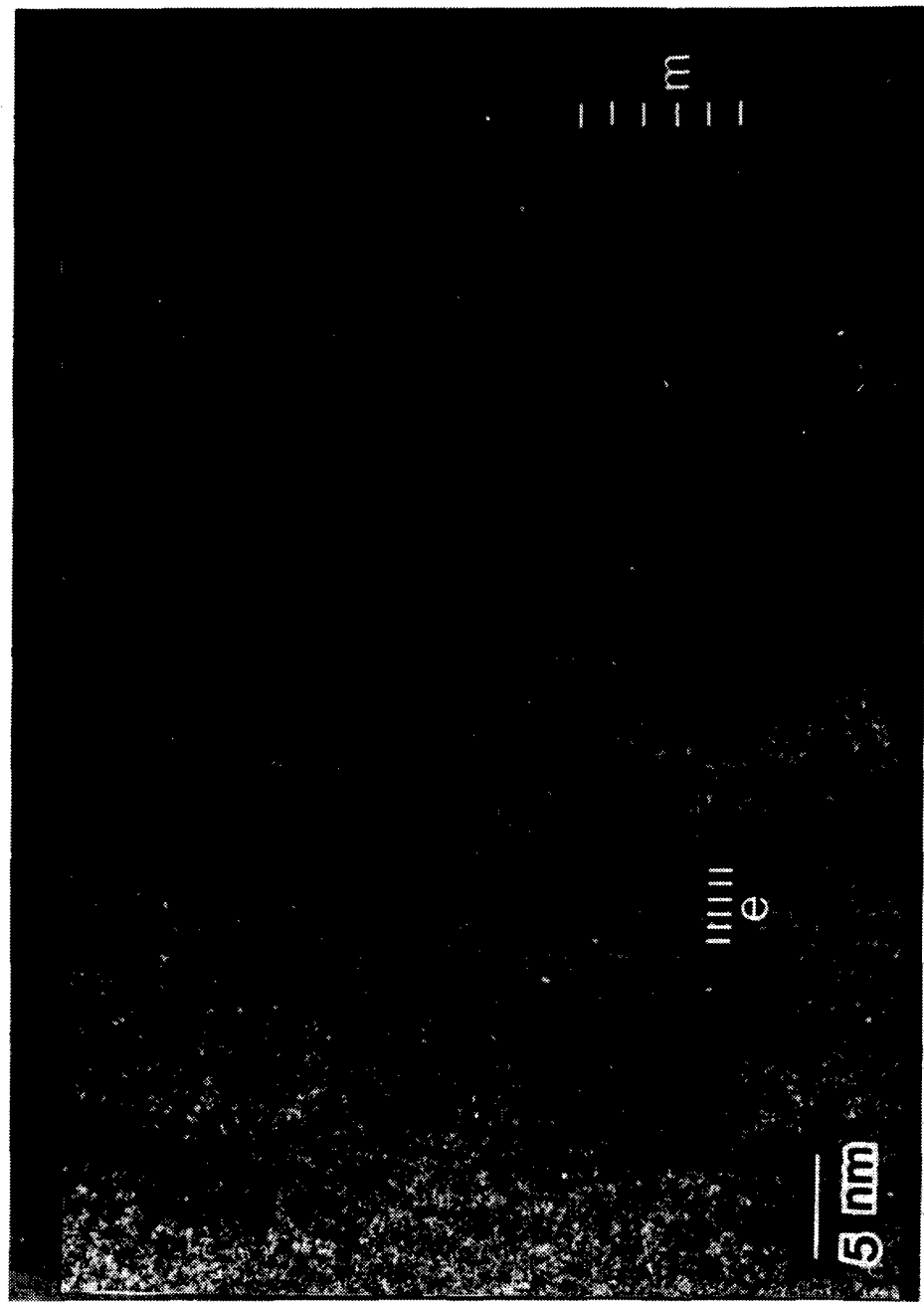
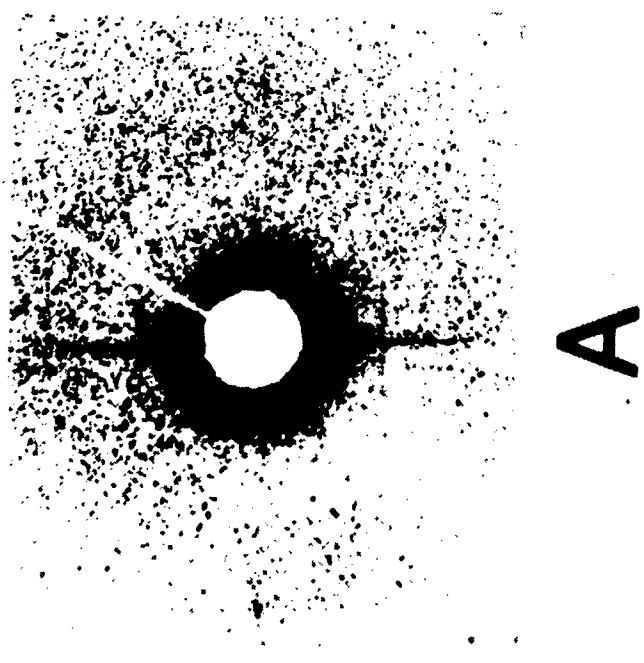


Figure 15. Two regions of an axial bright field lattice image (100,000 $\times$  instrumental magnification) of a tension heat treated fiber.



- + -

B

Figure 16. (a) Optical transform of micrograph used to obtain Figure 15.  
(b) Schematic of Figure 3.6a. Sharp spots are due to .59 nm E  
fringes and diffuse streaks to 1.24 nm M fringes.

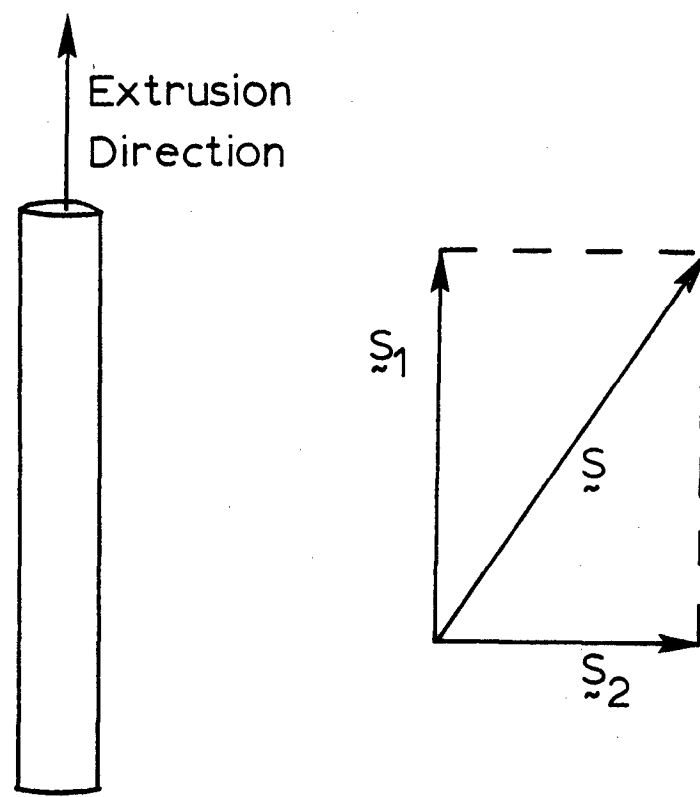


Figure 17. Definition of the scattering vectors used.

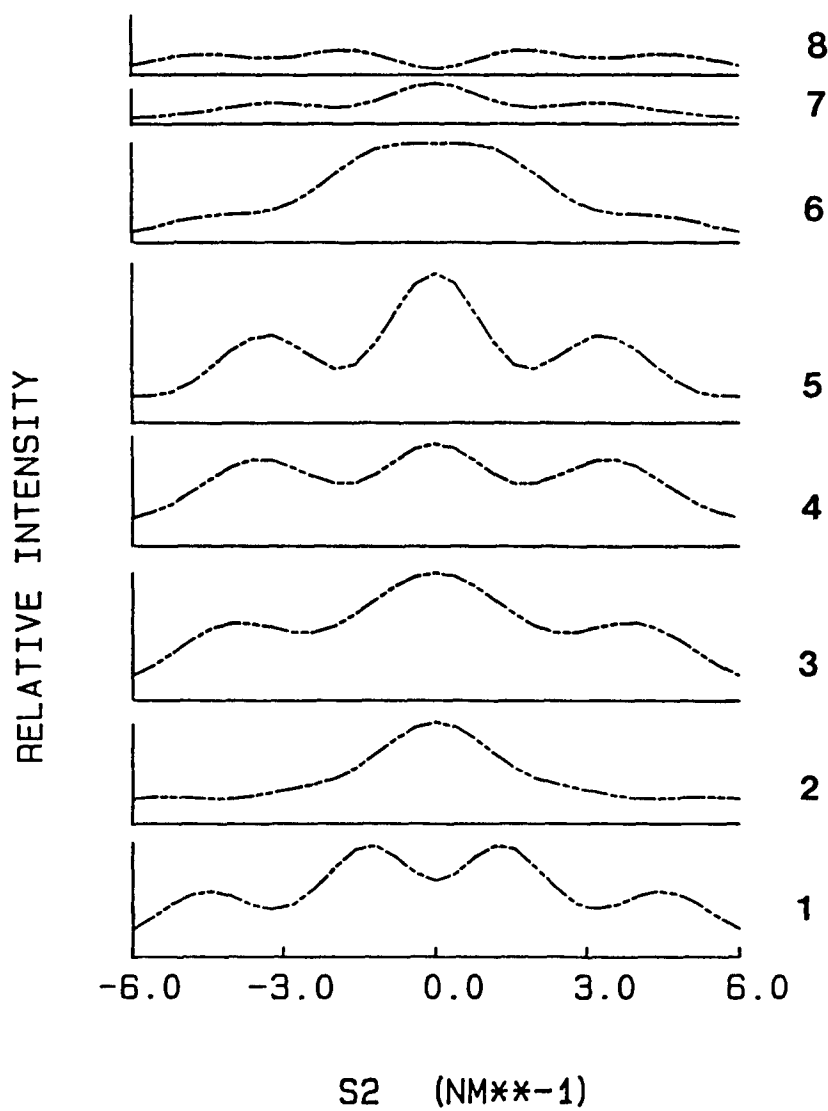


Figure 18. Cylindrically averaged molecular transform for a single PBT chain of 8 units using coordinates of Odell et al. [7]. Temperature factor (.025 nm<sup>2</sup> perpendicular to chain and .005 nm<sup>2</sup> parallel to chain axis).

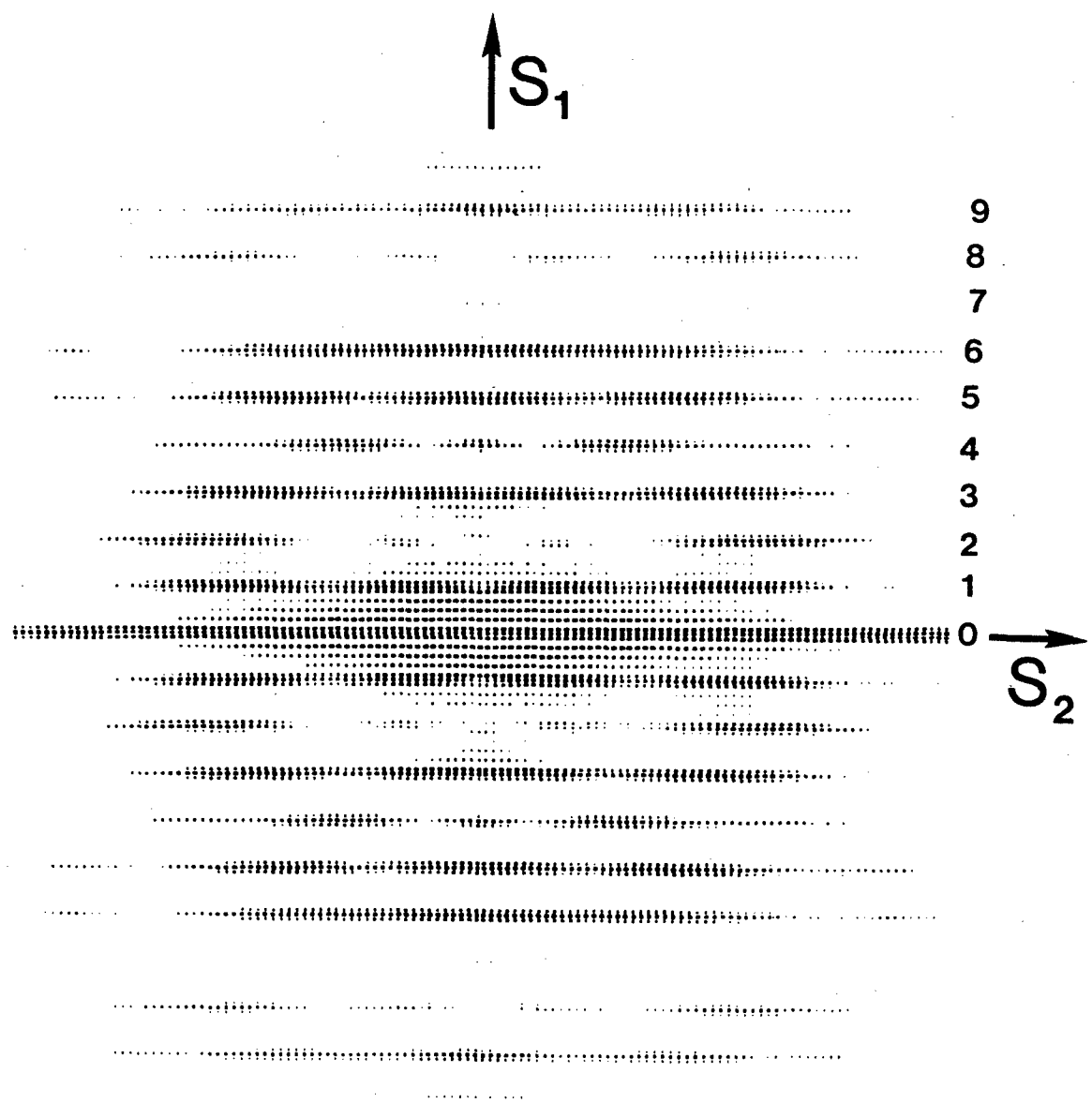


Figure 19. Matrix printer output of cylindrical averaged molecular transform for a single PBT chain of 8 units by Odell et al. [7].

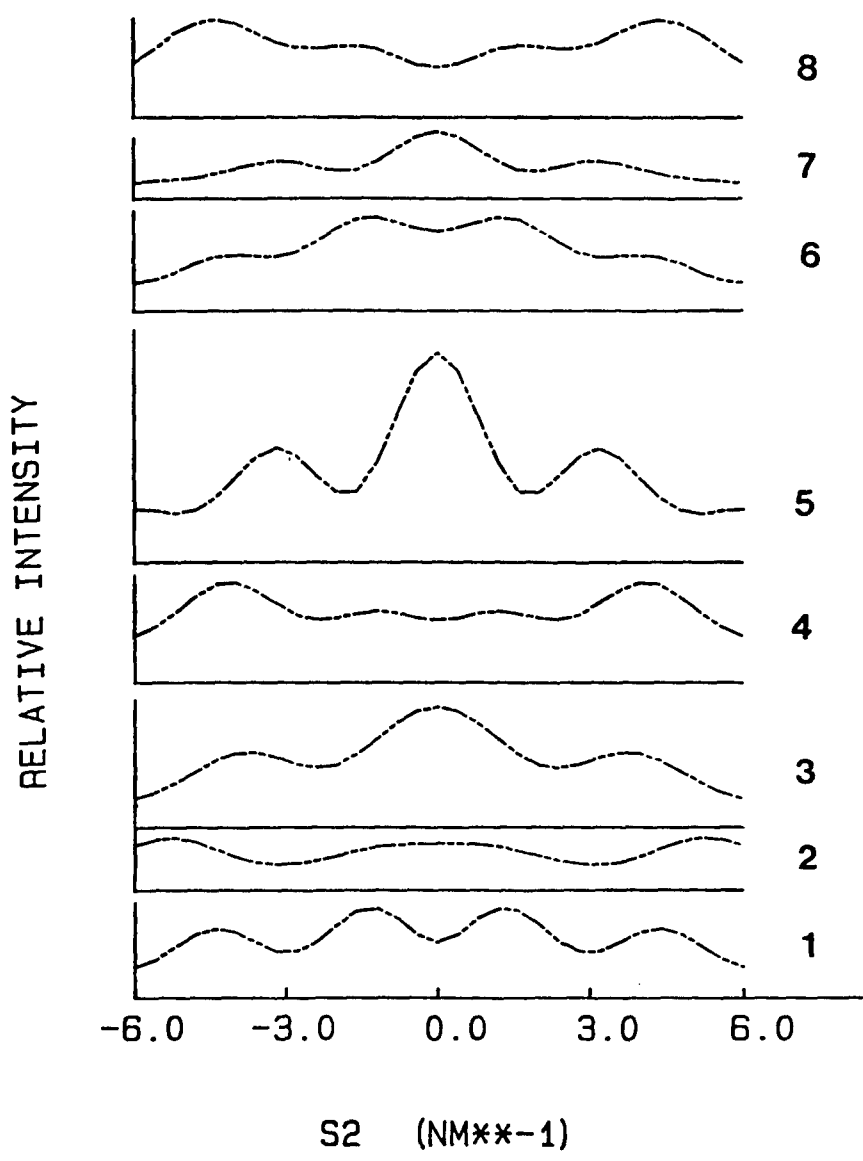


Figure 20. Cylindrical averaged molecular transform for a single PBT chain of 8 units using coordinates of Wellman et al. [44]. Temperature factor .025 nm<sup>2</sup> perpendicular to chain axis, .005 nm<sup>2</sup> parallel to chain axis.

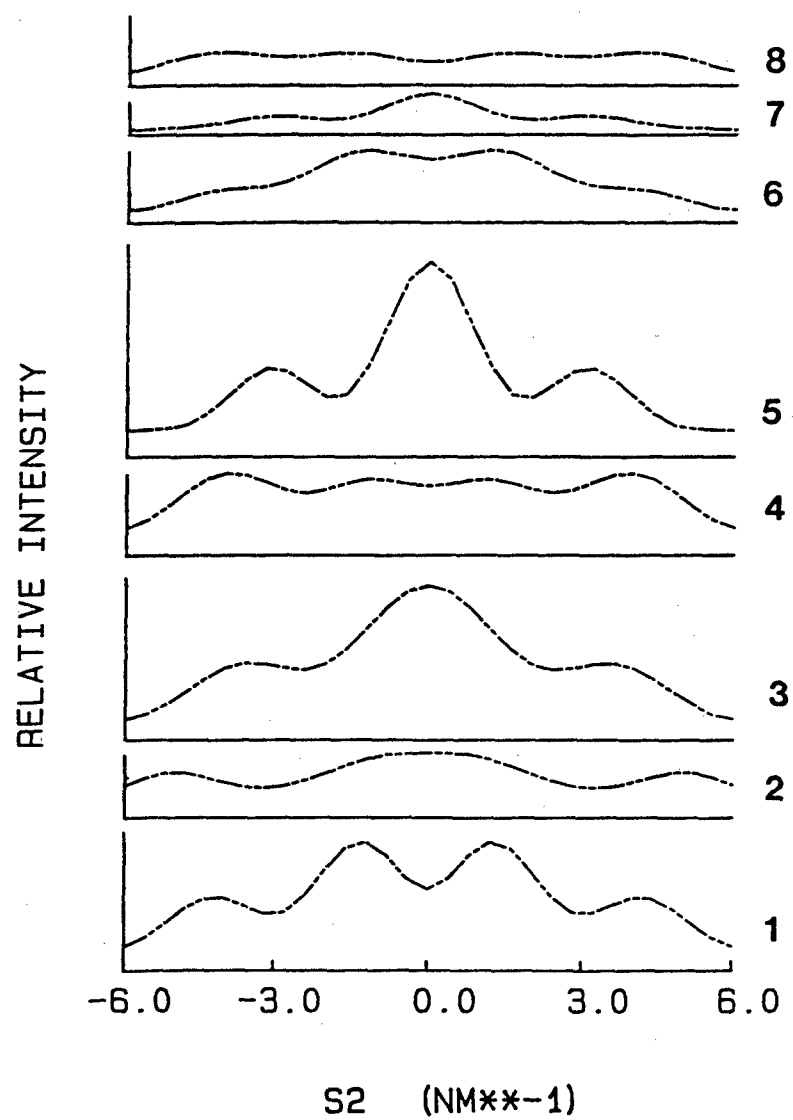


Figure 21. Cylindrical averaged molecular transform for a single PBT chain of 8 units using coordinates of Wellman et al. [7]. Temperature factor  $.06 \text{ nm}^2$  parallel to chain axis and  $.06 \text{ nm}^2$  perpendicular to chain axis.

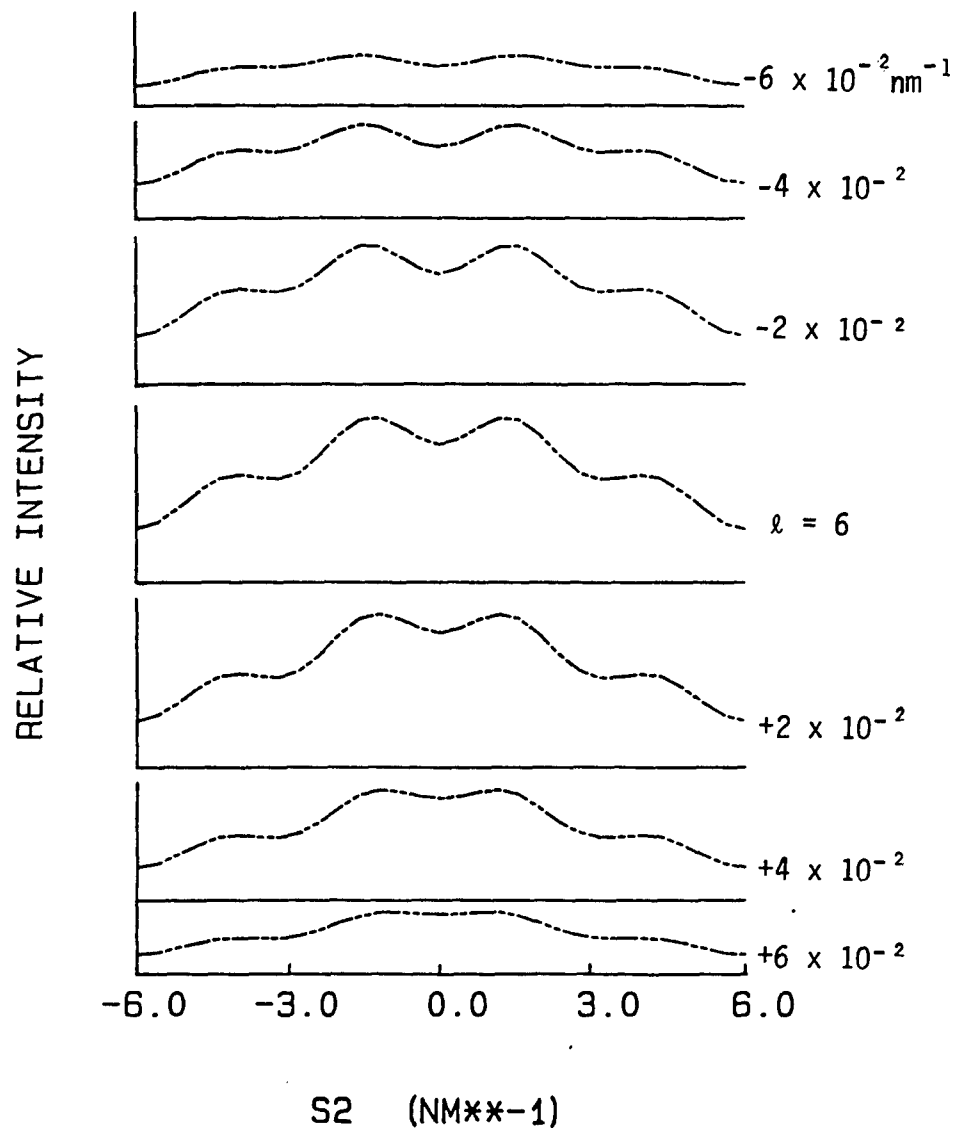


Figure 22. Distribution of intensity about  $\ell = 6$  for case in Figure 20 in steps of  $S_1 = \pm 0.02 \text{ nm}^{-1}$ .

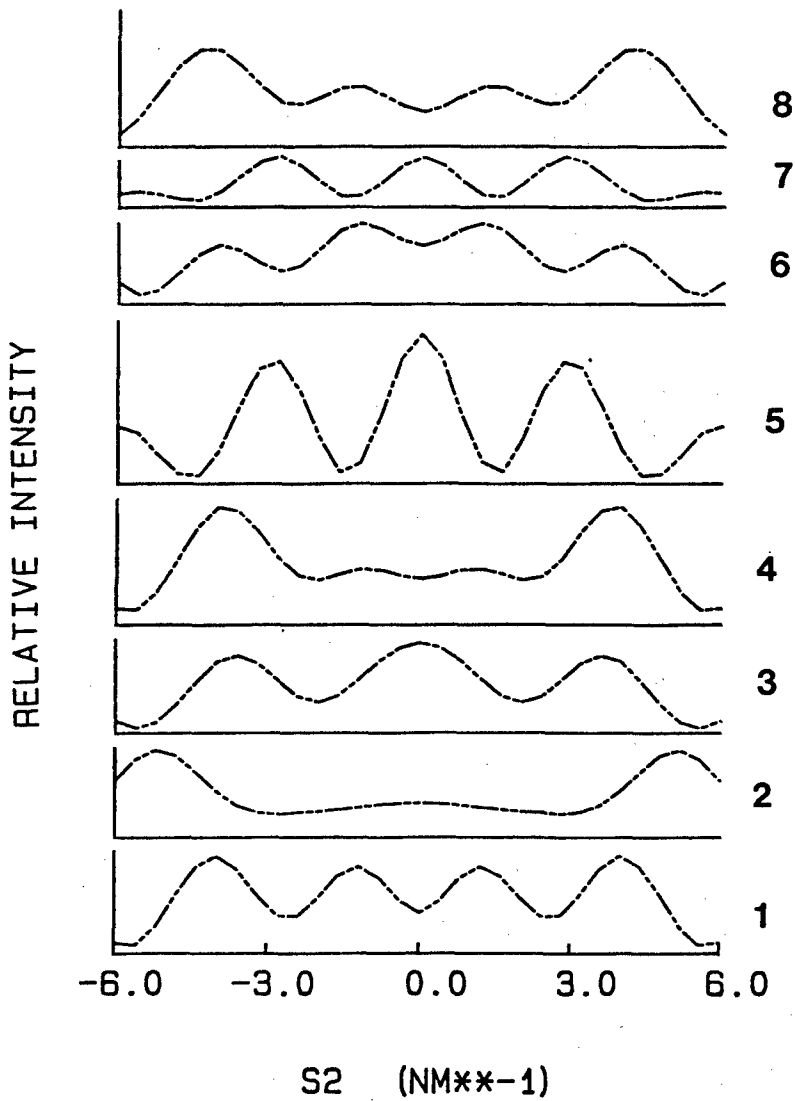


Figure 23. Molecular transform for a single PBT molecule of 8 units.  
 Conformational angle between phenyl and bisthiazole moieties  
 $(\phi) = 35^\circ$  as a function of angle of incidence of beam ( $\alpha$ ).  
 (a)  $\alpha = 0$ .

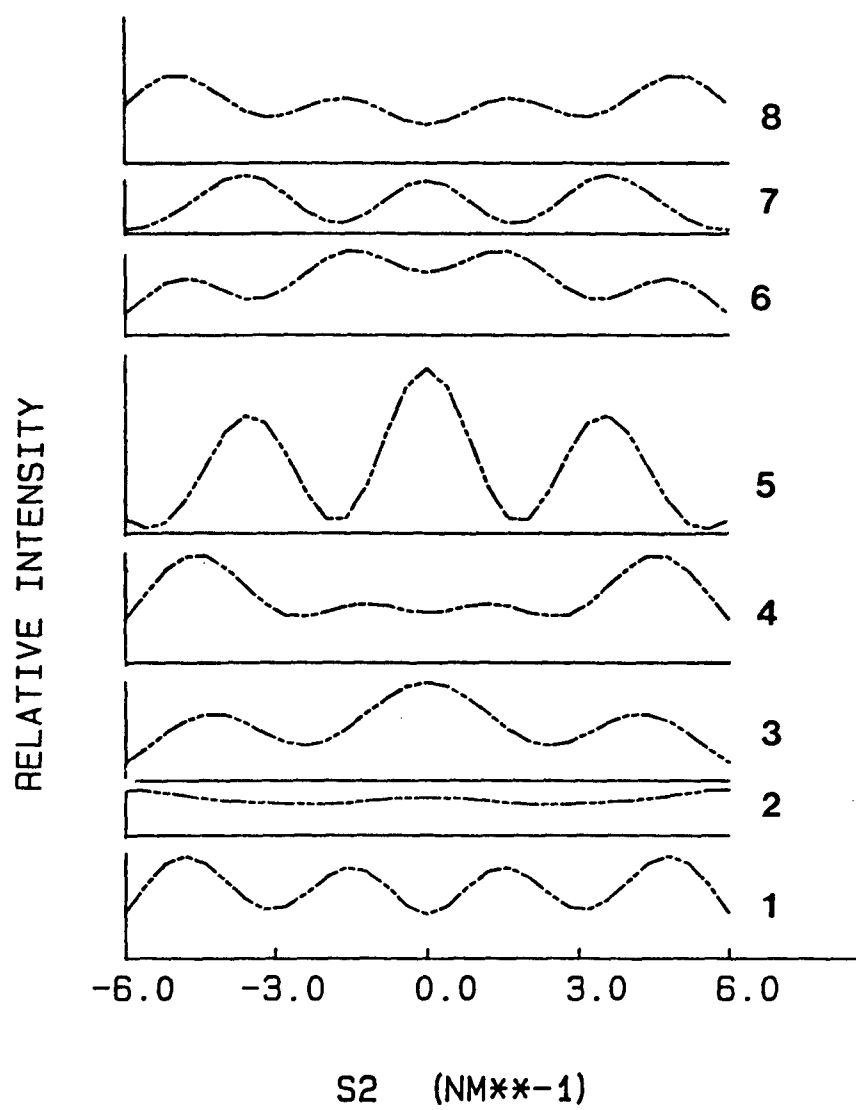


Figure 23. Molecular transform for a single PBT molecule of 8 units.  
 Conformational angle between phenyl and bisthiazole moieties  
 $(\phi) = 35^\circ$  as a function of angle of incidence of beam ( $\alpha$ ).  
 (b)  $\alpha = 35^\circ$ .

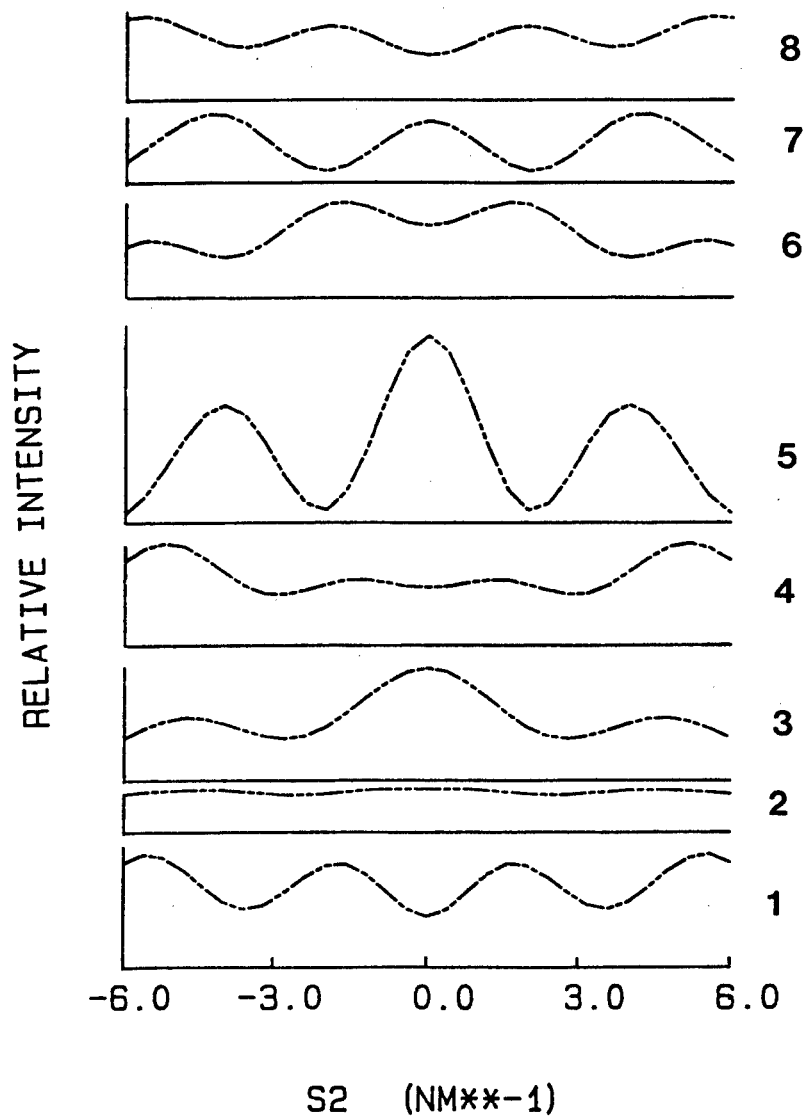


Figure 23. Molecular transform for a single PBT molecule of 8 units.  
 Conformational angle between phenyl and bisthiazole moieties  
 $(\phi) = 35^\circ$  as a function of angle of incidence of beam ( $\alpha$ ).  
 (c)  $\alpha = 45^\circ$ .

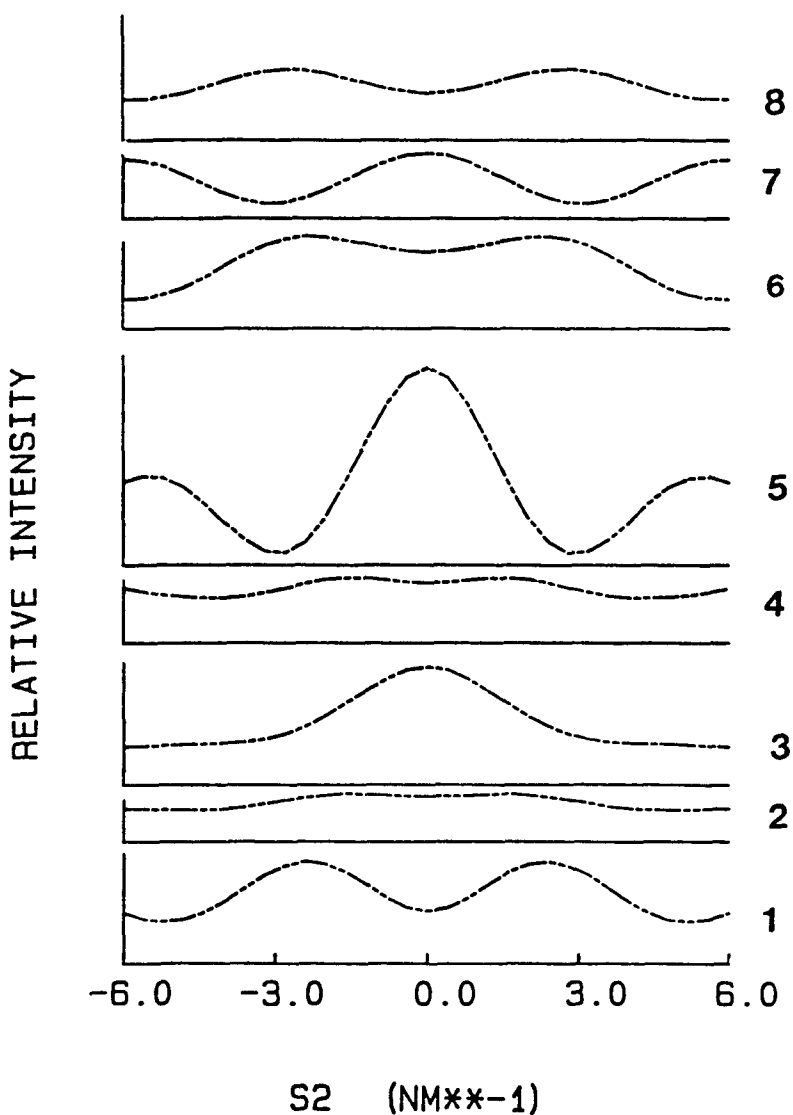


Figure 23. Molecular transform for a single PBT molecule of 8 units. Conformational angle between phenyl and bisthiazole moieties ( $\phi$ ) =  $35^\circ$  as a function of angle of incidence of beam ( $\alpha$ ).  
(d)  $\alpha = 60^\circ$ .

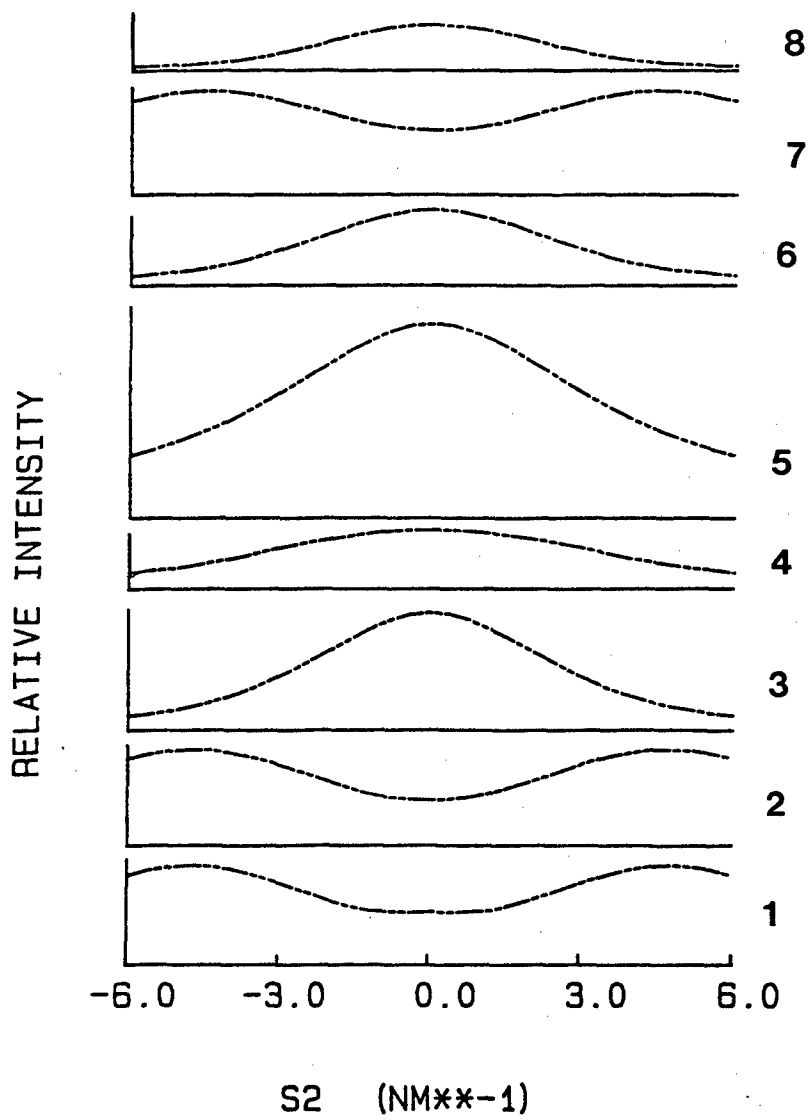


Figure 23. Molecular transform for a single PBT molecule of 8 units. Conformational angle between phenyl and bisthiazole moieties  $\{\phi\} = 35^\circ$  as a function of angle of incidence of beam ( $\alpha$ ).  
 $\{e\}$   $\alpha = 90^\circ$ .

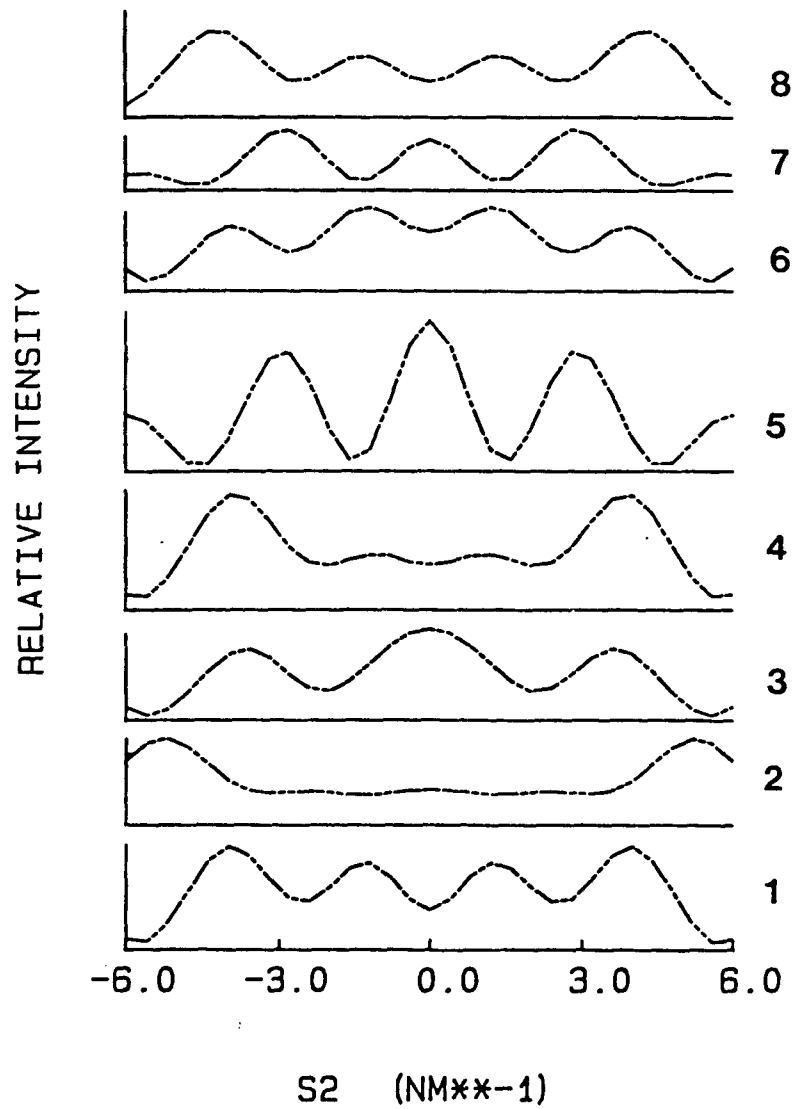


Figure 24. Molecular transform for a single PBT molecule of 8 units.  
 Conformational angle between phenyl and bisthiazole moieties ( $\phi$ ),  
 angle of incidence of beam ( $\phi$ ). (a)  $\phi = 0$ ,  $\alpha = 0$ .

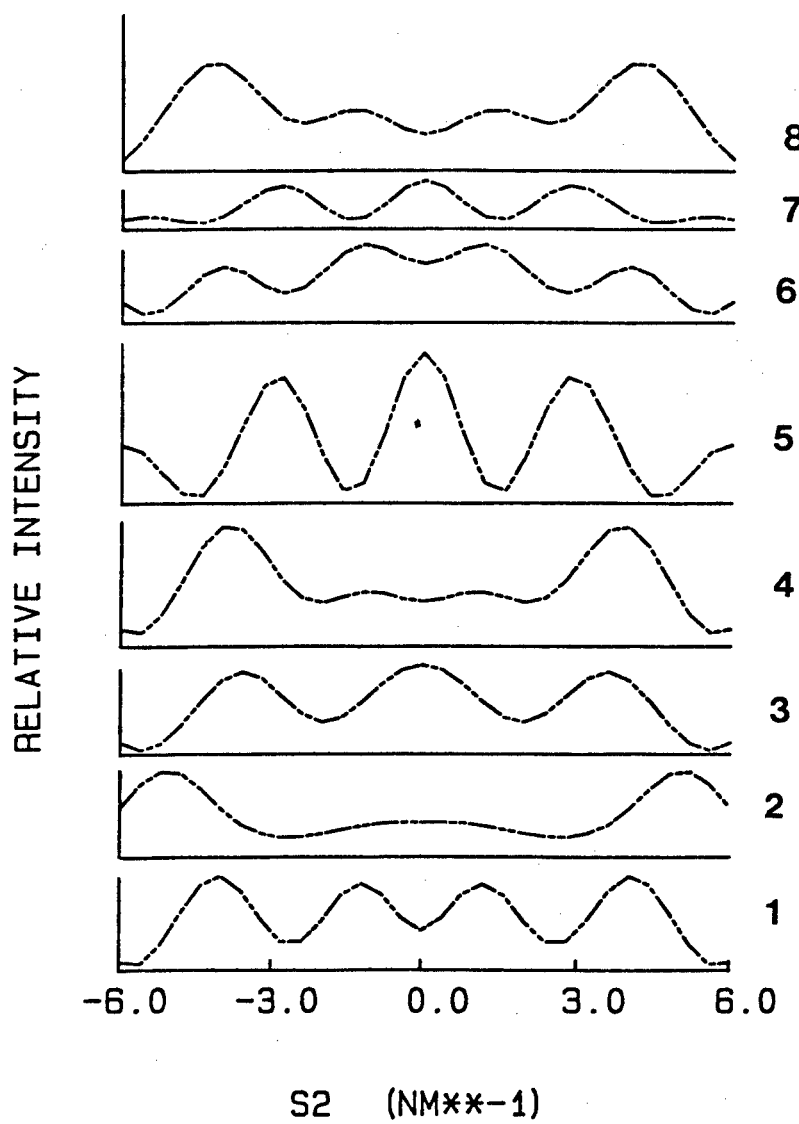


Figure 24. Molecular transform for a single PBT molecule of 8 units. Conformational angle between phenyl and bisthiazole moieties ( $\phi$ ), angle of incidence of beam ( $\phi$ ). (b)  $\phi = 25^\circ$ ,  $\alpha = 0$ .

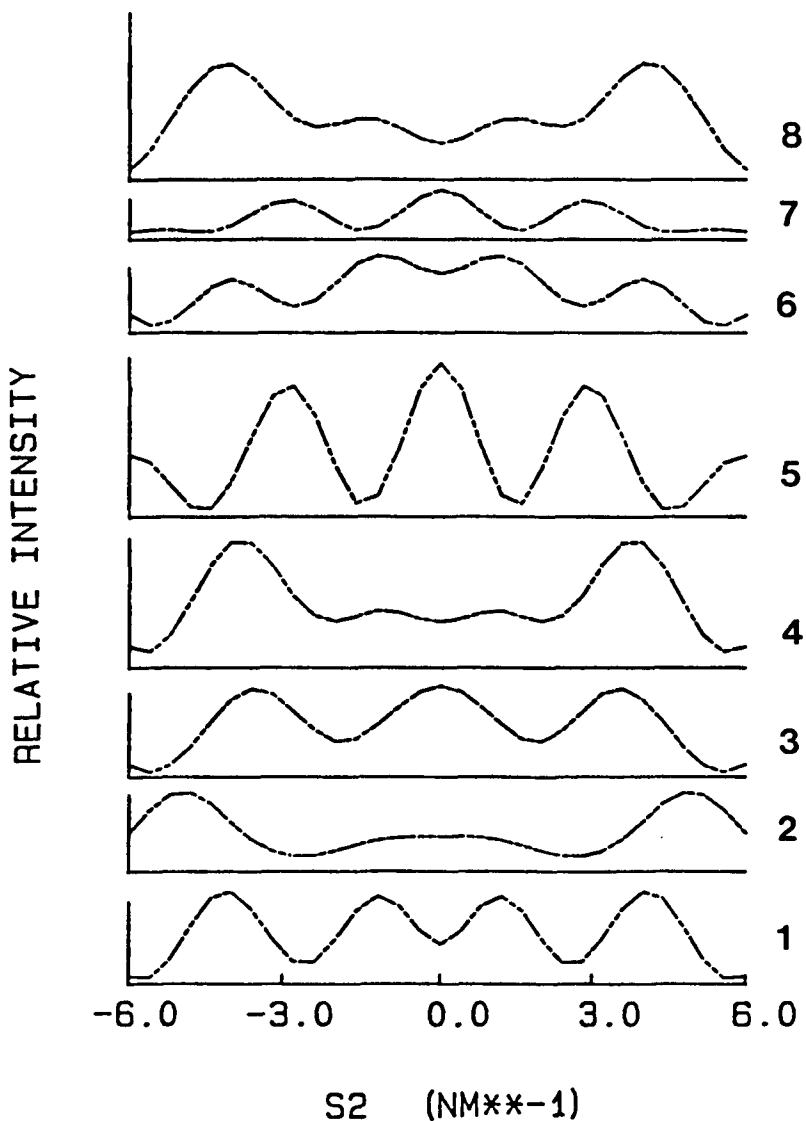


Figure 24. Molecular transform for a single PBT molecule of 8 units.  
Conformational angle between phenyl and bisthiazole moieties ( $\phi$ ),  
angle of incidence of beam ( $\phi$ ). (c)  $\phi = 45^\circ$ ,  $\alpha = 0$ .

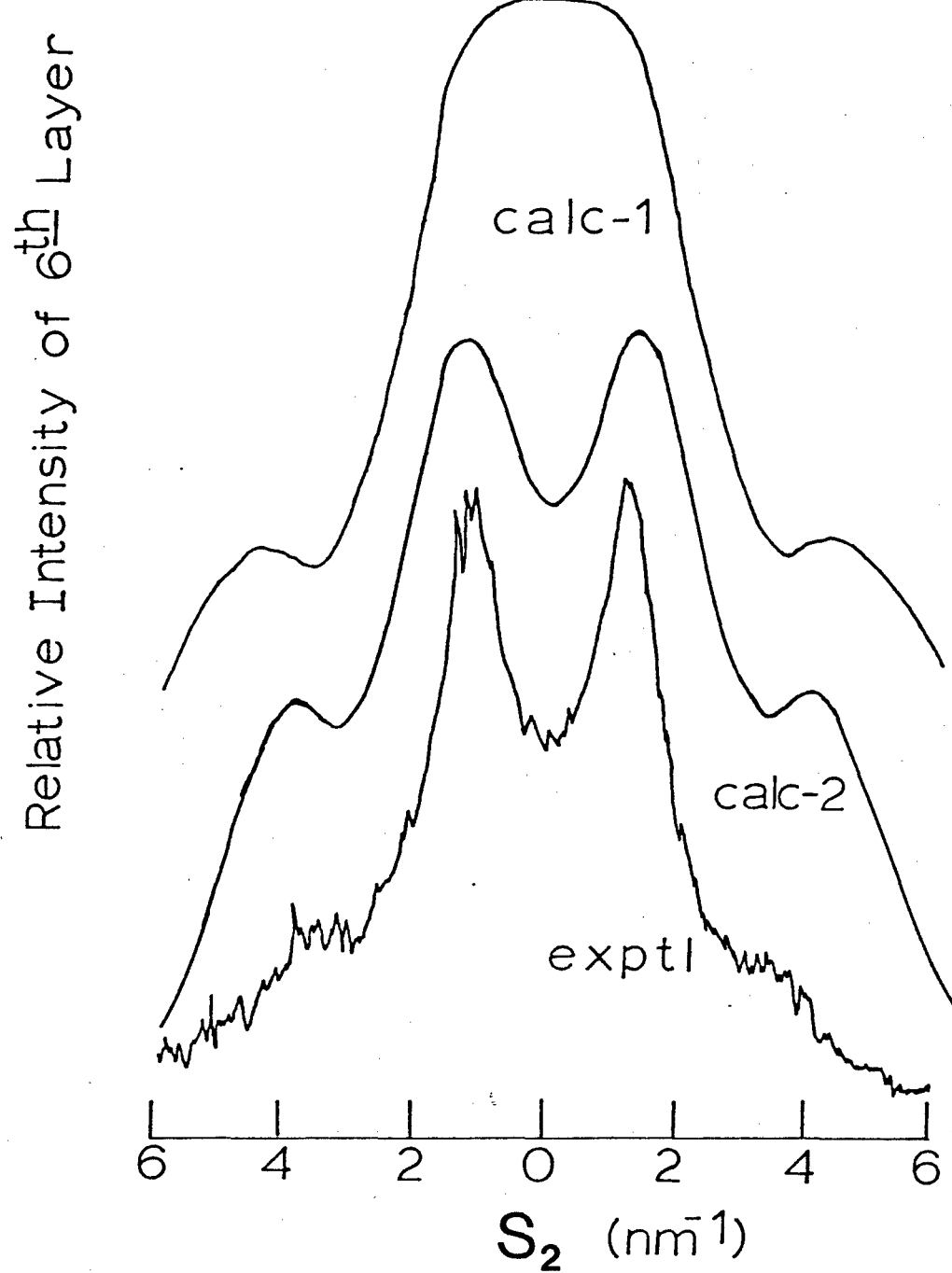


Figure 25. Comparison of cylindrically averaged molecular transforms of PBT chains to measured electron diffraction profile for the sixth layer line. Calc-1 - using coordinates of Odell *et al.* [41]; Calc-2 - using coordinates of Wellmann *et al.* [44]; Exptl - microdensitometer profile.

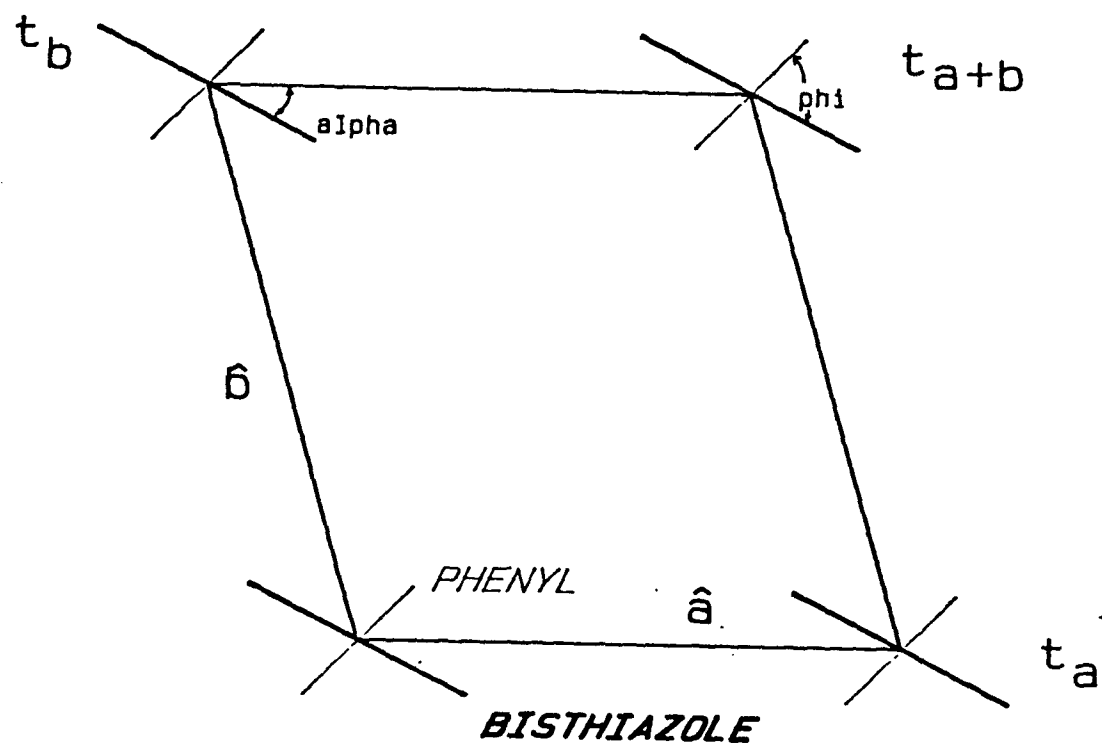


Figure 26. Definition of parameters for conformational calculations.

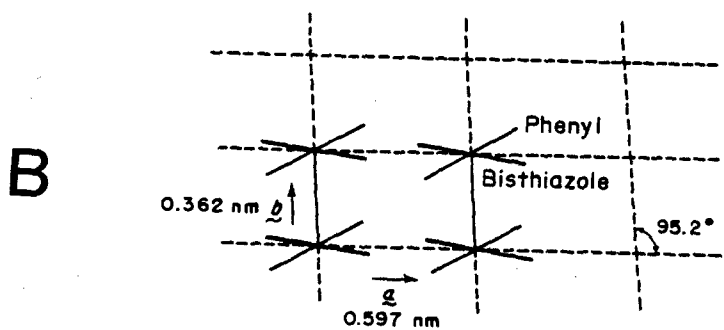
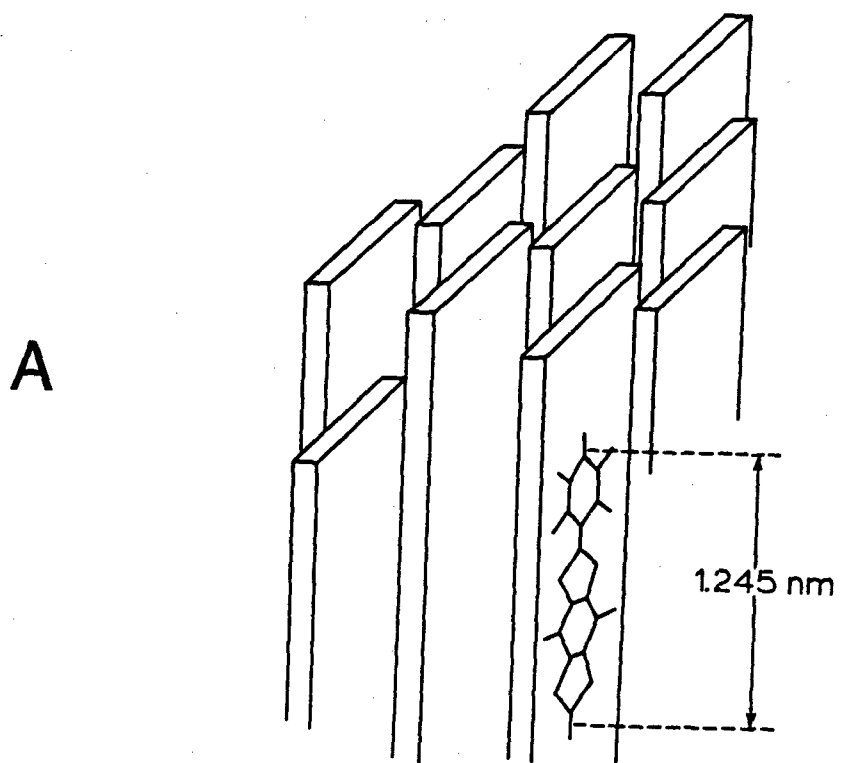


Figure 27. Proposed structure of PBT. Top: monoclinic net. Bottom: chains in net (with translational freedom).

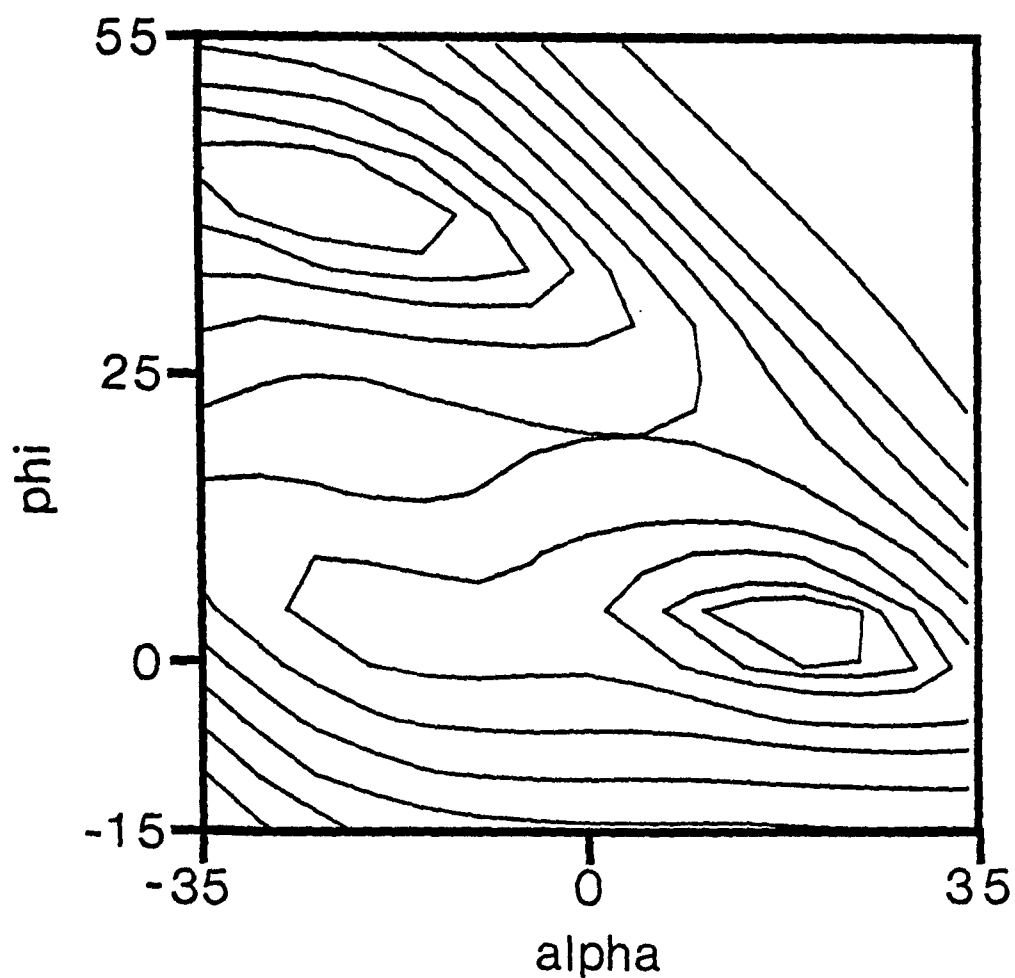


Figure 28. Conformational energy for PBT cell a function of chain rotational angle.

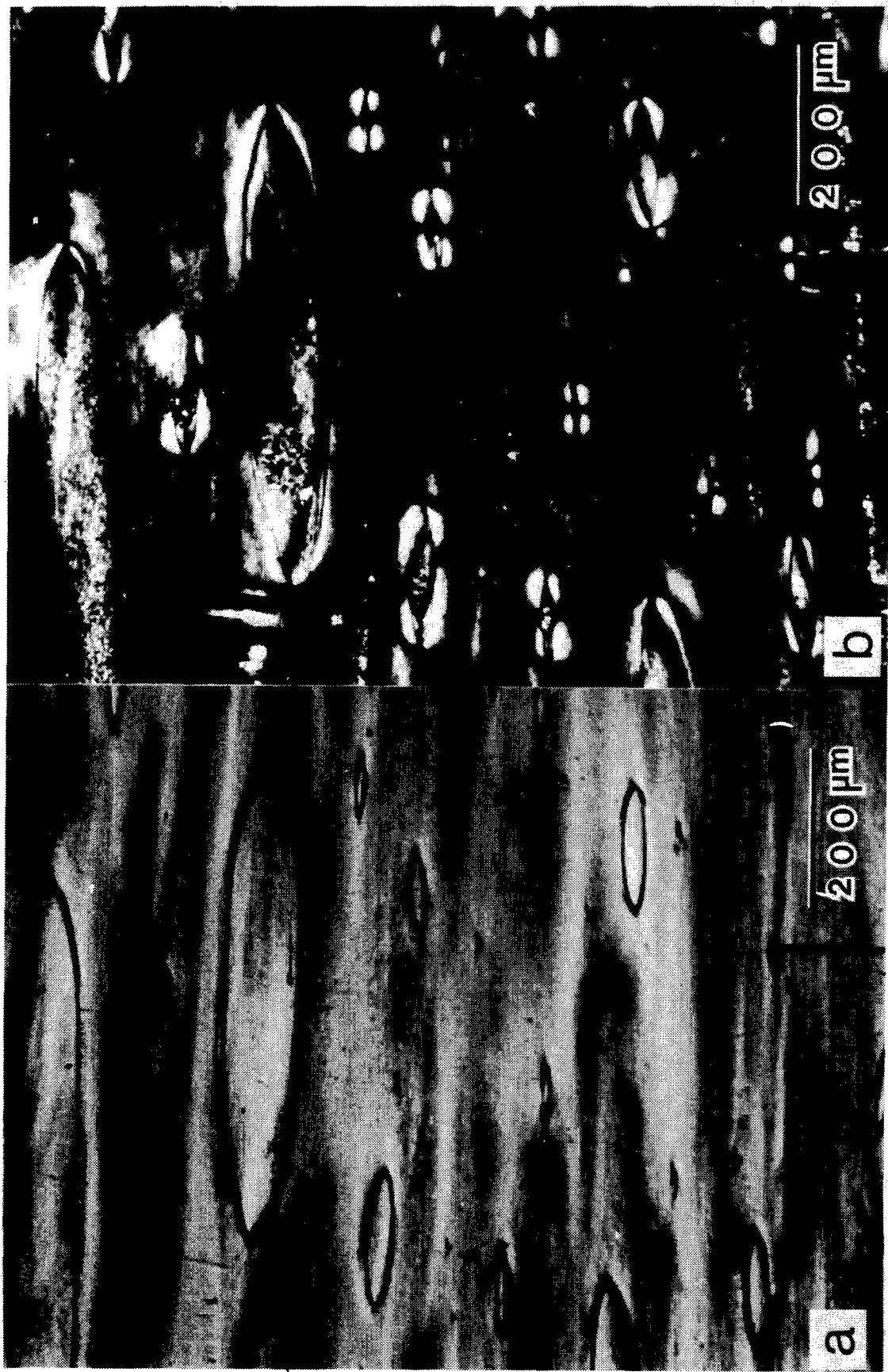


Figure 29. Polarized light micrograph of PBT-29022-7-8. (a) Film oriented at 45° to polarizer; (b) Film oriented at 5° to polarizer.



Figure 30. Polarized light micrograph of PBT-29022-5a. (a) Film oriented at  $45^\circ$  to polarizer; (b) Film oriented at  $0^\circ$  to polarizer.

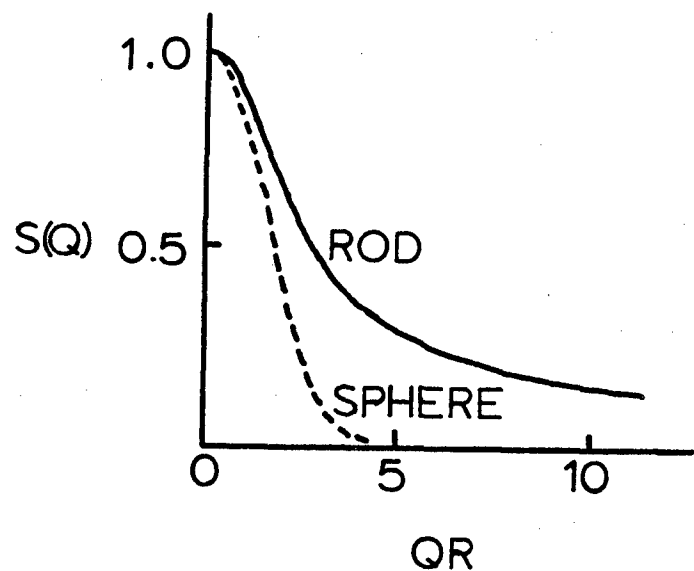


Figure 31. Scattering functions for a rod and a sphere.

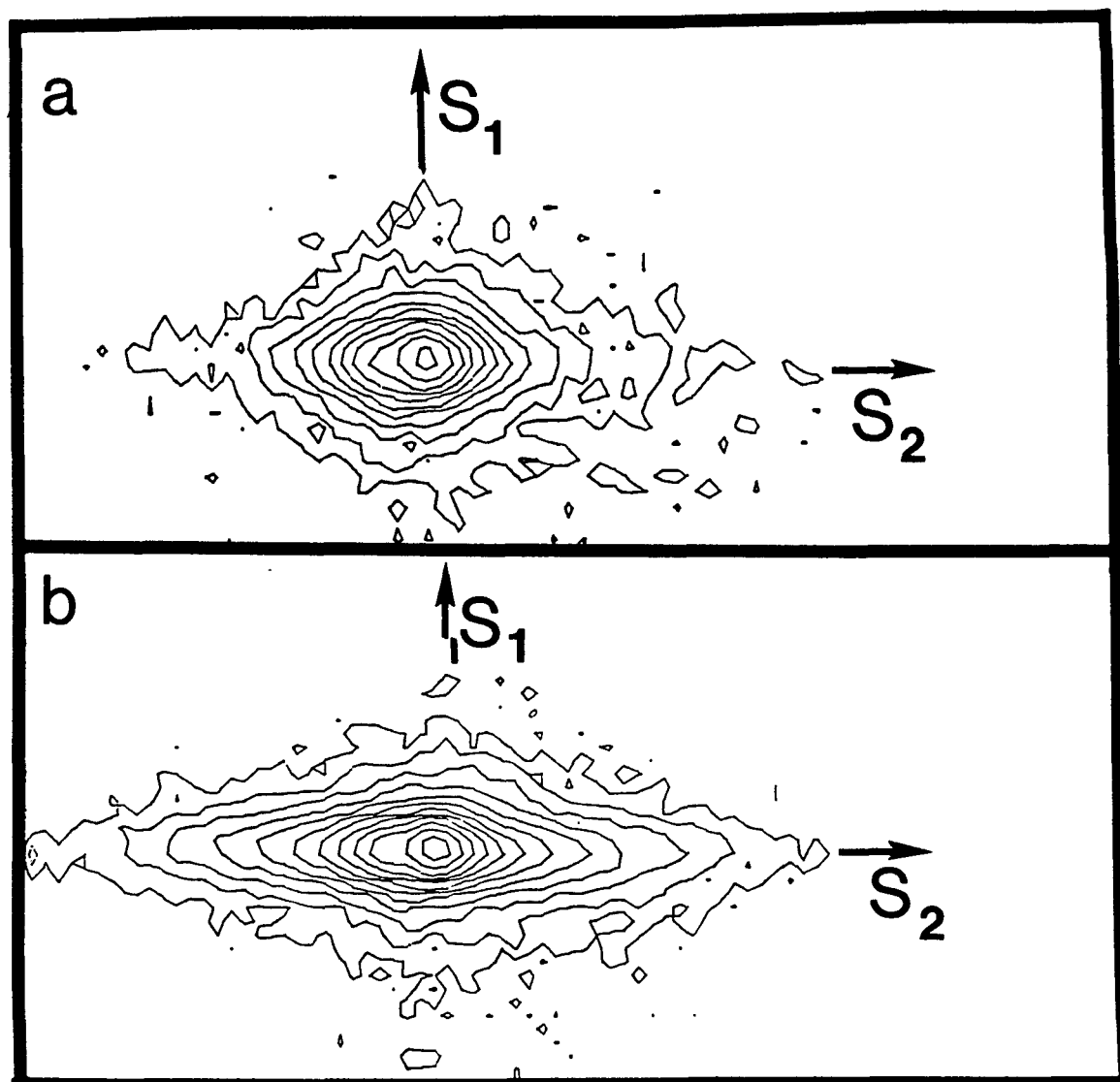


Figure 32. SAXS from annealed PBT fibers.

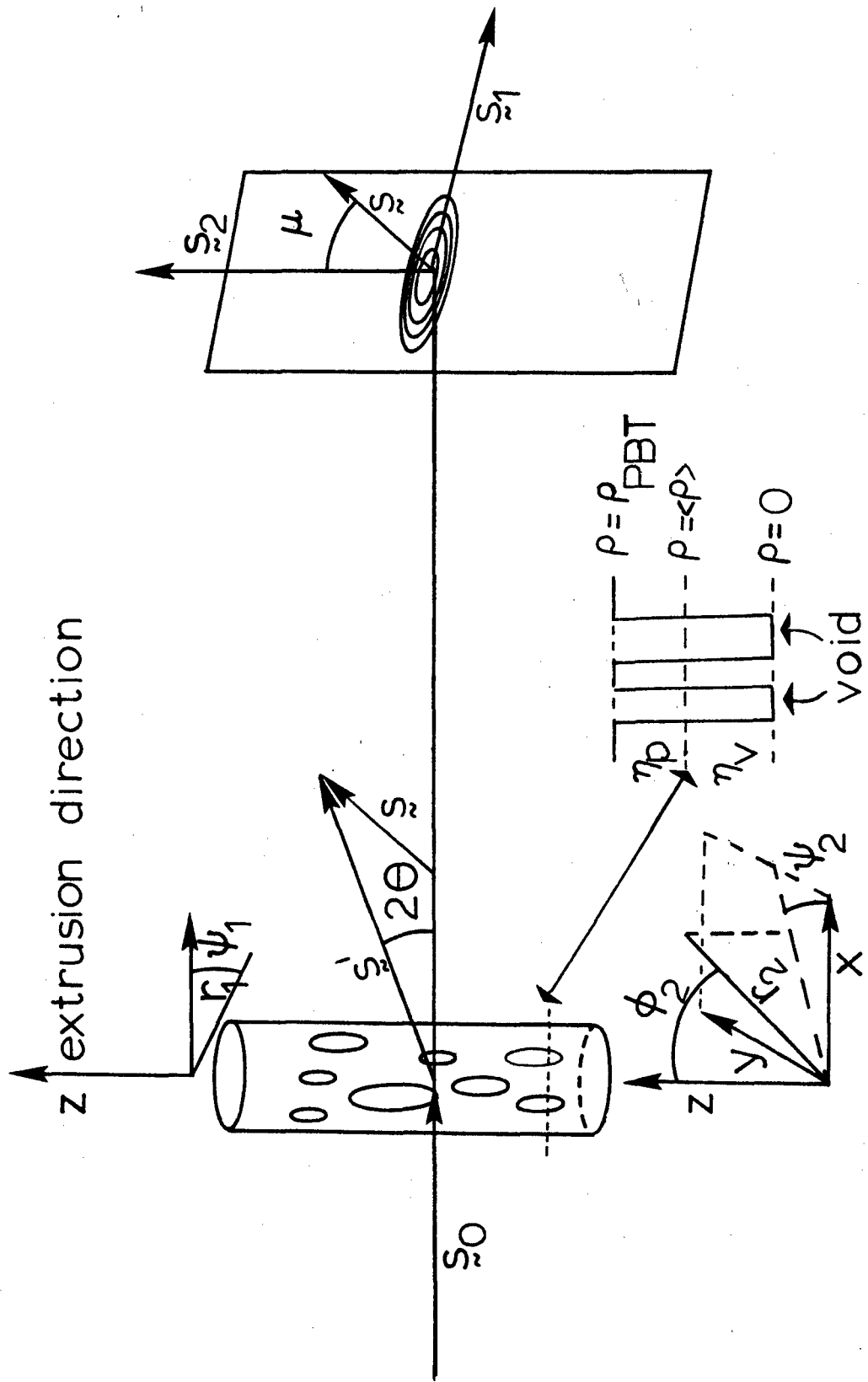


Figure 33. Model for interpreting SAXS from PBT.

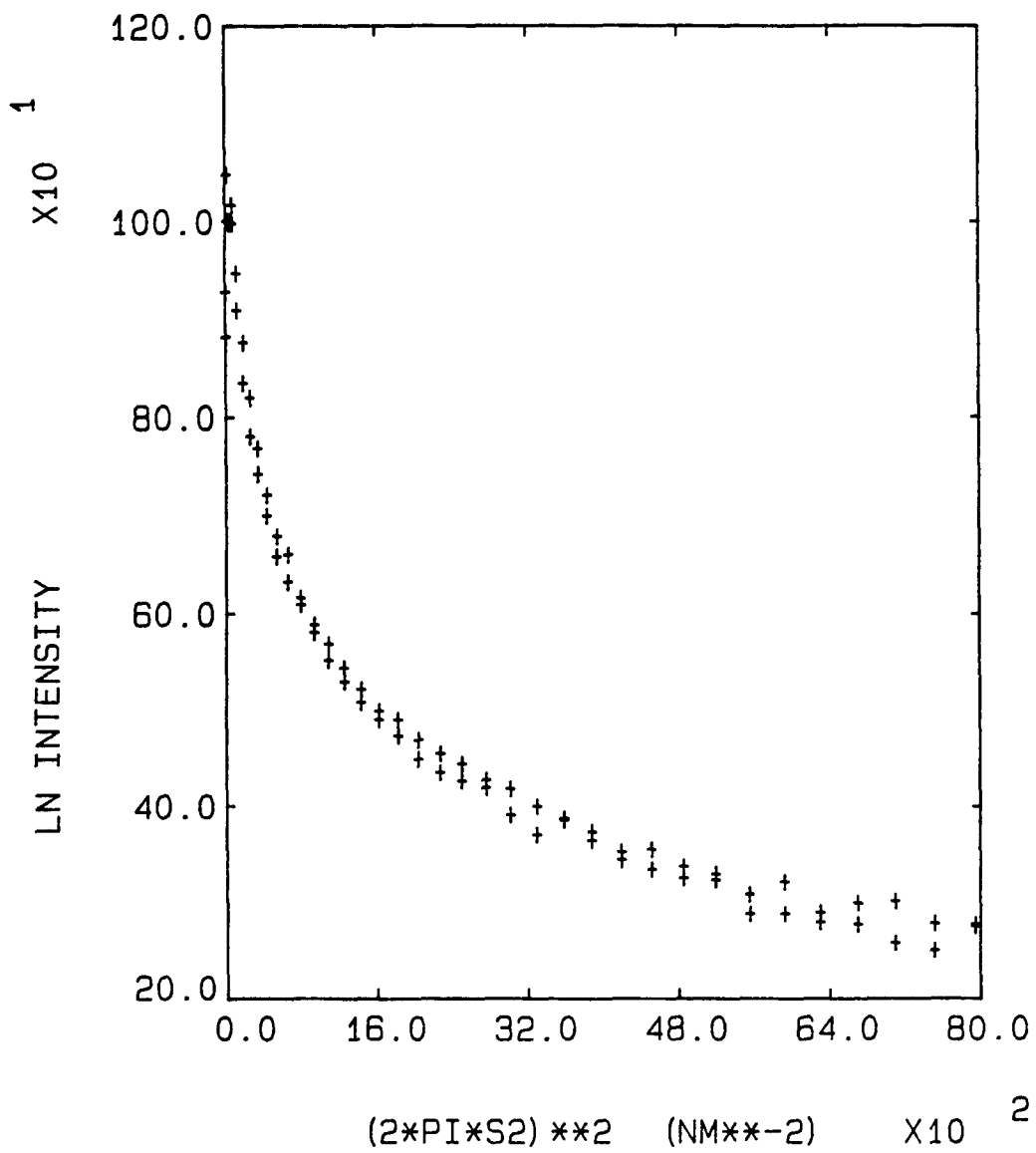


Figure 34. Guinier plot of PBT equatorial small angle x-ray scattering.

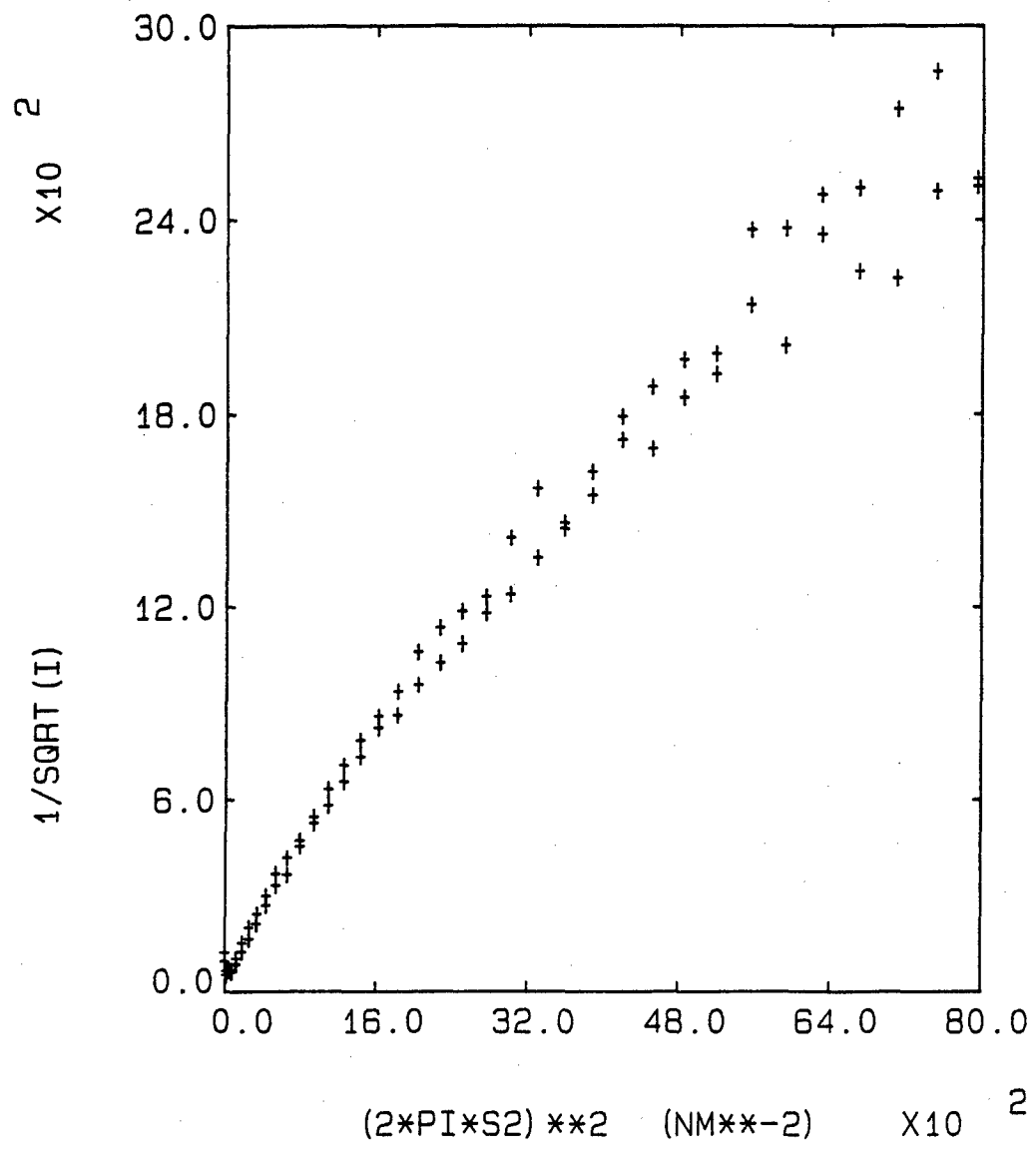


Figure 35. Debye plot of PBT equatorial small angle x-ray scattering.

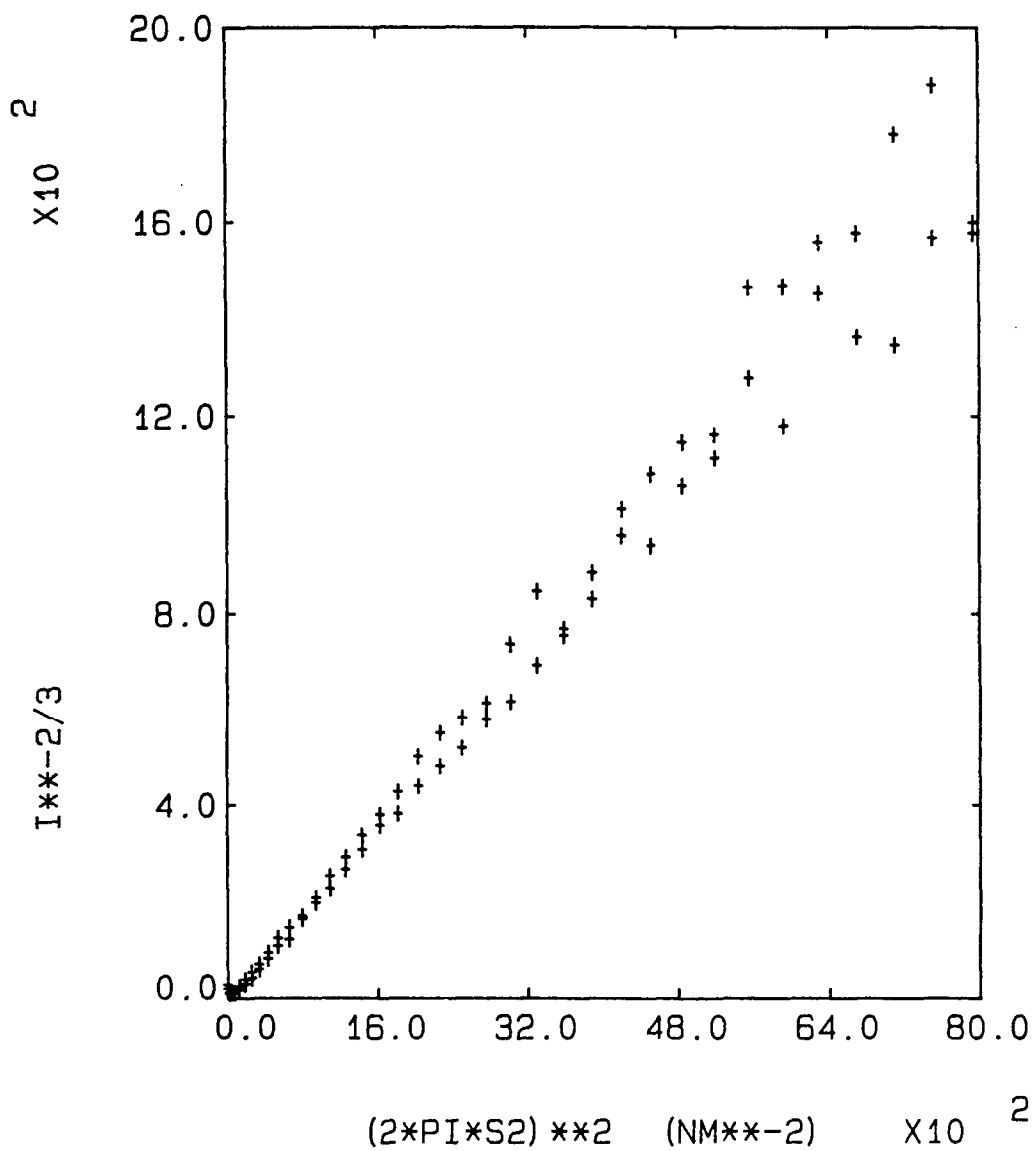


Figure 36. Cylindrical correlation function for PBT SAXS.

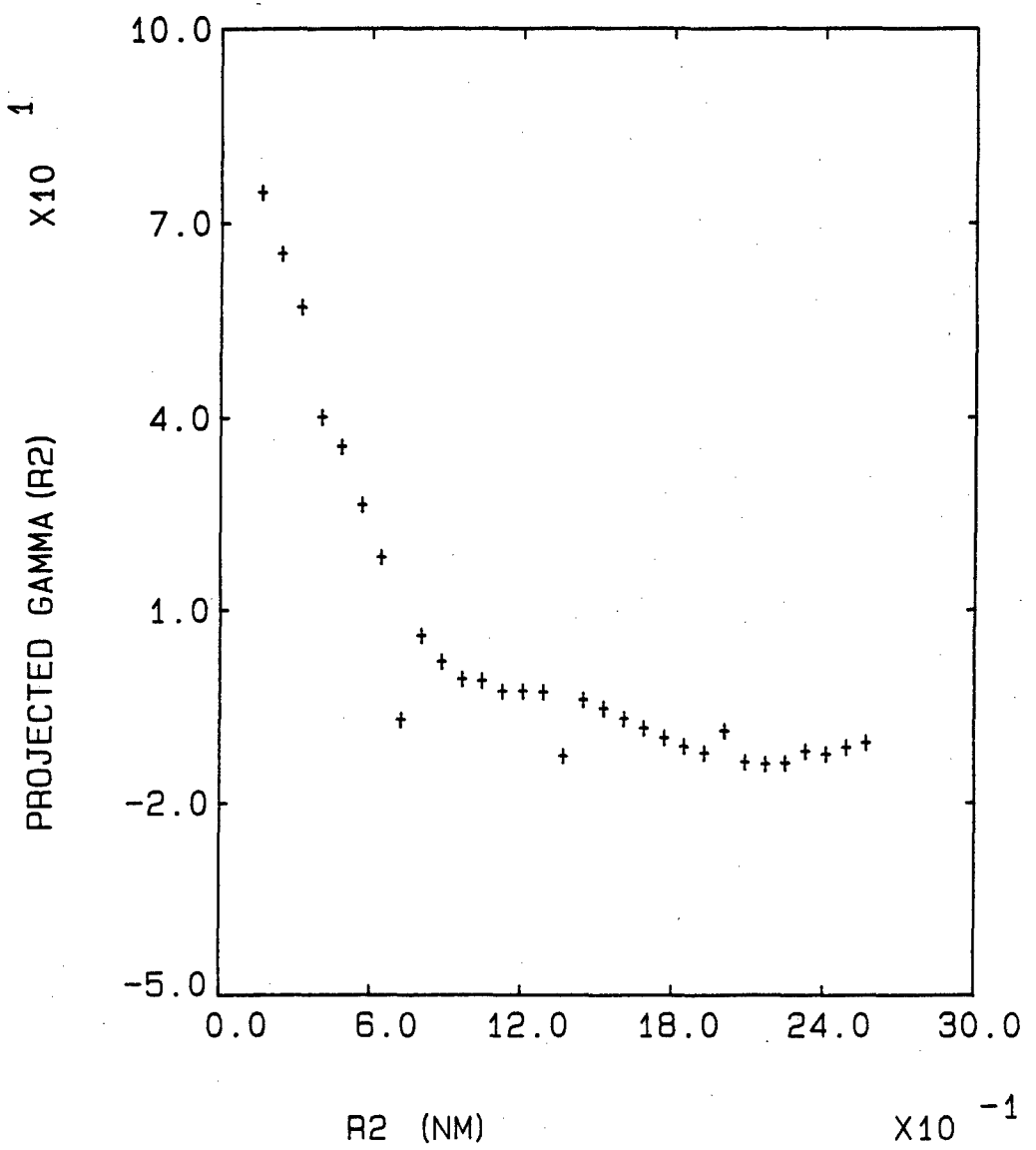


Figure 37. Projected correlation function along  $R_2$ .

#### SECTION IV: MECHANICAL PROPERTIES OF PBT FIBERS

The mechanical properties of PBT fibers spun from both methane sulfonic acid and polyphosphoric acid have been investigated with particular attention being given to property changes with heat treatment and to the mechanical anisotropy exhibited by the fibers. Fiber heat treatment studies (Section A) indicate the importance of high temperatures (500-600°C) in obtaining high strengths whereas high moduli can be obtained under a much broader range of conditions. A good retention of high modulus and high strength at elevated temperatures has been observed from a series of experiments (Section B) conducted in the temperature range of -200°C to +600°C.

Mechanical anisotropy in PBT fibers has been studied through torsional and bending experiments. The fiber shear modulus is observed to be two orders of magnitude lower than the tensile modulus (Section C) and the shear strength one order of magnitude lower than the tensile strength (Section D) indicating a high degree of anisotropy resulting from the axial alignment of the rod-like PBT molecules. In combined torsion and tension experiments (Section E), fiber tensile strength is retained up to moderate degrees of twisting. The anisotropy between tensile and compressive fiber behavior is also reported based on various fiber bending experiments (Sections F and G).

##### A. Fiber Heat Treatment

In attempting to understand the relationships between mechanical properties and microstructures in PBT fibers, it is advantageous to examine a number

of samples with differing properties. Use of a post-spinning heat treatment of as-spun PBT fibers can be employed to induce changes in both morphology and mechanical behavior which allows the study of a range of properties and structural characteristics in these fibers. Additionally, the investigation of the heat treatment process itself and its effect on fiber characteristics is invaluable to the tailoring of fiber properties for specific purposes.

A small scale heat treatment apparatus, schematically illustrated in Figure 38, has been employed for the heat treatment of as-spun PBT fibers. The process parameters include temperature, atmosphere, residence time and tension. Heat treatment temperature is controlled by passing the selected atmosphere (usually nitrogen) through tubing wrapped around the fiber chamber prior to entering it, both tubing and chamber being placed in a tubular oven capable of temperatures in excess of 1000°C. Thirty-five possible residence times are available by means of the take-up spool which is attached to a multiratio gear motor and a ten speed transmission. Residence times of 2.3 seconds to 27 minutes are accessible with the present equipment. A dynamometer connected to the fiber supply spool allows for careful measurement and control of the applied tension.

Due to the design of the tubular oven and the nitrogen flow pattern, it was desirable to measure the temperature distribution along the length of the fiber chamber and calculate an appropriate average heat treatment temperature. A typical temperature profile is given in Figure 39 for an average end temperature of around 400°C. The observed profile has a maximum center temperature as much as 150°C higher than the end temperatures. Certainly such severe profiles are undesirable for any quantitative study of heat treatment and a modified heat

treatment chamber is currently under construction. Therefore, the interpretation of our present heat treatment results are more qualitative than quantitative. It is hoped that when more quantitative results are obtained (with a more uniform temperature profile) and a better understanding of the heat treatment parameters is achieved, these results can be analyzed more precisely.

In order to obtain some useful information from the existing results we will apply certain corrections to the calculated residence times and average temperatures which would normally be reported. From Figure 39 it is observed that the temperature gradients near the oven ends are very severe. However, if only the central two-thirds of the oven are examined it is seen that the range of temperatures is reduced by roughly one-half (i.e. 70-80°C instead of 150°C). The average temperature over the central two-thirds of the oven for the profile of Figure 39 is 515°C with a maximum temperature of only 30°C higher over this distance. We will therefore consider only the central two-thirds of the oven as the "effective heat treatment chamber" for the presentation and discussion of our results. The residence times and average temperatures reported for the heat treatment of as-spun PBT yarns will therefore be based on this effective chamber length. It will be interesting to compare results obtained with this oven to results from a more homogeneous temperature profile. Temperature gradients would reduce the initial thermal shock to the fiber which may or may not be beneficial for PBT fibers.

Heat treatment of 5 filament PBT yarn 27554-33-5-255 was carried out using the apparatus described above. The as-spun mechanical properties of this fiber are: strength 9.5 gpd and modulus 1200 gpd. This fiber has also been heat

treated by Celanese. The Celanese heat treatment conditions were 475°C, 32 seconds, 1% stretch with the heat treated fiber being designated as 27554-42-2. The mechanical properties of this Celanese heat treated fiber are: strength 13.5 gpd, modulus 1800 gpd. It will be seen that this fiber has properties comparable to the properties reported below for similar heat treatment conditions.

Figures 40 and 41 present the modulus and strength of fibers heat treated for 77 seconds at 430°C, 515°C and 595°C as a function of the applied heat treatment tension per filament. All moduli and strength data are based on the as-spun fiber denier and are the averages of twelve tensile tests. From Figure 40 it is seen that the applied tension has an effect on the resulting modulus, whereas no effect of tension on strength is observed in Figure 41. It should be mentioned, however, that the condition of zero applied tension during heat treatment was not investigated in these studies.

It is obvious from both Figures 40 and 41 that the heat treatment at 595°C (for the 77 second residence time) was detrimental to the fiber mechanical properties. However, the heat treatments summarized in these two figures were performed without a cooling chamber for the fiber exiting the oven. In other words, the hot PBT yarn exiting the oven was simply exposed to room atmosphere where possible degradation may occur. In fact, for the 595°C case, it was observed that the yarn breakage occurred at the oven exit when the tension was increased. For these reasons a nitrogen cooled chamber was added to the oven exit to cool the hot yarn in an inert atmosphere before finally exiting into air.

Figures 42 and 43 present heat treated fiber properties for the same yarn heat treated at 595°C, with the use of a nitrogen aftercooler for a number of

residence times. A comparison of the results at the 77 second residence time with the data of the two previous figures indicates the beneficial influence of the cooling chamber. From these figures it appears that the applied tension is not nearly as influential as the residence time or temperature.

These results indicate that the higher the temperature during heat treatment, the higher the resulting fiber strength. However, the residence time is equally important and the fiber can only survive short exposure times at the high temperatures. Additional heat treatments employing various residence times at other temperatures are still needed to optimize the process as well as the heat treatment of different denier fibers. Higher values of moduli are reported here for the 430°C and 515°C heat treatments than for the 595°C heat treatments; however, only one residence time was investigated for the two lower temperatures.

Moduli of up to 1800 gpd (50% improvement) and strengths of up to 16 gpd (68% improvement) have been obtained for the heat treated PBT yarn reported here. As mentioned previously, these numbers are based on the as-spun fiber denier. If, however, we assume a similar weight loss as was found for the Celanese heat treatment of this fiber (we have also measured similar weight losses from heat treatment; e.g., monthly report, May 1980), these numbers can be multiplied by a factor of 1.1 for an additional 10% enhancement in properties. If we also consider the influence of the large voids present in this fiber, strengths comparable to those now being reported for PPA spun fibers are calculated, i.e. on the order of 20 gpd.

## B. Temperature Dependence of Tensile Properties

Tensile stress-strain response of a number of PBT fibers and of Kevlar fibers has been evaluated over the temperature range of -250°C to +250°C. The dependence of tensile modulus and strength on test temperature for these two materials are similar, both exhibiting a good retention of room temperature properties over a wide range of temperature. Some additional tests have been done at temperature as low as -198°C and as high as 595°C on some fibers and these results are also included here.

Five fibers were used in these tests: commercial Kevlar 49 and 29, as-spun PBT 27554-9-10, heat treated PBT 27554-42-2 and its precursor as-spun fiber, PBT 27554-33-5. All tests were performed using a 2.5%/min strain rate on 20 mm gage length samples prepared in the same manner as previously described [77]. Specimens were tested after a 5-10 minute conditioning period at the test temperatures of 25°C, 50°C, 100°C, 150°C, 200°C and 250°C. Tensile moduli values have been corrected for machine compliance evaluated at each test temperature.

Figure 41 summarizes the dependence of tensile modulus on test temperature for these five fibers. Over this temperature range fiber moduli are seen to decrease linearly with increasing temperatures. The heat treated PBT fiber (42-2) and the Kevlar fibers appear to have the same sensitivity to temperature while the as-spun PBT fibers (9-10 and 33-5) appear slightly more temperature sensitive. For comparison, at 200°C the heat treated PBT fiber modulus was 1500 g/denier, 82% of its room temperature value while the modulus of Kevlar 49 was 700 g/denier, 70% of its room temperature value.

The temperature sensitivity of fiber tensile strength however appears to be quite different for the Kevlar and PBT fibers as observed in Figure 45. Over

this temperature range fiber strength linearly decreases with increasing temperature, the rate of decrease being greater for Kevlar than for PBT. At 200°C the heat treated PBT fiber retained 73% of its room temperature strength while the Kevlar fiber strength retention was only 60-65%. The sensitivity of strength to temperature for the as-spun and heat treated PBT fibers appears to be the same.

Kevlar 49 fibers and the heat treated PBT fiber, 27554-42-2, were also tested at subambient temperatures. For these tests fiber samples were tested submerged in baths of liquid nitrogen at its boiling point (-196°C) and in dry ice/isopropanol baths (-70°C). The results of these experiments combined with the data of Figure 44 and 45 are presented in Figures 46 and 47. From Figure 46 the dependence of fiber moduli on temperature for the PBT and Kevlar 49 fibers is observed to be similar. While both fibers exhibited higher moduli at -70°C than at room temperature, the moduli at -196°C was found to be the same or even lower than the value at -70°C. Fiber strength (Figure 47) for the Kevlar 49 fibers was observed to be lower at subambient temperature whereas the PBT fiber exhibited a higher strength. At both -70°C and -196°C Kevlar 49 fibers exhibited a strength of 90% of its room temperature value. The modulus of the PBT fiber tested at -196°C was 1.4 times its room temperature value.

Additional fiber strength data has been obtained from the heat treatment experiments reported in the previous section. By increasing the tension applied to the yarn during heat treatment until fiber breakage occurs, an estimate of the strength of the fiber at the heat treatment temperature is obtained. It should be noted, however, that these results represent a test in a nitrogen

atmosphere. Additionally the preconditioning period is different, depending on the residence time employed for the heat treatment. It was observed that for the three heat treatment residence times employed, similar values of breakage stress were obtained. Figure 48 summarizes these results for as-spun PBT 27554-33-5 and compares them with heat treated PBT 27554-42-2. From this limited amount of data it appears that the strength of PBT fibers is roughly a linearly decreasing function of test temperature over the temperature range of 0°C to 600°C.

### C. Fiber Torsional Modulus

Knowledge of fiber torsional or shear modulus is of importance for the prediction of fiber behavior in woven structures and in complex stress states. Additionally, the shear modulus, when compared with the tensile modulus, provides a measure of material anisotropy. In this section the results of torsional vibration experiments, from which the torsional modulus can be obtained, are discussed for two Kevlar fibers, an as-spun PBT fiber (28555-50-3), a heat treated version of this same fiber (29022-1-12) and for a high modulus K-glass fiber.

The apparatus used in these studies is schematically illustrated in Figure 49. Fiber samples for these tests were prepared in the usual manner by bonding single filaments to cardboard tabs to facilitate gripping, a gage length of 20 mm being used for all fiber samples. One end of the fiber sample was then clamped in a fixed grip, the other end being carefully centered in a slotted disc pendulum as shown in the figure. The sides of the paper tab were then cut

away to free the fiber/disc system. Two different pendulum discs were employed having moments of inertia of 115 g-mm<sup>2</sup> and 56 g-mm<sup>2</sup> (which includes the minor contribution from the paper tab). The entire apparatus was then covered by a bell jar to prevent air currents.

The experiment consisted of imposing a 180 degree twist to the fiber sample and allowing the fiber/disc system to swing freely. The period of oscillation of the resulting motion was then measured with a stopwatch by following the motion of a reference mark on the disc relative to a similar mark on a platform mounted below the disc. It should be noted that these experiments were carried out at atmospheric pressure and while damping due to air resistance was observed for all fiber samples the amount of damping was not measured and therefore the moduli presented here are uncorrected for damping.

From measurements of the period of oscillation of the fiber/disc in these free torsional pendulum experiments, the fiber shear modulus was calculated through equation (70):

$$G = \frac{8\pi LI}{r^4 p^2} \quad (70)$$

where L is the fiber length, I the moment of inertia of the pendulum disc, r the fiber radius and p the period of oscillation. The shear moduli obtained for the five fibers investigated are presented in Table 9 along with the values of their tensile moduli for comparison. The PBT fibers possess shear moduli of roughly 1.4 GPa while the moduli of the Kevlar fibers is approximately 2 GPa.

A measure of material anisotropy is obtained from the ratio of tensile to

shear modulus ( $E/G$ ). For isotropic materials this ratio is equal to twice the value of one plus Poisson's ratio and should therefore have a value of between 2.0 and 3. From Table 9 it is seen that for the K-glass fiber the ratio  $E/G$  was calculated to be approximately 3, consistent for an isotropic material.  $E/G$  ratios for the PBT and Kevlar fibers range from 40 to 150 indicating a high degree of mechanical anisotropy. For comparison the  $E/G$  of wood (Douglas Fir) is approximately 16. These large values of  $E/G$  found for the PBT and Kevlar fibers obviously derive from the very high level of molecular orientation with respect to the fiber direction. In tensile experiments the modulus ( $E$ ) measures the response to deformation of chemical bonding in the chain direction; whereas in the torsional experiments the weaker secondary interactions between chains are largely responsible for the observed properties.

The large difference between the  $E/G$  ratio for the as-spun and heat treated PBT fibers results from their having approximately the same shear modulus (1.4 GPa) while possessing widely different tensile moduli, that of the heat treated fiber being twice that of the as-spun fiber. It should be pointed out, however, that both of these fibers possess roughly the same tensile strength (1.8 GPa).

#### D. Large Torsional Deformation: Twisting

The behavior of a heat treated PBT fiber (29022-1-12) in twisting was determined using an apparatus similar to that shown in Figure 49. In these experiments large torsional strains were imposed on the fiber sample by twisting the lower pendulum. The elastic component of this imposed shear strain was then measured by the amount of reversible twisting. As in the torsional modulus

experiments, samples of 20 mm gage length were bonded onto paper tabs.

The elastic torsional response of PBT fiber to large torsional strains (strains refer to the outer surface of the fiber) is summarized in Figure 50. The dashed line in the figure indicates the behavior of an ideally elastic material, i.e., the whole strain being completely reversible. For shear strains below 5%, the PBT fiber behaves elastically. Above 5% shear strain, a large amount of the imposed twist is irreversible. The ability of PBT fibers to sustain large torsional strains without complete fiber failure is in contrast to their brittle behavior in tension, again indicating the high degree of anisotropy present in these fibers.

To understand the nature of the irreversible torsional behavior at high degrees of twist, fiber samples having been twisted various amounts (and then fixed) were observed in a scanning electron microscope. Figure 51 shows the appearance of the fiber surface after 5%, 10%, 20% and 40% surface shear strain. In the range of elastic torsional behavior ( $\gamma < 5\%$ ) the fiber surface appears unaltered from that of an untwisted sample. Above 5% surface shear strain, however, the appearance of cracks running longitudinally down the fiber is observed. The severity and number of these cracks is seen to increase with increasing torsional strain and at large torsional strains, the cracks run helically about the fiber axis.

If the fiber behavior in torsion is assumed to be linear elastic in the reversible range of twisting ( $\gamma < 5\%$ , Figure 50) an estimate of the shear strength of the fiber can be made. From the previous section this particular fiber was found to possess a shear modulus of 1.3 GPa as measured from free

torsional vibration experiments. Taking 5% surface shear strain as the limit of reversible behavior in twisting, the shear strength of the surface layers of the fiber at the onset of longitudinal cracking is approximately 65 MPa.

#### E. Torsion-Tension Testing

The effect of pretwisting on the tensile strength of PBT fiber (29022-1-12) has been investigated. In these experiments, normal 20 mm gage length tensile samples were twisted as described in section D and while maintaining the twist were placed in an Instron for tensile testing. Figure 52 summarizes these experiments as the ratio of tensile strength of the twisted fiber to normal tensile strength ( $\gamma=0$ ) as a function of the amount of pretwisting. The tensile strength of the PBT fiber is seen to be unaffected by pretwisting of up to 10% surface shear strain. Above 10% surface shear strain, the tensile strength falls off drastically and appears to level off above 20% shear strain. For this particular fiber, then, a shear strain of 10% measured at the fiber surface can be considered as a limit of safe twisting.

It is interesting to note that shear strains of up to 10% do not adversely affect the tensile strength while from the previous section it was observed that shear strains just greater than 5% produced longitudinal cracks in this same fiber. In the 1980 yearly report, for a different PBT fiber (27554-42-2), a 5% shear strain also produced irreversible twisting behavior yet that fiber maintained a high tensile strength up to 25% shear strain pretwisting. Additional torsion-tension and twisting-testing are therefore required on a number of fiber samples to explore differences in fiber behavior and to correlate these differences with structural and processing differences.

It has also been noted in some preliminary experiments that if the reversible component of the pretwisting strain is allowed to relax before tensile testing higher tensile strengths are measured. Such combined states of loading should therefore provide useful information regarding the failure mechanisms in PBT fibers and will be further investigated.

#### F. Mandrel Loop Tests

Loop strength experiments similar to those previously reported [77] have been carried out on PBT 29022-1-12 fiber. The geometry of these tests is illustrated in Figure 53 along with the loop strength behavior of this fiber. These experiments simply measure the loop strength of the fiber placed around mandrels of various diameters, with a fiber wrapped around another fiber being the most severe bending case. For brittle, linear elastic materials that fail in tension, the expected loop strength is given by equation (71):

$$\sigma = E(\epsilon_b - \frac{r}{r+R}) \quad (71)$$

where  $\sigma$  is the loop strength,  $E$  the fiber modulus,  $\epsilon_b$  is the strain at break in tension,  $r$  the fiber radius and  $R$  the mandrel radius. Equation (71) predicts that the measured loop strength of the fiber is less than the tensile strength by an amount equal to the bending contribution to the axial stress. Figure 53 indicates that the loop strength of this PBT fiber is greater than that predicted by equation (71) and is even finite for an apparent bending strain of 50% (fiber looped over another fiber). The discrepancy between predicted and observed loop behavior is the result of the compressive strength being lower

than the tensile strength of the fiber. Scanning electron microscopy studies reveal the formation of kinks in the regions of compressive stresses in bent fibers (see figure 56). When compressive failure occurs in the loop, a redistribution of the bending strain field within the looped fiber cross-section results. The effective fiber diameter for bending is reduced, lowering the maximum bending strains giving higher than expected loop strengths.

The mandrel loop experiments on PBT fibers have revealed the anisotropy of material behavior in compression compared with tension. However, these experiments do not provide a quantitative measure of PBT fiber compressive behavior and additional types of tests are required.

#### G. Elastica Loop Tests

To begin to characterize the bending and compressive behavior of PBT, fibers were subjected to the elastica loop test illustrated in Figure 54. In these experiments, fiber loops were placed in parafin oil between glass slides and observed under an optical microscope. The loops were drawn down by pulling on the fiber ends and micrographs were taken at successive intervals from which loop geometry and bending strains could be calculated.

Characteristics of the elastica loop test have been worked out by Sinclair [78] for an ideally elastic material. However, in his analysis, Sinclair did not consider any possible curvature contributions due to shear and material anisotropy. For example, in a simple cantilever beam experiment the deflection of the end of the beam due to shear is dependent on beam geometry and on the ratio of E/G. The ratio E/G for isotropic materials is in the range of 2 to 3, whereas that for PBT fibers, it can be as high as 150 (section C),

therefore, the shear contribution to deflection of the cantilever can be up to two orders of magnitude greater for an anisotropic material than for an isotropic material. It was therefore considered worthwhile to examine the effect of shear and material anisotropy on the elastica loop behavior for the PBT fiber experiments.

The approach to the elastica test which we will consider is based on equating the elastic strain energy in an element of the elastica with the work done in producing the elastica. The elastic stored energy can be expressed as:

$$U = \frac{1}{2} \iiint \sigma_{ij} \epsilon_{ij} dv \quad (72)$$

where  $\sigma_{ij}$  and  $\epsilon_{ij}$  are the corresponding components of the stress and strain tensors respectively (summation convention implied) and  $dv$  is a volumetric element. For the problem of the elastica only the axial stresses ( $\sigma$ ) and shear stresses ( $\tau$ ) produced in bending are considered. Equation (72) can then be written as:

$$U = \frac{1}{2} \iiint_v (\sigma^2/E + \tau^2/G) dv \quad (73)$$

The volume integral can be decomposed into an integral over the cross-sectional area and over an arc length ( $ds$ ). Assuming a circular cross-section and the corresponding stress distributions produced in bending the integration over the fiber cross-section yields:

$$U = \frac{1}{2} \int_s \left( \frac{EI}{R^2} + \frac{4V^2}{3AG} \right) ds \quad (74)$$

where  $E$  is the fiber axial modulus,  $R$  the radius of curvature,  $I$  the moment of

inertia of the cross-section,  $V$  the shear force on the cross section,  $A$  the cross-sectional area and  $G$  is the fiber shear modulus.

The work done in bending to produce the elastica is given by:

$$W = \frac{1}{2} \int_s \frac{M}{R} ds \quad (75)$$

where  $M$  is the bending moment. Equating expressions (74) and (75) yields:

$$\int_s \left( \frac{M}{R} - \frac{EI}{R^2} - \frac{4V^2}{3AG} \right) ds = 0 \quad (76)$$

Considering any element of arc length the expression under the integral sign in equation (76) must therefore be equal to zero and equation (76) reduces to:

$$\frac{M}{R} = \frac{EI}{R^2} + \frac{4V^2}{3AG} \quad (77)$$

If we neglect the effect due to shear, equation (77) reduces to the normal bending equation:

$$M = \frac{EI}{R} \quad (78)$$

Referring to Figure 54, a moment balance about any point  $(x,y)$  yields:

$$M = T(s-y) \quad (79)$$

where  $T$  is the tension applied to the fiber ends to maintain the loop. From

geometry the shear force on the cross-section at  $(x,y)$  can be expressed as:

$$V = \frac{T \ dy/dx}{[1+(dy/dx)^2]^{1/2}} \quad (80)$$

and the radius of curvature can be written as:

$$\frac{1}{R} = \frac{d^2y/dx^2}{[1+(dy/dx)^2]^{3/2}} \quad (81)$$

Using equations (81), (80) and (79) the solution of equation (77) would yield an expression for the elastica,  $y = y(x)$ . Due to the difficulties involved in solving the non-linear differential equation, a simpler check on the magnitude of the shear energy term in equation (77) is first considered.

Consider the ratio of the energy term due to shear stresses ( $4V^2/3AG$ ), to that due to axial stress ( $EI/R^2$ ). Define  $\psi$  as the ratio of these two terms:

$$\psi \equiv \frac{4V^2R^2}{3AGEI} \quad (82)$$

The maximum value of  $V$  occurs at a position  $y = s-\phi$  where  $dy/dx = \infty$ . The radius of curvature at this location can be approximated from the solution of equation (28) (neglecting shear) as:

$$\frac{1}{R} \approx \frac{M}{EI} = \frac{T\phi}{EI} \quad (83)$$

Therefore at  $y = s - \phi$ ,  $\psi$  takes on the value:

$$\psi = \frac{4EI}{3AG\phi^2} = \frac{E}{G} \left( \frac{r^2}{3\phi^2} \right) \quad (84)$$

where  $r$  is the fiber radius. As mentioned earlier, the importance of the shear energy term increases for anisotropic materials where the ratio  $E/G$  can take on large values.

The value of  $\phi$  can be estimated from the solution of equation (88) which can be shown yields:

$$\phi = s/2. \quad (85)$$

The magnitude of  $\psi$  can now be estimated taking typical values for the fiber size and elastica geometry. The radius of the PBT fiber used for these tests was 0.012 mm and a typical value of  $s$  would be on the order of 10 mm. Using an  $E/G$  ratio of 150 (section C) equation (84) yields:

$$\psi \approx 1 \times 10^{-4} \quad (86)$$

Therefore it can be concluded that even though the shear energy term is two orders of magnitude larger for anisotropic PBT fibers than for an isotropic material it is still negligible ( $\sim 10^{-4}$ ) compared with the axial stress energy term and the solution of equation (88) can be used to describe the elastica loop for anisotropic PBT fibers.

Sinclair [77] has given the solution of equation (88) to be

$$X = \pm s \left( \frac{2y}{s} - \frac{y^2}{s^2} \right)^{1/2} \mp \frac{s}{4} \ln \frac{1+(2y/s-y^2/s^2)^{1/2}}{1-(2y/s-y^2/s^2)^{1/2}} \quad (87)$$

The analysis also yields the following useful results:

$$s^2 = \frac{4EI}{T} \quad (88)$$

$$R_{\min} = s/4$$

and (89)

$$D = 0.5328 s$$

where D is the minor axis of the loop (Figure 54). Sinclair did not mention but it can be derived from (87) that the major loop axis (L) has the value

$$L = 0.7136 s \quad (90)$$

From (89) and (90) then it is observed that if the fiber behaves elastically in the elastica loop geometry, the ratio of major to minor loop axis should be equal to a constant,

$$L/D = 1.34 \quad (91)$$

The elastica loop test therefore provides a simple means of studying the bending behavior of PBT fibers. By drawing loops down to smaller values of L (or D) and hence increasing the bending strains in the loop, the parameter L/D can be

followed to monitor the elastic region of fiber behavior.

Figure 55 summarizes the elastica loop data obtained for PBT 29022-1-12 fiber. It is observed that as the bending strains are increased (decreasing the value of L) the ratio L/D remains constant until the major loop axis is on the order of 10 mm. For smaller values of L the ratio of L/D increases as the fiber deviates from elastic behavior. If the loop is undone after drawing down to  $L < 10$  mm the fiber possesses a permanent curvature indicating irreversible deformation has occurred. Scanning electron microscopy reveals the onset of kink formation (Figure 56) in the compressive stress regions of the fiber for 29022-1-12 fibers drawn down below  $L = 10$  mm.

The radius of curvature at the onset of non-linear behavior can be calculated from (86) or can be estimated from the micrographs taken just prior to the onset of kinking. Using an axial modulus of 200 GPa for the fiber, a compressive stress of 0.68 GPa is calculated for the onset of kink formation. Experiments carried out on Kevlar 49 fibers yield a similar value of 0.74 GPa for the onset of compressive yielding in bending. The compressive strength of PBT fiber is roughly 30% of its tensile strength indicating the degree of anisotropy between tensile and compressive behavior.

#### H. PBT Compressive Behavior

The effect of compression on the morphology and mechanical properties of PBT fiber surface can be examined by embedding the fiber in a polymer matrix which subsequently undergoes shrinkage. The compressed fiber is easily recovered by dissolving away the matrix material with an appropriate solvent.

Surface morphology of the compressed fiber can then be examined using SEM techniques. Changes in the mechanical behavior will be determined with tensile testing of the compressed fiber, and will be reported in a future report.

Table 9  
Comparison of Tensile and Torsional Moduli

	E (GPa)	G (GPa)	E/G
Kevlar 29	89	2.2	40
Kevlar 49	130	1.8	72
PBT 50-3	93	1.4	66
PBT 1-12	200	1.3	154
K Glass	67	22	3

- A Tubular Oven
- B Coiled Tubing for Preheating Nitrogen
- C Fiber Chamber
- D Aftercooler
- E Fiber
- F Fiber Take-up Spool/Multiratio Gear Motor
- G Fiber Supply Spool/Dynamometer
- H Nitrogen Supply

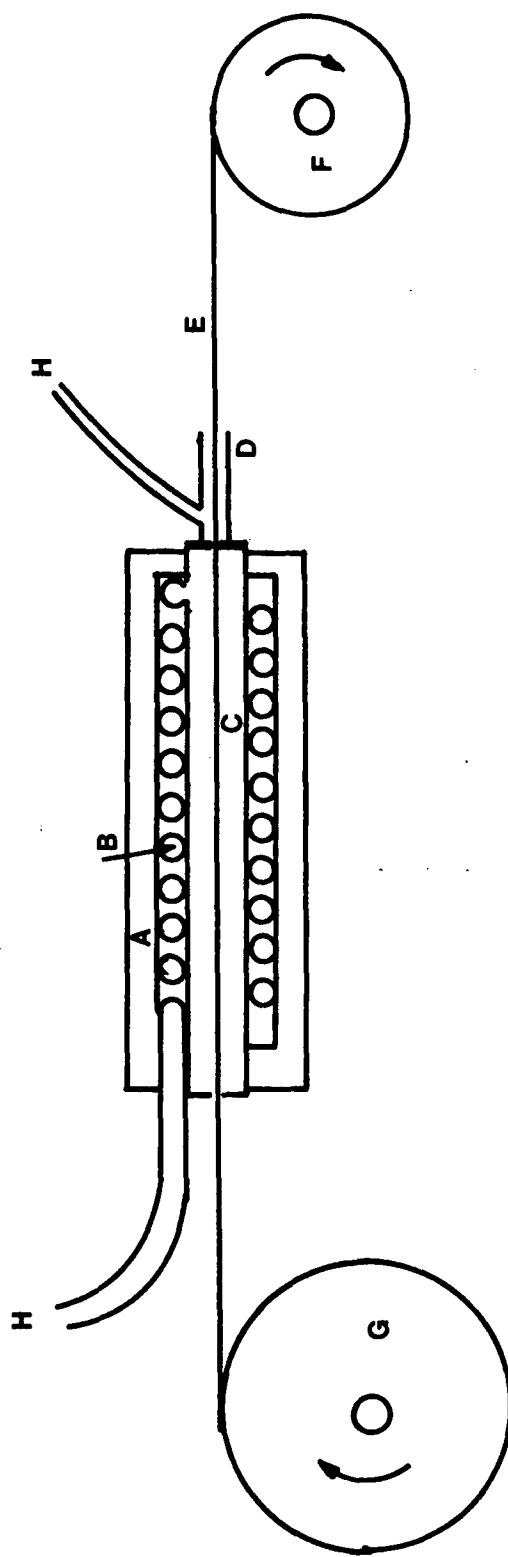


Figure 38. Schematic of fiber heat treatment apparatus.

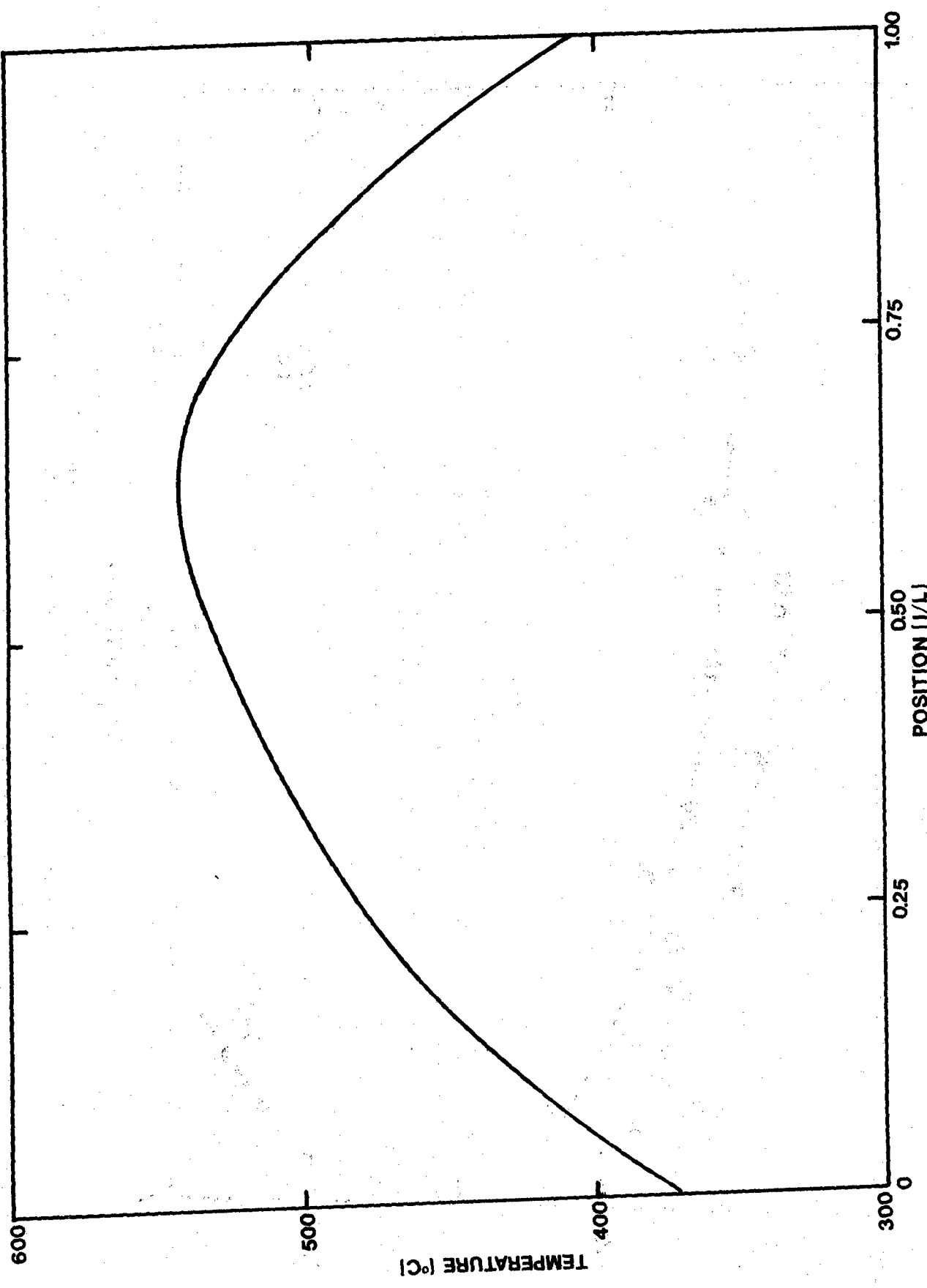


Figure 39. Typical temperature profile in the heat treatment chamber.

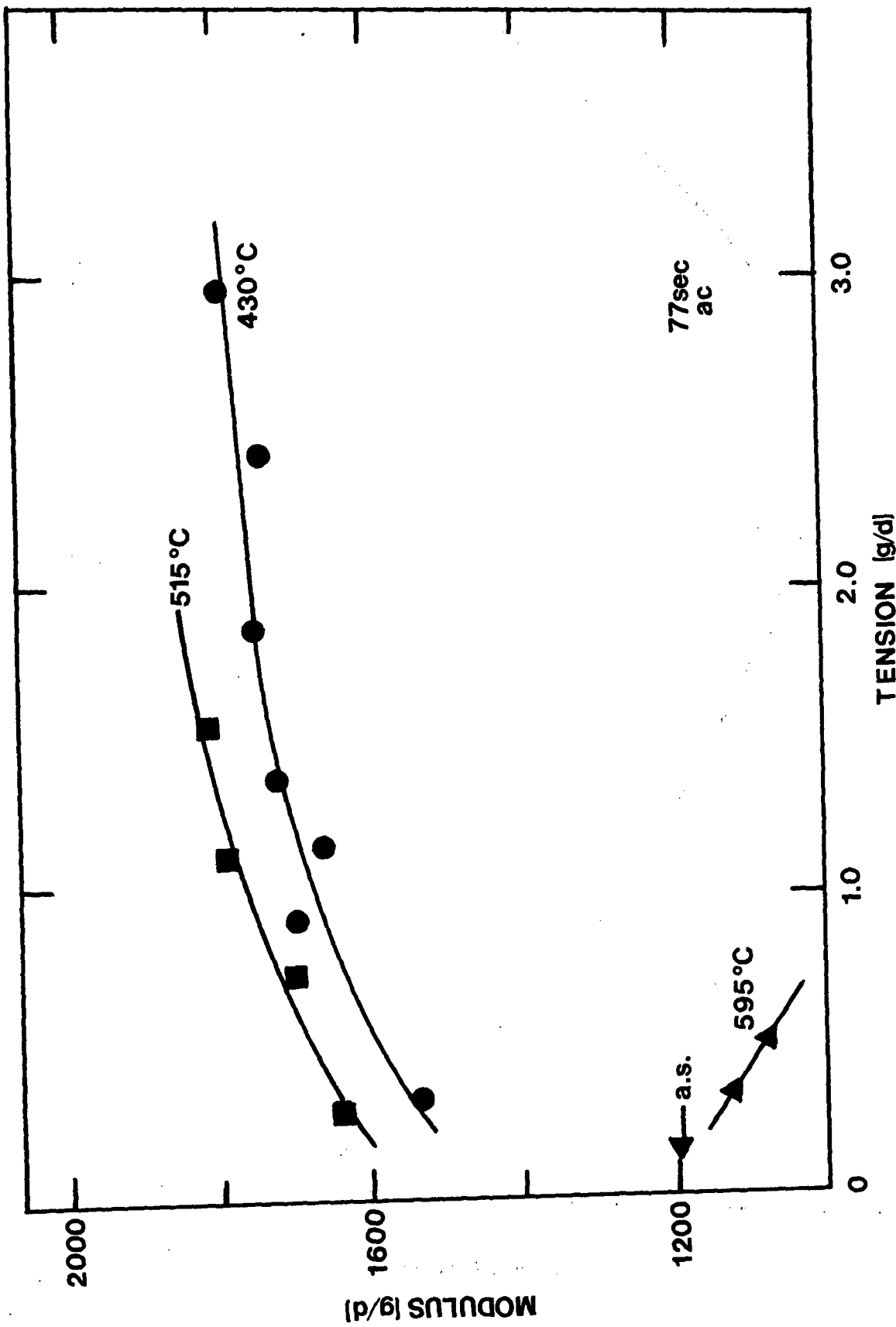


Figure 40. Summary of heat treated fiber modulus dependence on heat treatment temperature and tension. Residence time 77 seconds, no aftercooler.

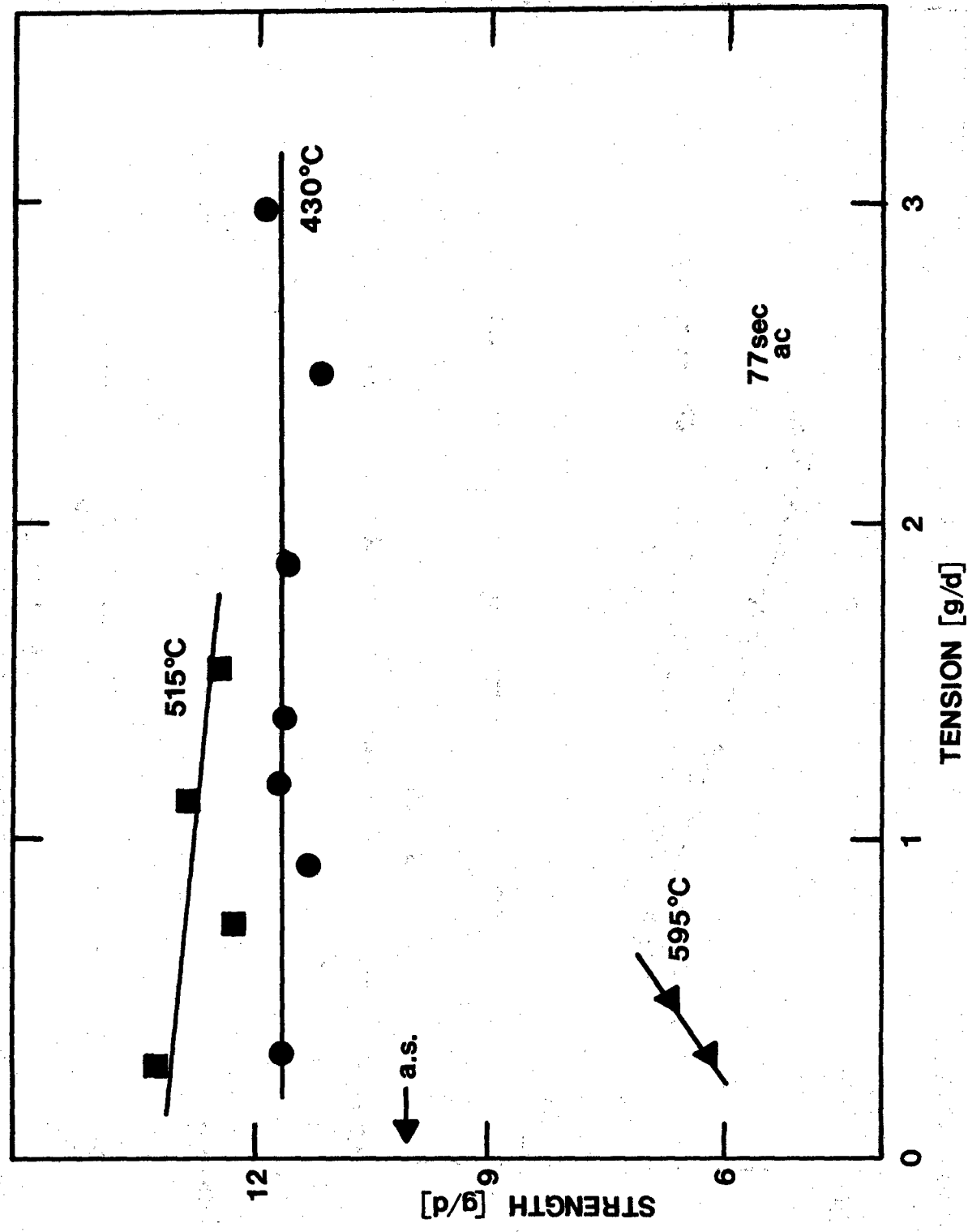


Figure 41. Summary of heat treated fiber strength dependence on heat treatment temperature and tension. Residence time 77 seconds, no aftercooler.

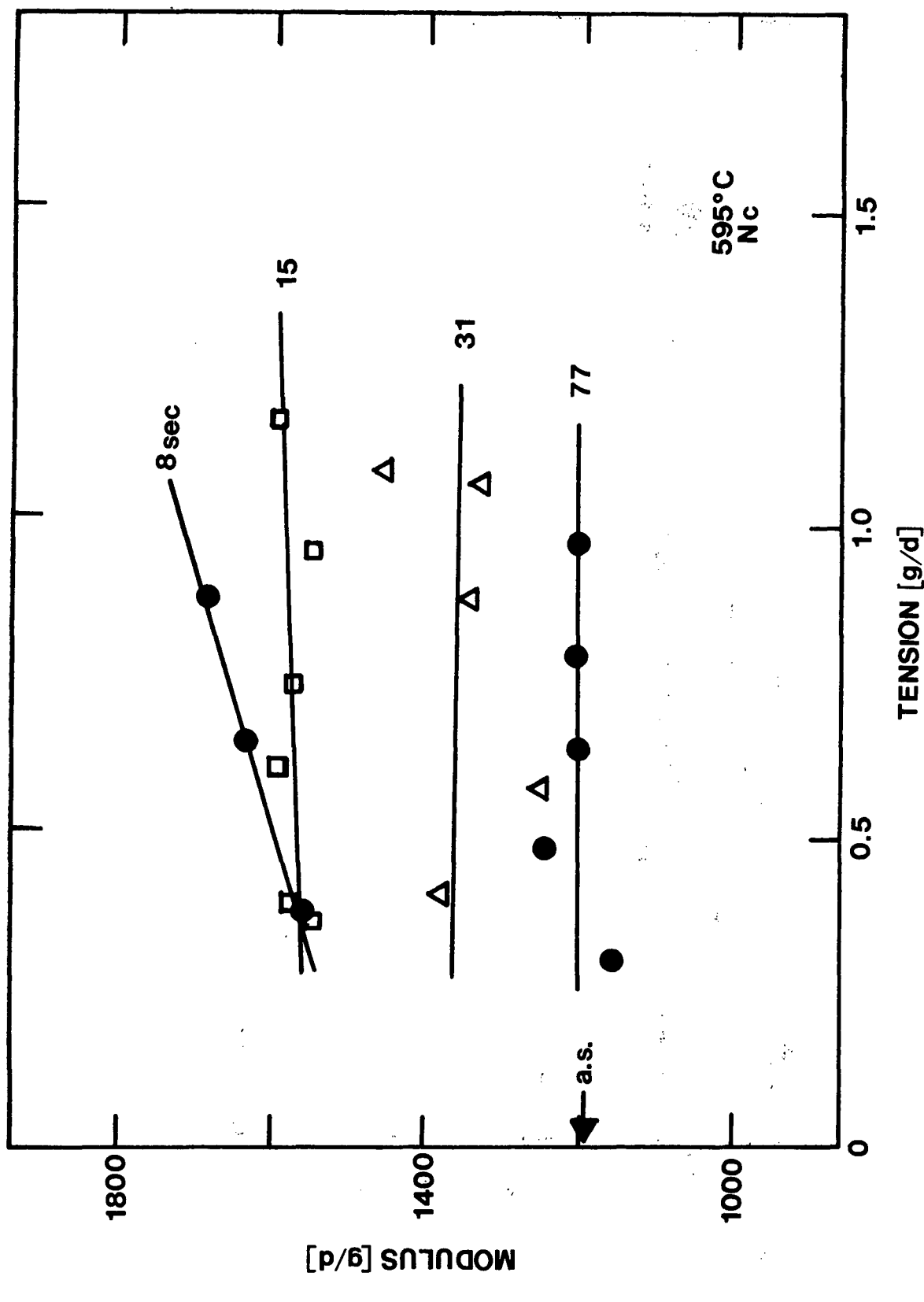


Figure 42. Modulus, of  $595^{\circ}\text{C}$  heat treated fiber, dependence on residence time and tension. Nitrogen aftercooler used.

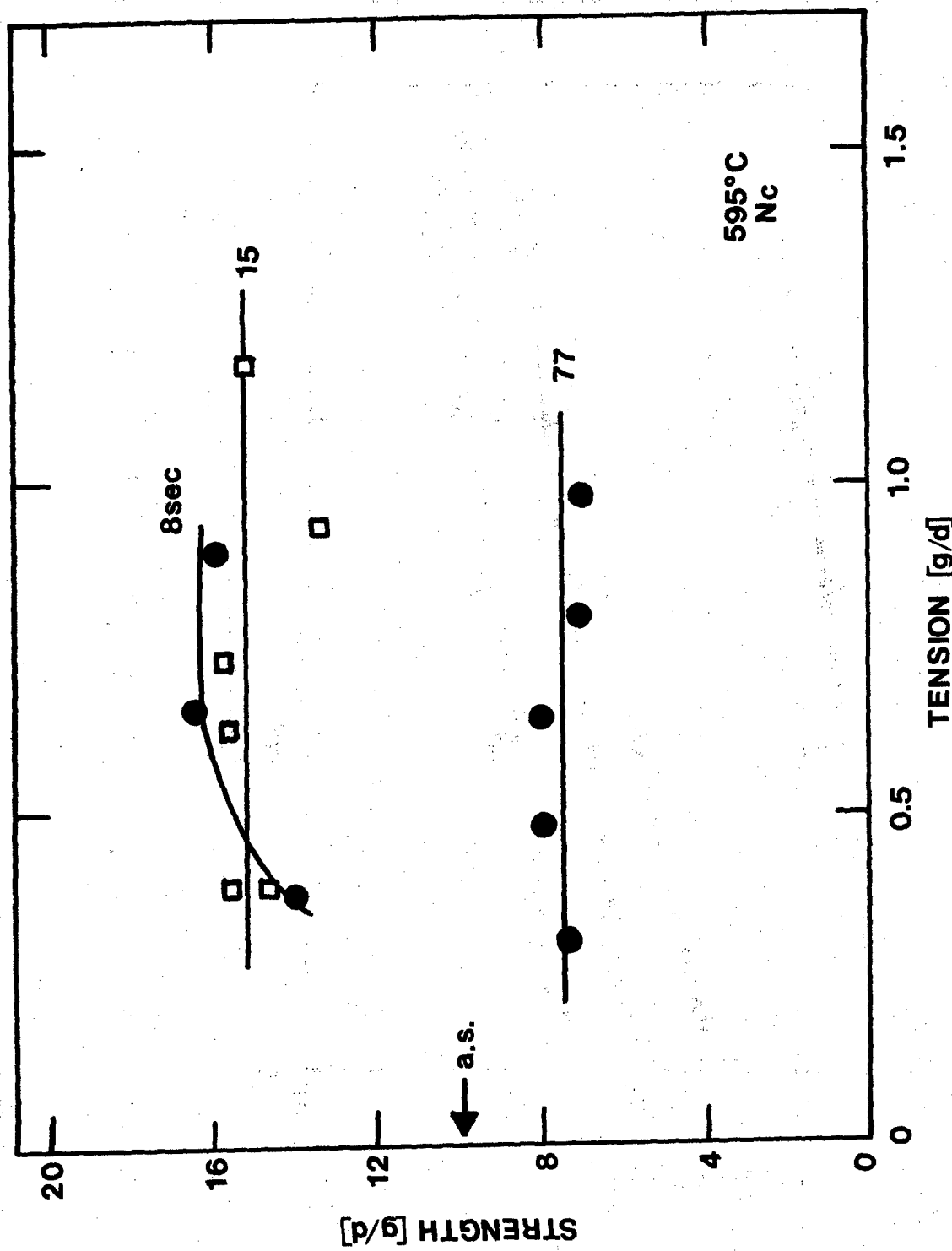


Figure 43. Strength of 595°C heat treated fiber, dependence on residence time and tension. Nitrogen aftercooler used.

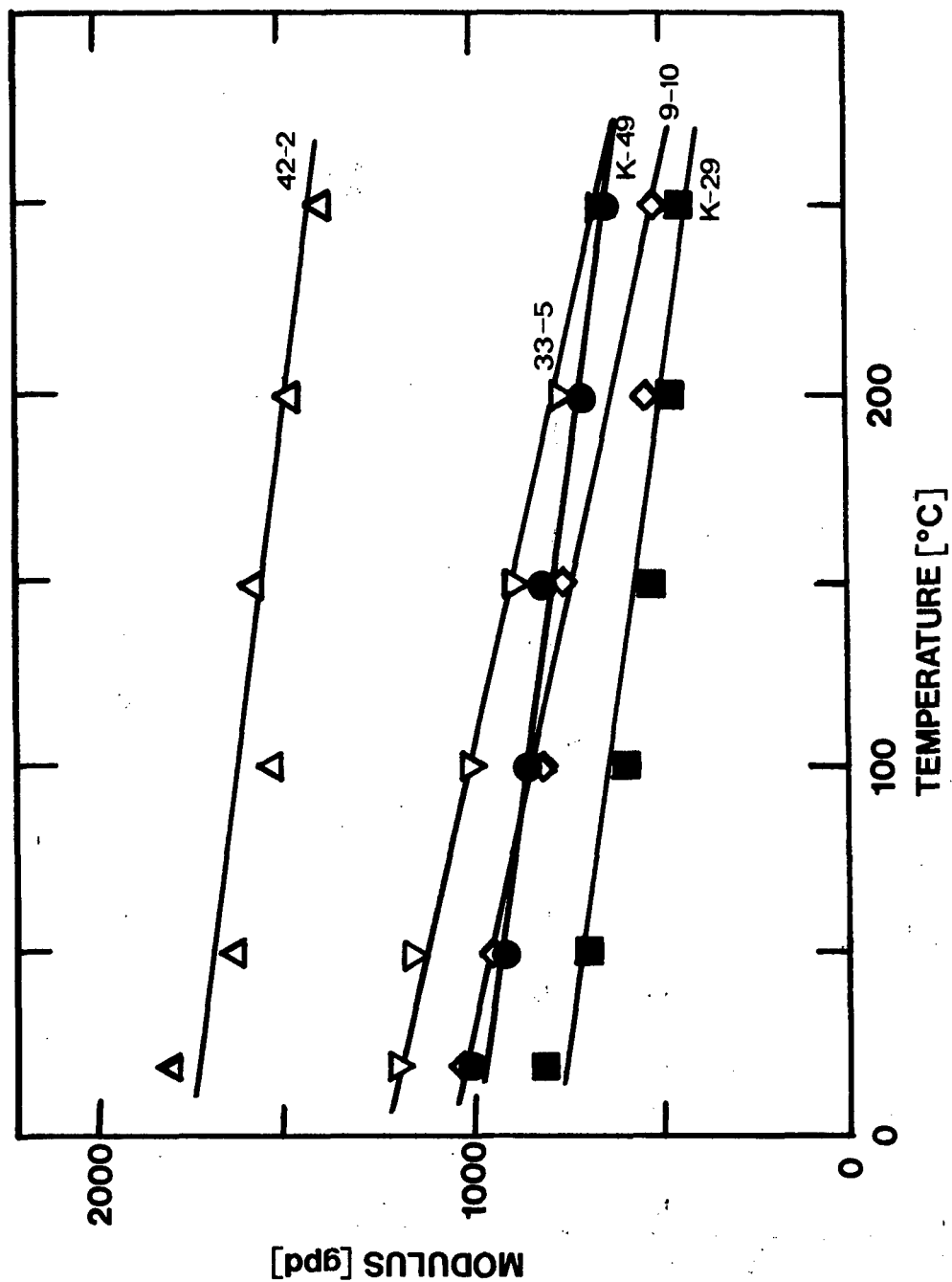


Figure 44. Temperature dependence of Kevlar (K-49, K-29), as spun PBT (9-10, 33-5) and heat treated PBT (42-2) fiber modulus.

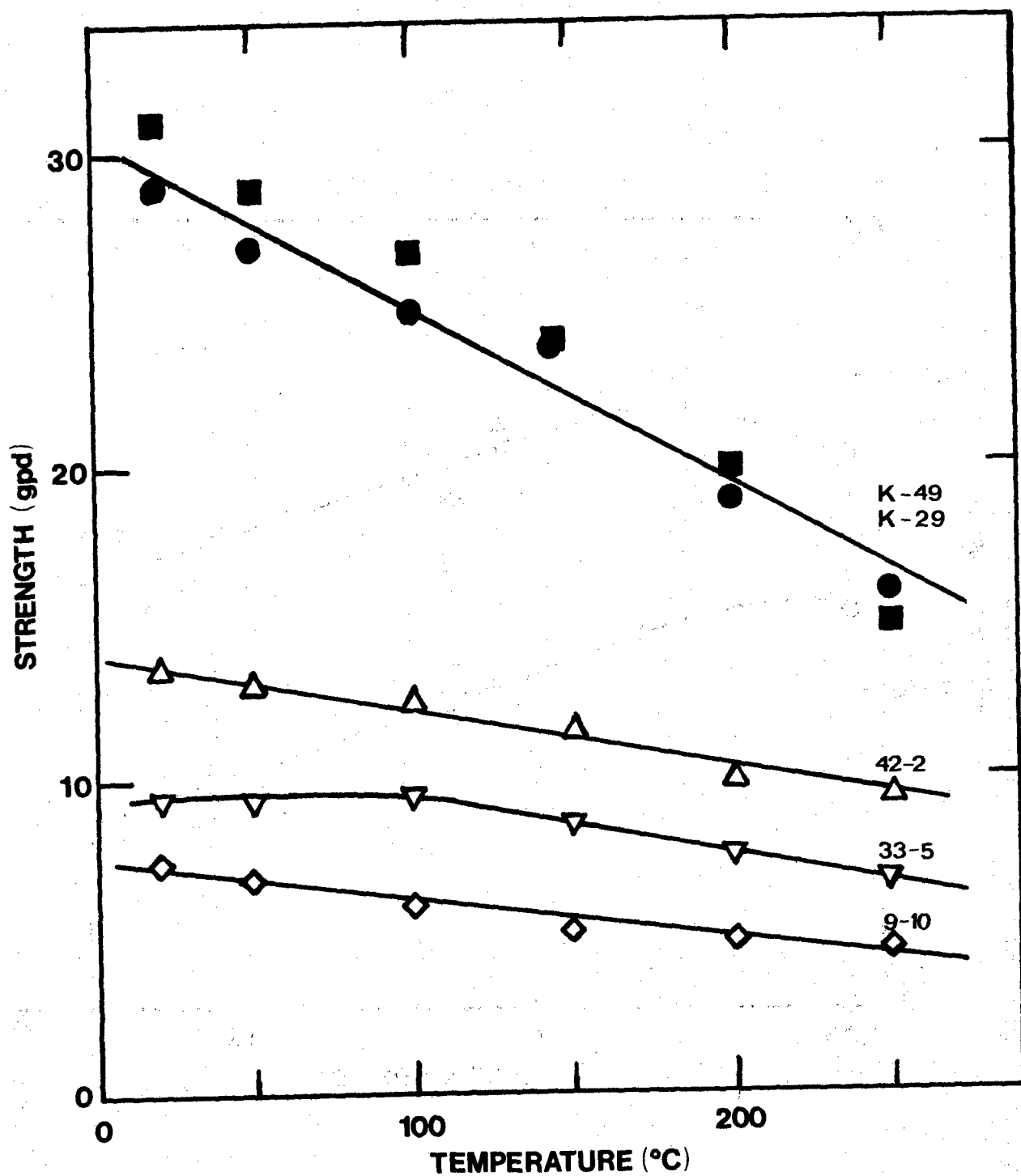


Figure 45. Temperature dependence of Kevlar (K-49, K-29), as spun PBT (9-10, 33-5) and heat treated PBT (42-2) fiber strength.

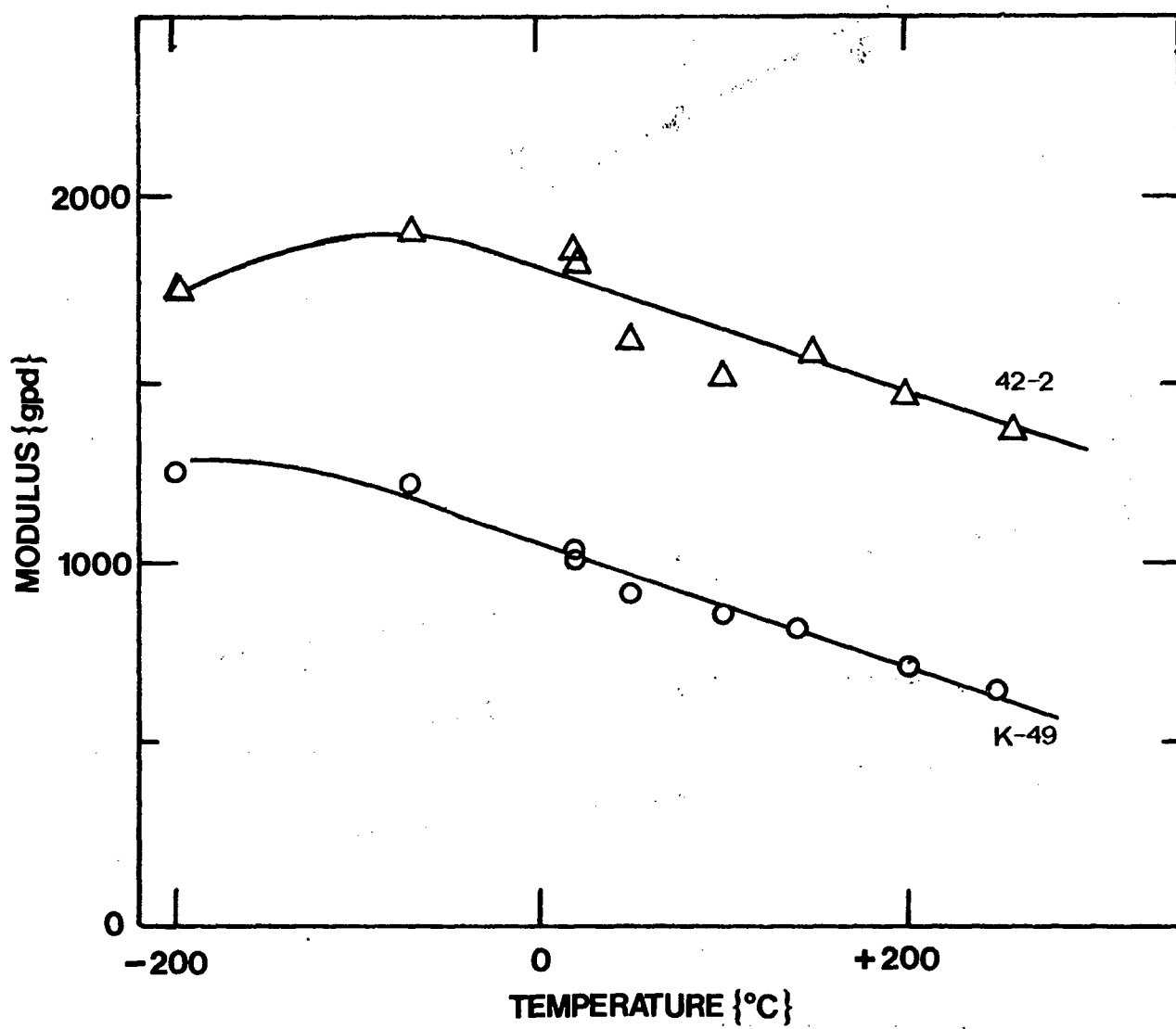


Figure 46. Fiber modulus dependence on temperature for Kevlar 49 and heat treated PBT fibers.

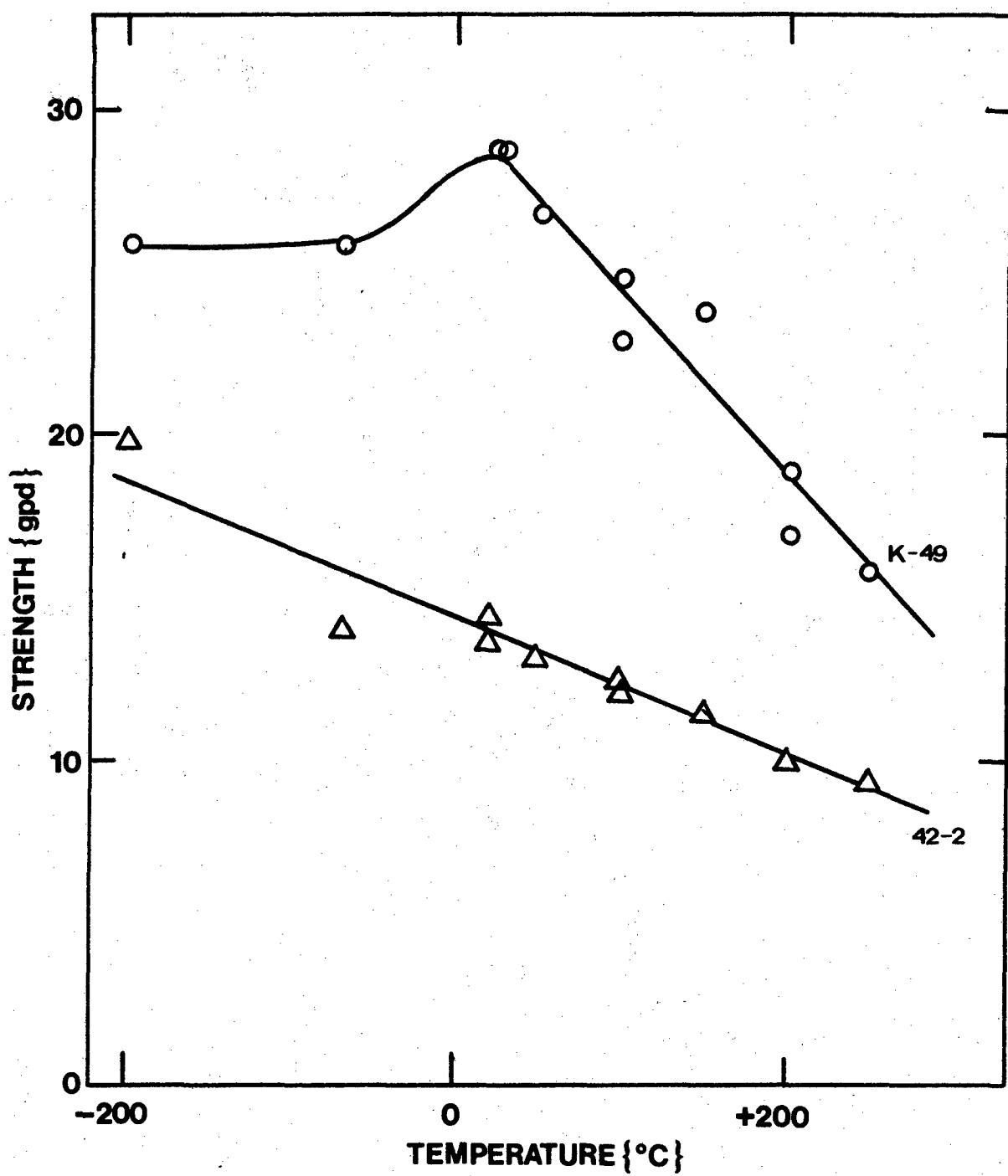


Figure 47. Fiber strength dependence on temperature for Kevlar 49 and heat treated PBT fibers.

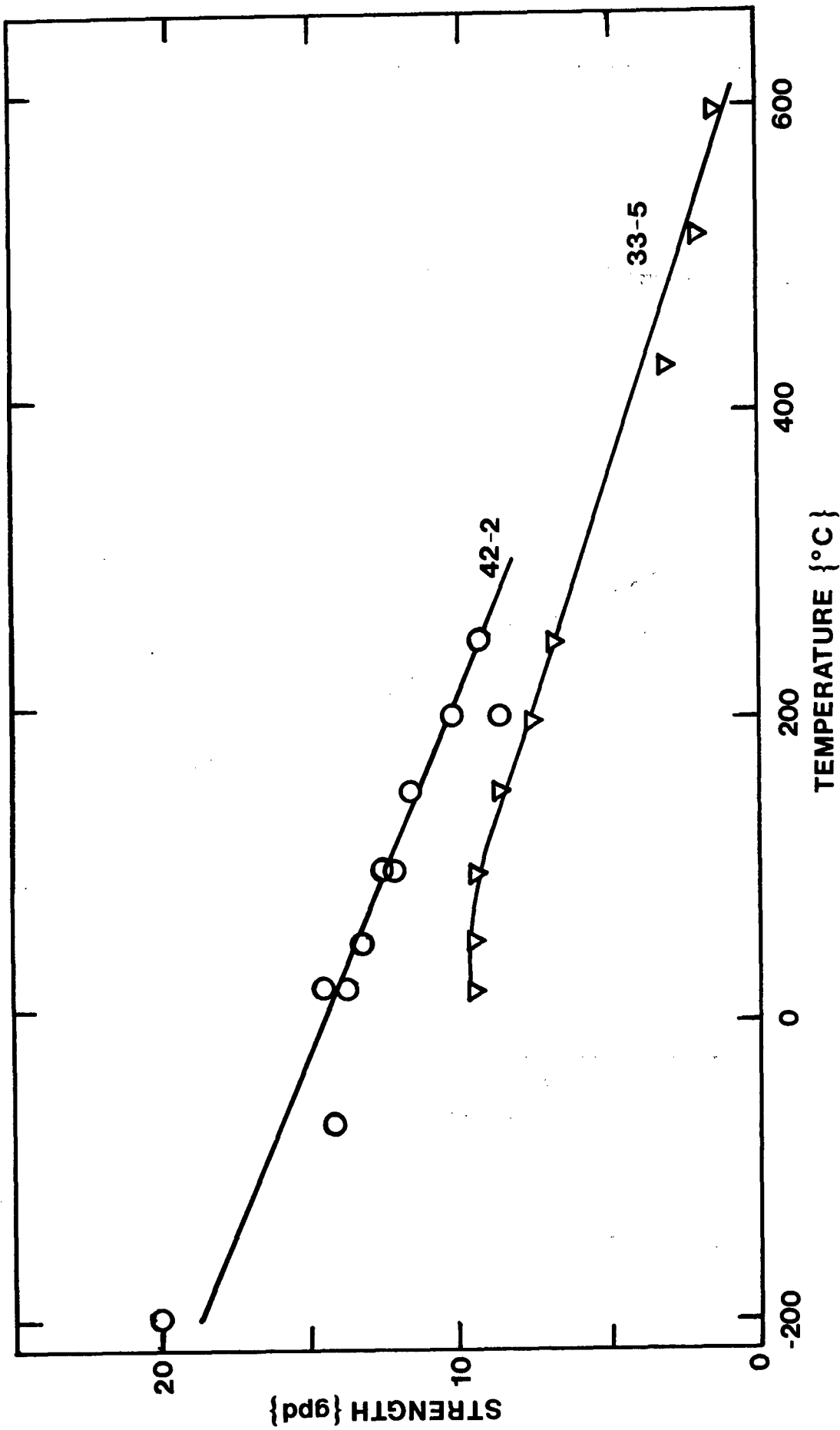


Figure 48. PBT fiber strength dependence on temperature.

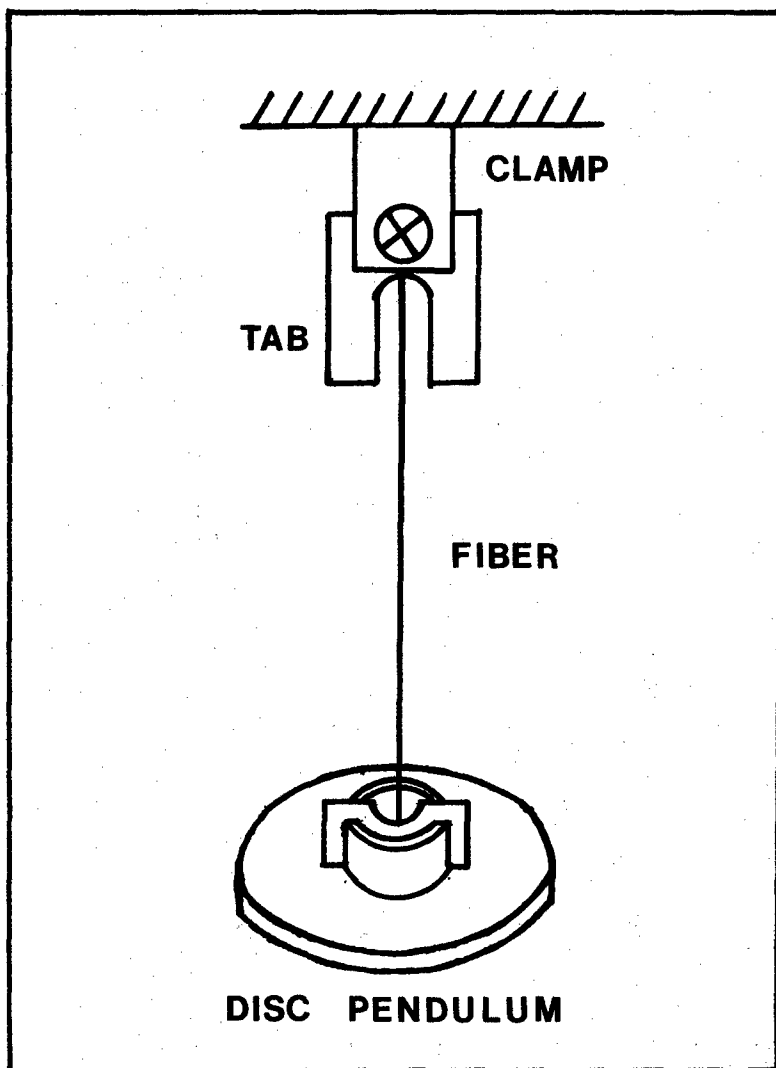


Figure 49. Schematic of torsion pendulum apparatus employed for the determination of fiber torsional moduli.

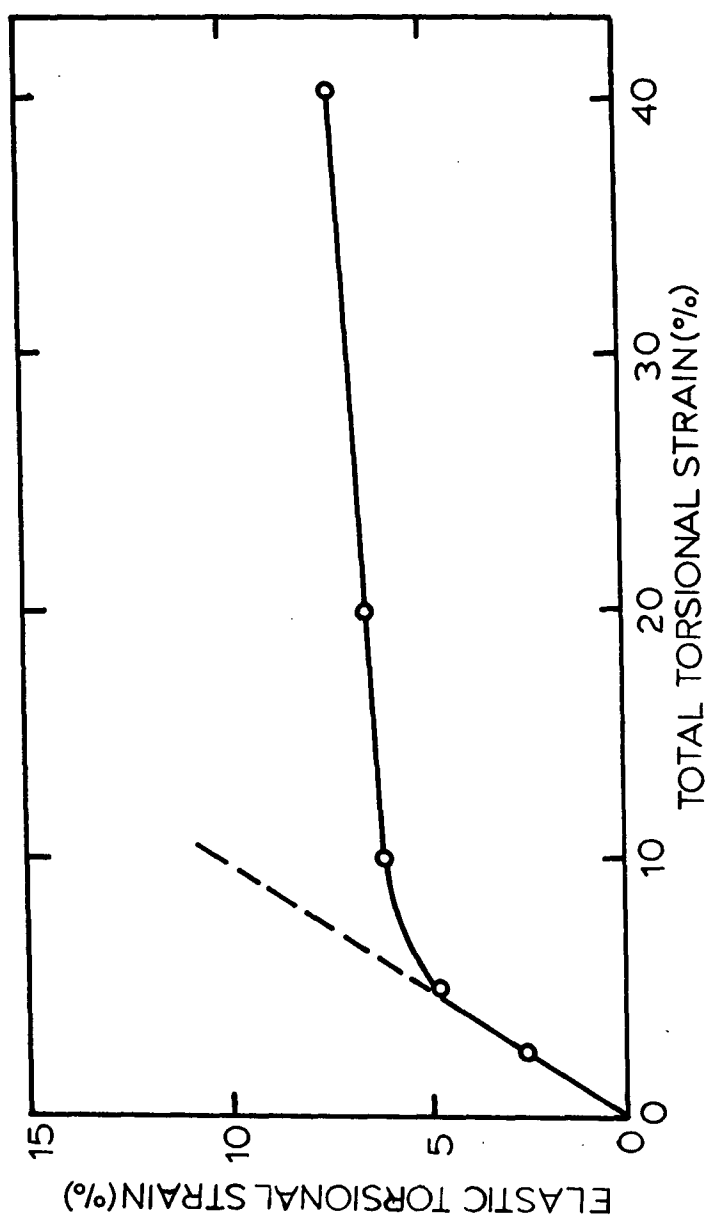


Figure 50. Torsional behavior of PBT fibers.

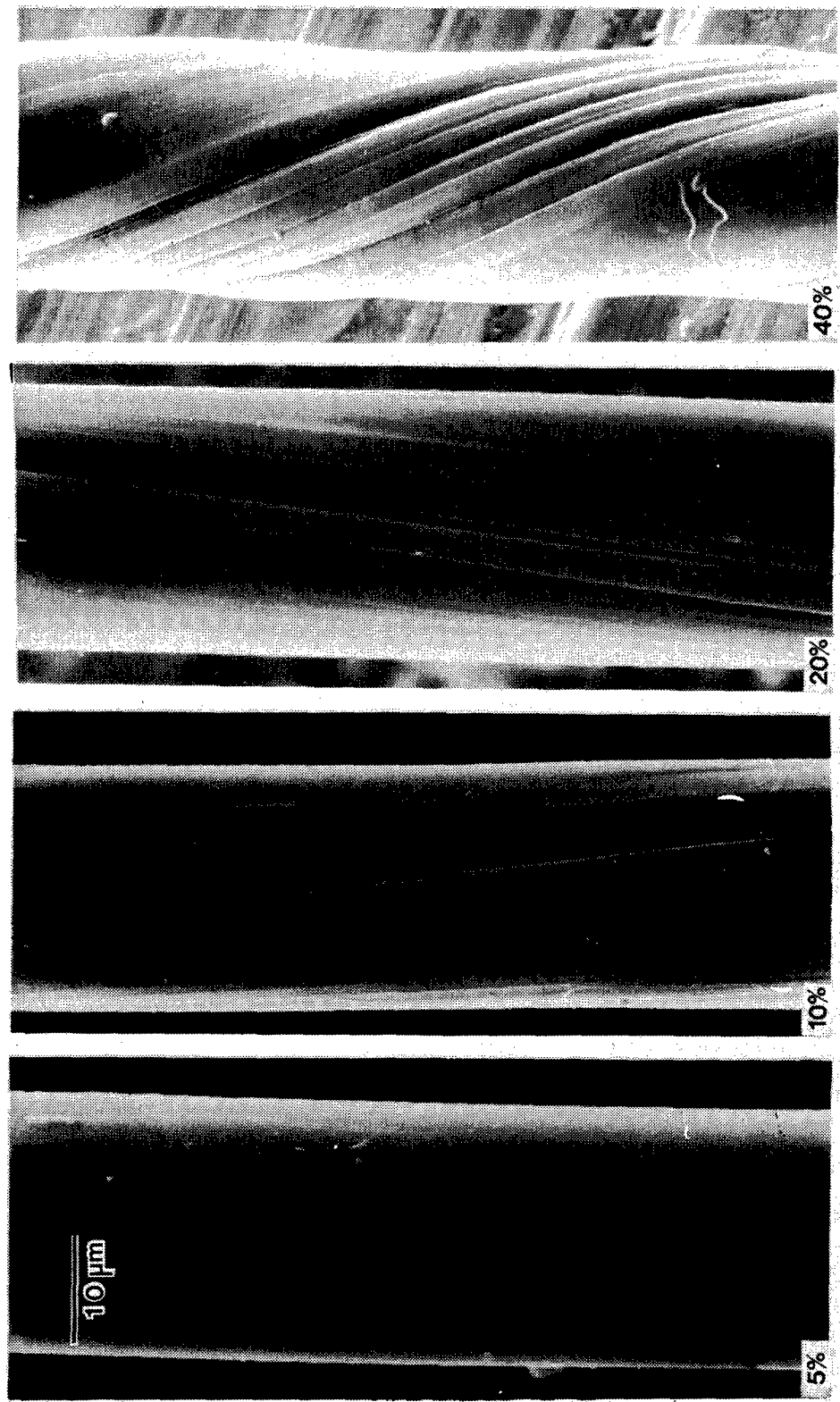


Figure 51. Surface appearance of twisted PBT fibers (strains refer to the fiber surface).

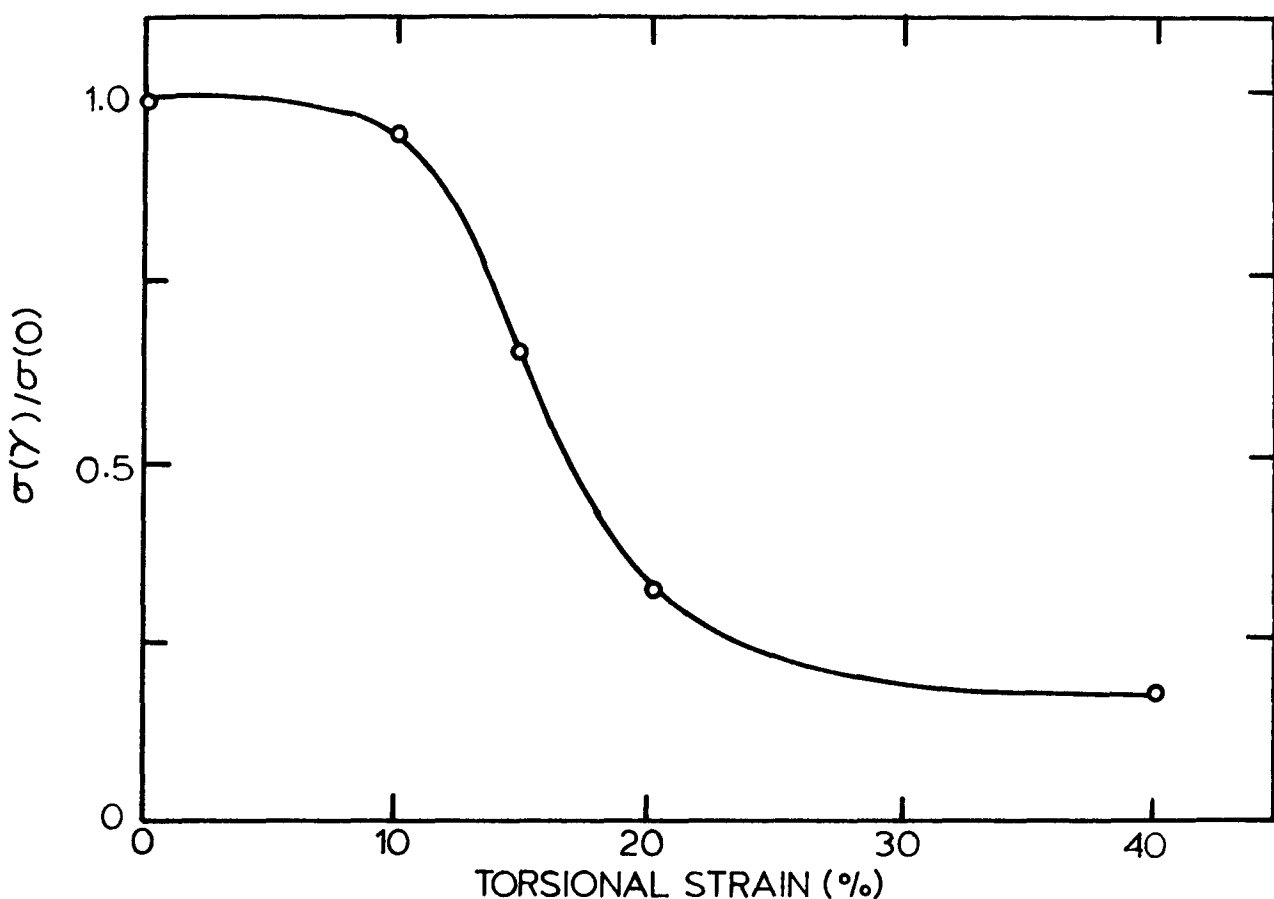


Figure 52. Variation of PBT fiber strength with initial pretwisting.

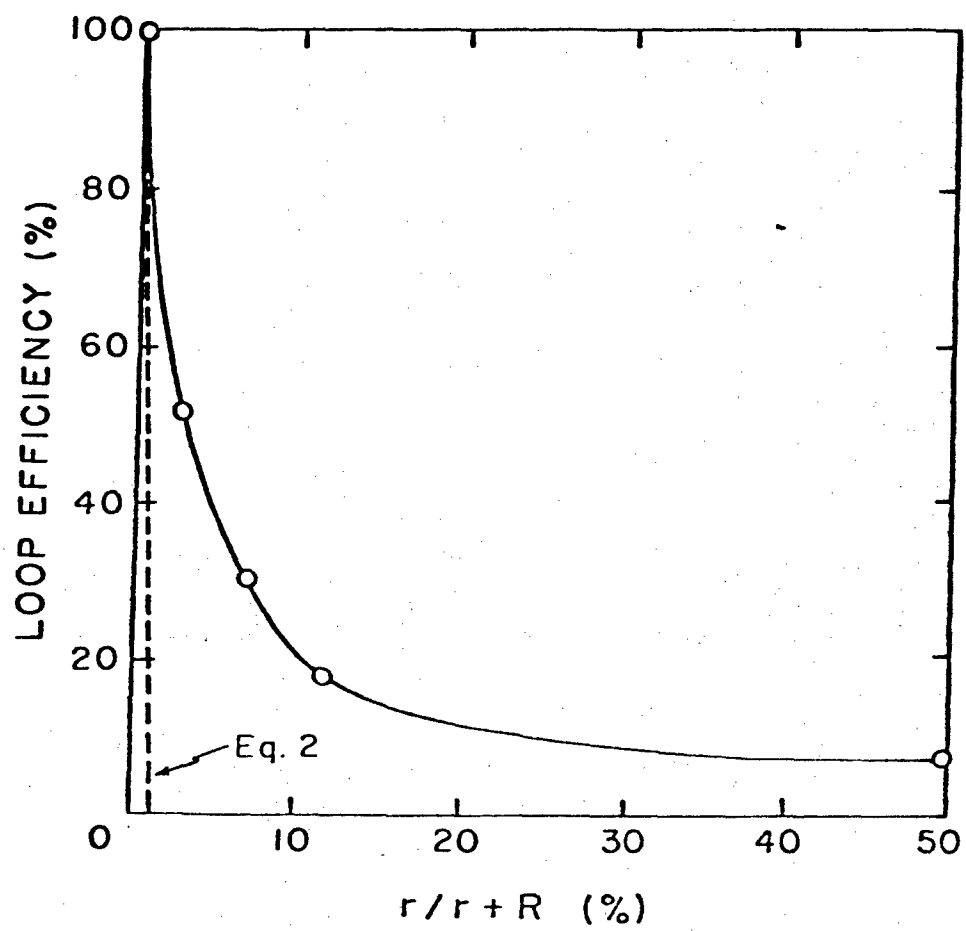
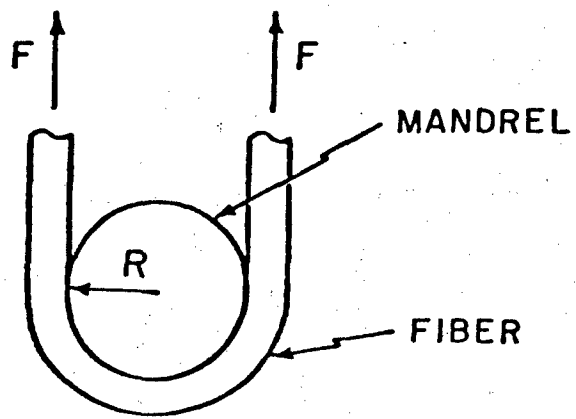


Figure 53. a) Geometry of mandrel loop test. b) Loop efficiency of PBT fiber.

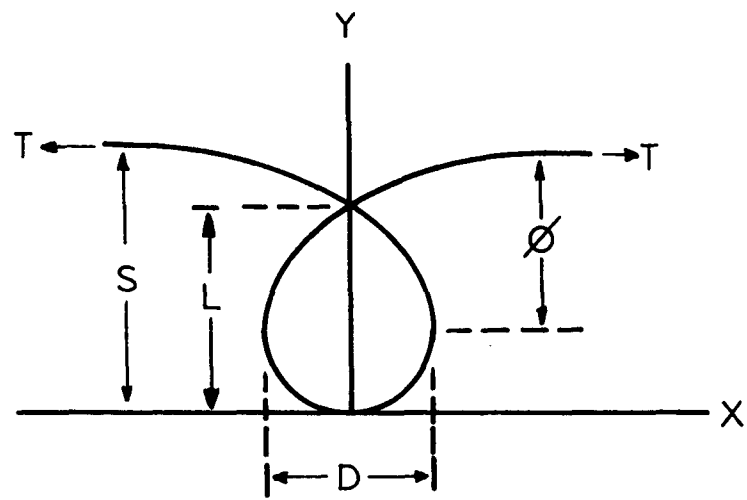


Figure 54. Geometry of elastica loop test.

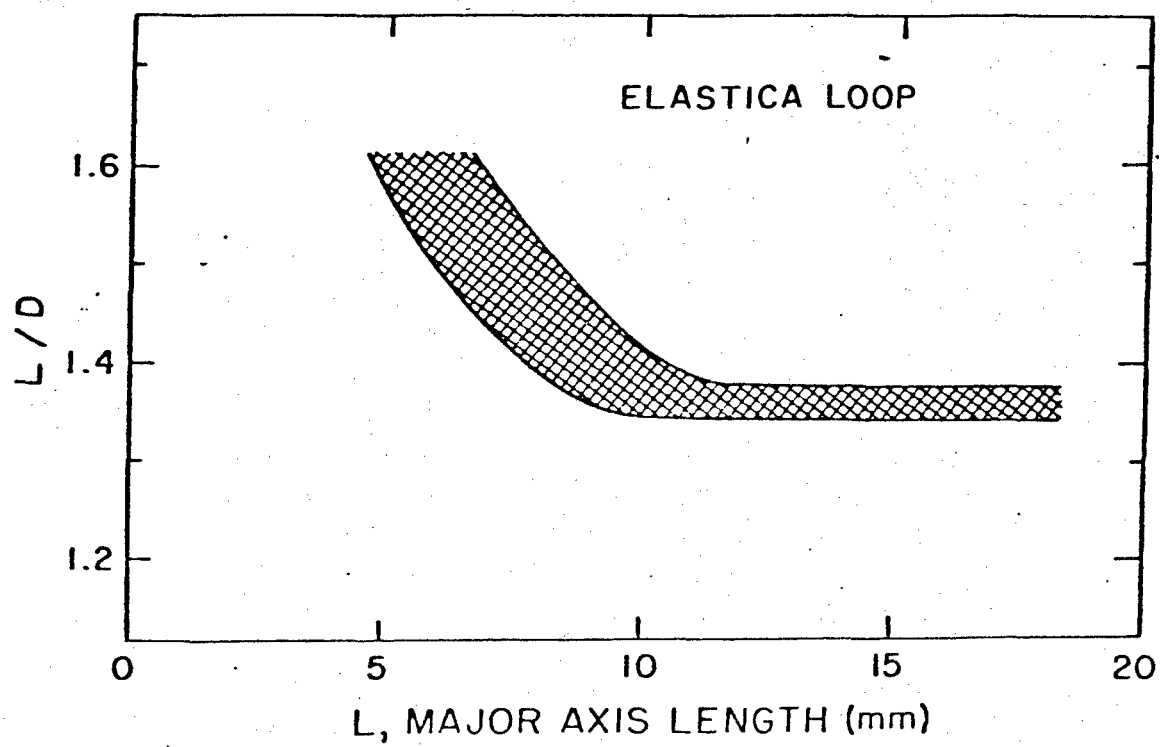


Figure 55. Elastica loop behavior of PBT fibers.



Figure 56. Kinks produced in bending of PBT fibers.

## REFERENCES

1. K. Holland-Moritz, K. Van Werden, *Makromol. Chem.*, 182, 651 (1981).
2. D.K. Roylance and K.L. DeVries, *J. Polym. Sci., Polym. Lett. Ed.*, 9, 443 (1971).
3. R.A. Evans and H.E. Hallam, *Polymer*, 17, 838 (1976).
4. V.K. Mitra, W.M. Risen, Jr., and R.H. Baughman, *J. Chem. Phys.*, 66, 2731 (1977).
5. S.N. Zhurkov, V.I. Vettegren, V.E. Korsukov and J.I. Novak, *Fracture*, 2, 545 (1969).
6. R.P. Wool, *Polym. Eng. Sci.*, 20, 805 (1980).
7. H.W. Siesler, *Makromol. Chem.*, 180, 2261 (1979).
8. J. Minter and E.L. Thomas (to be published).
9. N.J. Harrick, *J. Opt. Soc. Amer.*, 54, 1281 (1964).
10. J.L. Koenig and M. Itoga, *Applied Spectroscopy*, 25, 355 (1971).
11. L.E. Wolfram, J.G. Grasselli, and J.L. Koenig, *Applied Spectroscopy*, 24, 263 (1970).
12. G.M. Venkatesh, D.Y. Shen and S.L. Hsu, *J. Polym. Sci., Polym. Phys. Ed.* (in press).
13. D.Y. Shen, G.M. Venkatesh, D.J. Burchell and S.L. Hsu, *J. Polym. Sci., Polym. Phys. Ed.* (in press).
14. G. Varsányi, Vibrational Spectra of Benzene Derivatives, Academic Press, New York, 1969.
15. F.R. Dollish, W.G. Fateley and F.F. Bentley, Characteristic Raman Frequencies of Organic Compounds, John Wiley & Sons, New York, 1974.

16. G. Sbrana, E. Castellucci and M. Ginanneschi, *Spectrochim. Acta*, 23A, 751 (1967).
17. G. Davidovics, C. Garrigou-Lagrange, J. Chouteau and J. Metzger, *Spectrochim. Acta*, 23A, 1477 (1967).
18. G. Davidovics, P. Roepstorff, J. Chouteau and C. Garrigou-Lagrange, *Spectrochim. Acta*, 23A, 2669 (1967).
19. M.W. Wellman, W.W. Adams, D.S. Dudas, D.R. Wiff and A.V. Fratini in Abstracts, Proceedings of the American Crystallographic Association Meeting, Boston, 1979.
20. W.J. Welsh, P. Bhaumik and J.E. Mark, First Annual Report for Air Force Office of Scientific Research, No. 78-3683, 1979.
21. S.R. Allen, A.G. Filippov, R.J. Farris and E.L. Thomas, *J. Appl. Polym. Sci.*, 26, 291 (1981).
22. C.P. Wong, H. Ohnuma and G.C. Berry, *J. Polym. Sci. - Polym. Symposia* 65, 173 (1978).
23. G. Berry (private communication).
24. A.C. Albrecht and M.C. Hutley, *J. Chem. Phys.*, 55, 4438 (1971).
25. T.E. Helminiak, 177th ACS Meeting, Hawaii, 675 (1979).
26. E.D. Schmid and B. Brosa, *J. Chem. Phys.*, 56, 6267 (1972).
27. G. Sbrana, E. Castellucci and M. Ginanneschi, *Spectrochim. Acta*, 23A, 751 (1967).
28. G. Davidovics, C. Garrigou-Lagrange, J. Chouteau and J. Metzger, *Spectrochim. Acta*, 23A, 1477 (1967).

29. G. Davidovics, P. Roepstorff, J. Chouteau and C. Garrigou-Lagrange, Spectrochim. Acta, 23A, 2669 (1967).
30. M.M. Cordes and J.L. Walter, Spectrochim. Acta, 24A, 237, 1421 (1968).
31. H. Suzuki, Bull. Chem. Soc., Japan, 32, 1340 (1959).
32. D.J. Burchell and S.L. Hsu, Polymer, 22, 907 (1981).
33. G. Zerbi and S. Sandroni, Spectrochim. Acta, 24A, 483 (1968).
34. G. Zerbi and S. Sandroni, Spectrochim. Acta, 24A, 511 (1968).
35. W.W. Adams, L.E. Azaroff, A.K. Kulshreshtha, Z. für Krist. 150, 321 (1979).
36. W. Adams, A. Grimison and G. Rodriguez, Tetrahedron 23, 2513 (1967).
37. F.R. Dollish, W.G. Fateley and F.F. Bentley, "Characteristics of Raman Frequencies of Organic Compounds", Wiley-Interscience, New York (1974), p. 168.
38. D.T. Grubb and G.W. Groves, "Rate of Damage of Polymer Crystals in the Electron Microscope: Dependence on Temperature and Beam Voltage." Phil. Mag., 24, 815-828 (1971).
39. E.L. Thomas and D.G. Ast, "Image intensification and the electron microscopy of radiation sensitive polymers." Polymer, 15, 37-41 (1974).
40. M.G. Dobb, D.J. Johnson, and B.P. Saville, "Direct Observation of Structure in High-Modulus Aromatic Fibers," J. Polym. Sci.: Polym. Symp., 58, 237-251 (1977).
41. K. Suehiro, Y. Chatani, and H. Tadokoro, "Structural Studies of Polyesters. VI. Disordered Crystal Structure (Form II) of Poly( $\beta$ -Propiolactone)." Polymer J. (Japan), 7(3), 352-358 (1975).

42. H. Tadokoro, Structure of Crystalline Polymers, USA: John Wiley and Sons, Inc., (1979).
43. W.W. Adams, L.V. Azaroff, and A.K. Kulshreshtha, "X-ray diffraction by a nematic polybenzothiazole fiber." Z. für Krist., 150, 321-326 (1976).
44. E.L. Thomas, R.J. Farris, S.L. Hsu, S. Allen, A. Filippov, J. Minter, E. Roche, K. Shimamura, T. Takahashi and G. Venkatesh, "Mechanical Properties vs. Morphology of Ordered Polymers." AFWAL-TR-80-4045, Vol. 2 (1981).
45. Gibson and Howie
46. J.A. Odell, A. Keller, E.D.T. Atkins, and M.J. Miles, "Preparation, properties and structure of poly(p-phenylene benzobisthiazole) films." J. Mat. Sci., 16, 3309-3318 (1981).
47. M.W. Wellman, W.W. Adams, R.A. Wolff, D.S. Dudis, D.R. Wiff, and A.V. Fratini, "Model Compounds for Rigid-Rod Aromatic Heterocyclic Polymers. 1. X-Ray Structures of 2-6 Diphenylbenzo[1,2d:4,5d']bisthiazole and 2-6 Diphenylbenzo[1,2-d:5,4-d']bisthiazole." Macromolecules, 14, 935-939 (1981).
48. M. Yokouchi, H. Tadokoro, Y. Chatani, "Conformational and Packing Stability of Crystalline Polymers. V. A Method for Calculating Conformational Parameters of Polymer Chains with Gide, Helical and Translational Symmetries." Macromolecules, 7(6), 769-776 (1974).
49. E. Roche, private communication.
50. M.J. Buerger, "Some Physical Factors Affecting Intensities." Crystal Structure Analysis, NY: Wiley (1960), pp. 195-241.

51. W.J. Welsh, D. Bhaumik, and J.E. Mark, "Phenylene Group Rotations and Nonplanar Conformations in Some cis- and trans-Poly(benzobisoxazoles) and -Poly(benzobisthiazoles)." *Macromolecules*, 14, 947-950 (1981).
52. J.P. Cotton, D. Decker, H. Benoit, B. Tarnoun, J. Higgins, G. Jannick, R. Ober, C. Picot, and J. des Cloiseaux, "Conformation of Polymer Chain in the Bulk." *Macromolecules*, 7, 863-872 (1974).
53. G.E. Bacon, Neutron Diffraction, 2nd ed., Clarendon Press, Oxford, 1962.
54. G.E. Bacon, "Coherent Neutron Scattering Amplitudes." *Acta Cryst.*, A28, 357-358 (1972).
55. G.E. Bacon, Neutron Scattering in Chemistry, London: Butterworths (1977).
56. E.J. Roche, T. Takahashi, and E.L. Thomas, "Structure of High Modulus Fibers of Poly(p-phenylene benzobisthiazole)." Fiber Diffraction Methods, ACS Symposium Series 141, Ed. A.D. French and K.H. Gardner, 303-313 (1980).
57. A. Guinier and G. Founet, Small Angle Scattering of X-Rays, USA: John Wiley and Sons., Inc., (1965).
58. A. Guinier "Diffraction of X-rays at Small Angles - Application to the Study of Ultramicroscopic Phenomena" *Ann. Physique*, 12, 161-237 (1939).
59. A.Z. Akcasu, G.C. Summerfield, S.N. Tahshan, C.C. Hur, C.Y. Kim, and H. Yu, "Measurement of Single Chain Neutron Scattering in Concentrated Polymer Solutions." *J. Polym. Sci.: Polym. Phys.* Ed., 863-869 (1980).
60. G.D. Wignall, R.W. Hendricks, W.C. Koehler, J.S. Cin, M.P. Wai, E.L. Thomas, and R.S. Stein, "Measurements of Single Chain Form Factors by Small Angle Neutron Scattering from Polystyrene Blends Containing High Concentrations of Labeled Molecules." *Polymer*, in press (1981).

61. L.E. Alexander, X-Ray Diffraction Methods in Polymer Science, NY: Krieger Publishing Co., (1979).
62. W.O. Statton, VI. Small-Angle X-Ray Studies of Polymers." Newer Methods of Polymer Characterization, ed. B. Ke, USA: Interscience, (1964).
63. P.H. Hermans, D. Heikens, and A. Weidinger, "A Quantitative Investigation on the X-Ray Small Angle Scattering of Cellulose Fibers. Part II. The Scattering Power of Various Cellulose Fibers." J. Polym. Sci., 35, 145-165 (1959).
64. M.G. Dobb, D.J. Johnson, A. Majeed, B.P. Saville, "Microvoids in aramid-type fibrous polymers." Polymer, 20, 1284-1288 (1979).
65. P. Debye and A.M. Bueche, "Scattering by an inhomogeneous solid." J. Appl. Phys., 20, 518-525 (1949).
66. P.F. Van Hutton, "Small-Angle X-Ray Scattering Studies of Macromolecular and Colloidal Systems." Ph.D. dissertation, University of Groningen, 1981.
67. R.S. Stein and T. Hotta, "Light Scattering from Oriented Polymer Films." J. Appl. Phys., 35(7), 2237-2242 (1964).
68. G.C. Summerfield and F.R. Mildner, "Small Angle Scattering with Azimuthal Symmetry." J. Appl. Cryst., in press.
69. E.O. Brigham, "The Discrete Fourier Transform." The Fast Fourier Transform, Englewood Cliffs, NJ: Prentice Hall, (1974).
70. R.S. Stein, personal communication.
71. M.H. Jellinek, E. Solomon, and I. Fankuchen, "Measurement and Analysis of Small-Angle X-Ray Scattering." Ind. Eng. Chem., 18(3), 172-175 (1946).

72. R. Hosemann and S.N. Bagchi, Direct Analysis of Diffraction by Matter, New York: North-Holland Pub. Co./Interscience, (1962).
73. L.E. Alexander, op. cit., pp. 291-293.
74. B. Crist, "Microfibril Dimensions from Small-Angle X-ray Scattering." J. Appl. Cryst., 12, 27 (1979).
75. J.T. Koberstein, B. Morra, and R.S. Stein, "The Determination of Diffuse-Boundary Thicknesses of Polymers by Small-Angle X-Ray Scattering." J. Appl. Cryst., 13, 34-45 (1980).
76. H. Yamakawa, Modern Theory of Polymer Solutions, New York: Harper and Row (1971).
77. E.L. Thomas, R.J. Farris and S.L. Hsu, AFWAL-TR-80-4045, Vols. I, II (1980).
78. D. Sinclair, J. Appl. Phys., 21, 380 (1950).